Theoretical study of charge density waves in transition metal materials

Junichi Okamoto

Submitted in partial fulfillment of the
Requirements for the degree
of Doctor of Philosophy
in the Graduate School of Arts and Sciences

COLUMBIA UNIVERSITY

2014

Abstract

Theoretical study of charge density waves in transition metal materials

Junichi Okamoto

In this thesis we theoretically study new aspects of charge density waves in transition metal materials recently revealed by scanning tunneling microscopy measurements. The two important problems that we have investigated are the effects of orbital degeneracy on the formation of the charge-density waves in cobalt nanowires, and the effects of dilute but strongly pinning impurities on the charge-density wave in niobium diselenide.

We first present an overview on charge-density waves, and then introduce a general theoretical model describing charge-density waves. We also explain several known results about disorder effects on charge-density waves. We briefly touch on the principle of scanning tunneling microscopy and its advantages compared to other experimental tools.

Second, we discuss the physics of one-dimensional cobalt nanowires along with experimental results. We propose a theoretical model that is relevant to cobalt nanowires, and then analyze the model by two theoretical tools: mean-field theory and bosonization. Our results show that the multi-orbitals allow a spin-triplet interaction among electrons leading to different phase diagrams from the ones considered previously for similar models. Numerical results obtained by first-principles calculations are also briefly explained.

Third, we consider the effects of dilute strong impurities on the charge-density wave in niobium diselenide, a transition metal dichalcogenide. We first explain the material and properties of its charge-density wave phase. Then, detailed analysis of a scanning tunneling microscopy measurement is presented. Next, we analytically and numerically study a phenomenological model relevant to the experiment. We show that the dilute strong impurities have little effects at large length scales compared to the average inter-impurity distance, leading to a topologically ordered phase with a (quasi-)long-range autocorrelation; this result is quite different from conventional pictures predicting short-range order with the proliferation of topological defects.

Contents

List of Tables

List of Figures

Acknowledgments

First, I would like to express my sincere gratitude to my advisor, Professor Andrew J. Millis. It was great fortunate that I could work with him for six years at Columbia University. Through countless discussions that we had, I learned many things from basic principles of physics to some algebraic techniques. Also, I appreciate that he always encouraged me to go to summer schools, where I learned a lot about physics and made many friends.

I thank Nader Zaki, Professor Osgood, Carlos J. Arguello, Ethan P. Rothenthal, Professor Pasupathy, and Rafael Fernandes for our fruitful collaboration. I have been always motivated by their experiments and discussions with them. I thank Hung The Dang, Se Young Park, Edgardo Carrillo, Florian Elste, Rainer Härtle, and Ara Go for many helpful conversations and discussions. Also, I am very grateful to Professor Uemura, Tsuguo Aramaki, and Kyo Iigaya for their mentorships.

I also would like to express my appreciation to the professors in the defense committee: Boris Altshuler, Richard Osgood, Abhay Pasupathy, and David Reichman, for their careful examination on my dissertation.

Finally, I would like to thank my parents, who have been always encouraging me, and my wife, Claire, for her support and cares.

Chapter 1
Introduction

1.1 Overview

In this thesis, we theoretically study charge-density waves in transition metal materials. Motivated by the recent discovery of a low-temperature dimerized state in Co nanowires [Zaki et al. (2013)], in Chap. 2, we consider one-dimensional charge-density waves in transition metal nanowires. In Chap. 3, we investigate the disorder effects on the charge-density wave in $NbSe_2$ based on recent scanning tunneling microscopy measurements [Okamoto et al. (2014)].

This chapter is an introduction to the thesis. We start by giving a general overview of charge-density waves in the first section. In the second section, a phenomenological model describing a charge-density wave is introduced and explained. We review the disorder effects on charge-density waves in the third section. A brief description of a scanning tunneling microscopy technique for the study of charge-density wave materials is presented in the last section.

1.2 Charge-density waves: background

Interacting condensed matter systems often exhibit spontaneously broken symmetries at low-temperatures, and a classification of phases of matters by the broken

symmetry (an idea proposed by Lev Landau) has been a central dogma of theoretical physics since the last century. Spontaneously broken symmetry means that at high-temperatures, the state of the system has the same symmetry of the Hamiltonian, while at low temperatures, the state of the system falls into a subgroup of the symmetry of the Hamiltonian. Such a transition is characterized by an order parameter, which is zero at the high-temperature disordered phase, but is non-zero at the low-temperature ordered phase. A charge-density wave (CDW) is a typical example of such a broken symmetry phenomenon, and its order parameter is a density modulation of electrons whose periodicity is different from the one at high temperatures; the translational symmetry at high temperatures is broken at low temperatures. In equilibrium situations, this charge modulation accompanies lattice distortion in general, and these two are treated as a single order parameter.

Along with the classification of broken symmetries, an important question is the underlying mechanism of the spontaneous symmetry breaking. In the case of CDWs, Rudolf Peierls first discussed that the nesting of a Fermi surface of electrons can lead to a charge-density modulation considering electrons coupled to phonons (ions) [Peierls (1930)]. Later, this idea was more carefully formulated by himself [Peierls (1996)], and Fröhlich (1954). Mathematically, this formulation is equivalent to the Bardeen-Cooper-Schrieffer (BCS) theory of superconductivity [Bardeen et al. (1957); Lee et al. (1974)], and can be understood as the Fermi surface instability in a particle-hole channel; for instance, the particle-hole susceptibility is divergent at $|\vec{Q}| = 2k_F$ (k_F: the Fermi wave vector) for one-dimensional electrons. The energy gain comes from the energy gap opening around the Fermi energy, so the wavelength of the charge modulation is not related to the original lattice periodicity and given by $\lambda = \pi/k_F$. The dominant driving force for the CDW in this case is the electronic part, while phonons are weak scatters of electrons on the Fermi surface. Thus, the amplitude of the CDW and lattice distortion is small compared to the original lattice constant

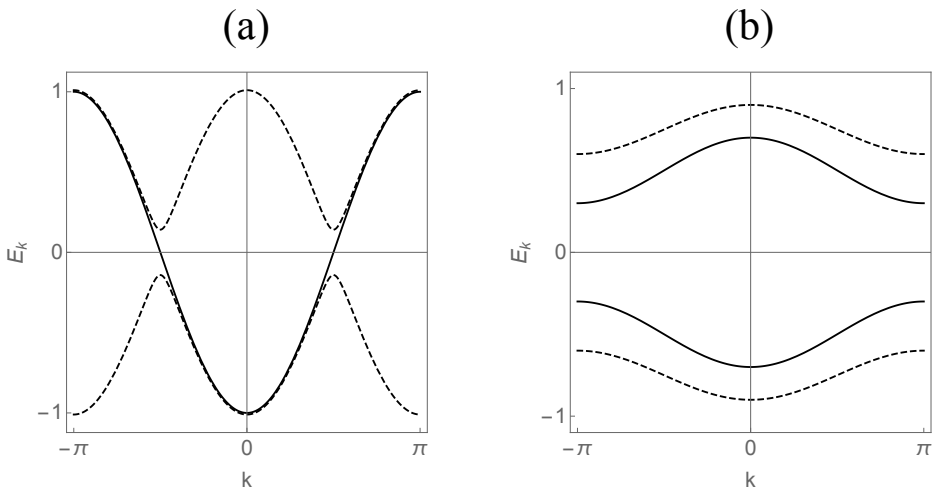

Figure 1.1: Solid (dashed) lines indicate the original (modified) energy bands. Energies are measured from the chemical potential. (a) When the electron-phonon coupling is weak, the energy gain comes from the Fermi surface. (b) When the coupling is strong, the energy gain comes from the occupied band far from the Fermi energy.

a. Instead the coherence length ξ, which is the distance of the electron-hole pair creating the CDW, i.e., the measure of the rigidity of the CDW, is large as the BCS theory ($\xi \gg a$). Since the BCS theory gives a mean-field like transition, there are no electron-hole pairs above the transition temperature. Because nesting requires a special geometry such as quasi-one-dimensional alignment of molecules, this theory had not been verified until experiments on organic compounds such as TTF-TCNQ became possible in 1970s [Jérome and Schulz (1982)]. Blue bronzes [Schlenker (1983)], and some transition metal chalcogenides [Rouxel and Schlenker (1989)] are also considered to follow this scenario. We will discuss how the Peierls' idea is modified when electrons in one-dimension are interacting (Luttinger liquids) in Chap. 2.

Another scenario inducing CDWs is "phonon softening" [Dove (1993)]. In this picture, ions are vibrating around their equilibrium positions at high temperatures, while the anharmonic couplings between vibrating modes (phonons) turn the frequencies

of the modes into imaginary at low temperatures; the high temperature equilibrium positions are no longer stable. Thus at low temperatures, the ions align with a new periodicity inducing also a charge-density modulation. Microscopically, the anharmonic couplings of phonons are due to the electron-phonon couplings [Varma and Simons (1983)], and the induced charge-modulation is intimately connected to the periodic lattice distortion. Therefore, the new periodicity is typically close to the integer multiple of the original lattice (commensurate) $\lambda = aN/M$ (N, M: integers). We may image this picture more like a local chemical bonding of neighboring ions. Thus, the coherence length is short ($\xi \sim \lambda$), and the CDW amplitude is large. Above the transition temperature, there remain short-range electron-hole pairis; the phase of the CDW is not yet condensed while the amplitude is condensed. Compared to the nesting picture, phonon softening does not necessarily require a non-zero electronic density of states at the Fermi surface, although the energy gain is still from the electronic part (Fig. 1.1). The typical metals having phonon-driven CDWs are transition metal dichalcogenides [Wilson et al. (1975); McMillan (1977)], and we will discuss, in particular, 2H-$NbSe_2$ in Chap. 3.

In a real material, along with the electron-phonon coupling, electron-electron interactions also exist. Naively speaking, electronic interactions tend to suppress charge-density waves, simply because electrons repel each other and charge-density modulation, which has a local charge accumulation, is not preferable. Instead, spin-density waves are often induced for repulsive interactions [Overhauser (1960); Chan and Heine (1973)]. For semimetals and semiconductors, the interactions between electrons and holes may lead to a CDW [Halperin and Rice (1968a,b)]. On the other hand, as we will see in Chap. 2, for one-dimensional electrons with orbital degeneracy, there are various scattering processes that can compete with the spin-density waves, leading to a non-trivial rich phase diagram.

From the above mechanisms, we can draw the following simple picture for a CDW

phase transition [Tosatti (1980)]. As for most of classical phase transitions, a CDW transition occurs as a result of a competition between energy and entropy in free energies $F = E - TS$ (F: free energy, E: energy, T: temperature, S: entropy). The energy of a CDW state is lower than the energy of a normal state;

$$\Delta E = E_{\mathrm{CDW}} - E_{\mathrm{normal}} = \Delta E_{\mathrm{lattice}} + \Delta E_{\mathrm{electron}} < 0, \tag{1.1}$$

where the energy difference is decomposed into two contributions from electrons and phonons. As depicted in Fig. 1.1, a CDW always gains electronic energy by either opining a gap at the Fermi surface or lowering the valence band, $\Delta E_{\mathrm{electron}} < 0$ [Johannes and Mazin (2008)]. On the other hand, due to the lattice distortion, the lattice part has to pay extra elastic energy, thus $\Delta E_{\mathrm{lattice}} > 0$. In order to have a phase transition, the sum of the two contributions must be negative, $\Delta E < 0$. Now we will look at the entropy difference between CDW and normal states. The entropy of electrons becomes smaller for the CDW state, when a gap opens, since a phase space available for the electrons becomes smaller ($\Delta S_{\mathrm{electron}} < 0$). For the lattice part, we also find $\Delta S_{\mathrm{lattice}} < 0$, since the CDW state is more rigid. Thus, the total entropy difference is always negative $\Delta S < 0$. Therefore, the free energy has a critical temperature satisfying

$$\Delta F = 0 = \Delta E - T_c \Delta S, \tag{1.2}$$

whenever $\Delta E < 0$.

1.3 Ginzburg-Landau theory of charge-density waves

1.3.1 Fluctuations and dimensionality

In this section, we introduce a Ginzburg-Landau model describing a CDW phase transition, and explain some basic features of the model. As is similar to Ginzburg-Landau theories for superconductivity, in a real crystal, a Ginzburg-Landau functional can be very complicated including all the terms allowed by the symmetry. Here we consider only one ordering vector without those complexities. Some specific theories for transition metal dichalcogenides are found in McMillan (1975); Walker and Jacobs (1982); Nakanishi and Shiba (1984), and we will discuss this in Chap. 3. At weak electron-phonon coupling limit, we can derive a Ginzburg-Landau functional rigorously [Grüner (2009)]. When the electron-phonon coupling becomes larger, rigorous derivations are difficult. However, the following model still captures the basic features of the transition, so we will take the model as given:

$$F = F_0 + f \int d\vec{x} \left(t|\psi|^2 + \frac{1}{2}|\psi|^4 + \xi^2 \left| \vec{\nabla}\psi \right|^2 \right), \tag{1.3}$$

where F_0 is the free energy of a normal state, f is the free energy density, $\psi \equiv |\psi|e^{i\phi}$ is a complex order parameter describing the amplitude and the phase of the lattice distortion, and ξ is the bare coherence length. Near the mean-field transition temperature T_c^{MF}, we have $t \sim (T - T_c^{\mathrm{MF}})/T_c^{\mathrm{MF}}$. In general, with multiple ordering vectors, there is a cubic term if three ordering vectors sum up to zero as in a triangular lattice; we will see this in Chap. 3. If the sum of three ordering vectors is non-zero, as in a square lattice, a cubic term is prohibited. The modulated charge density is given by

$$\rho(x) = \rho_0 + \rho_1|\psi| \cos(\vec{Q} \cdot \vec{x} + \phi), \tag{1.4}$$

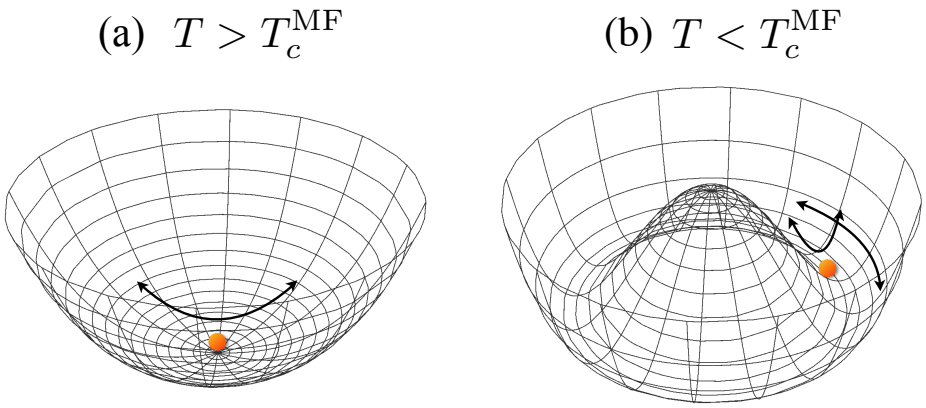

Figure 1.2: (a) The free energy for $T > T_c^{\mathrm{MF}}$. There are two massive amplitude modes around the bottom of the potential. (b) The free energy for $T < T_c^{\mathrm{MF}}$. There are one massive amplitude mode along the radial direction, and one massless phase mode along the minima.

where ρ_0 is the original charge-density, ρ_1 is the modulated density, $\vec{Q}$ is the ordering vector, and ϕ is the phase of ψ. The second term comes from the electrons near $\vec{Q}$. The slow spatial modulation of ϕ (much longer than the wavelength $2\pi/Q$) means that the ordering vector is shifted to $\vec{Q} \to \vec{Q}' = \vec{Q} + \vec{\nabla}\phi$. For a quasi-one dimensional case, the ordering vector is associate with the Fermi wavevector as $Q = 2k_F = \pi\rho_0$. Thus, the local modulation of the phase leads to slow change of the charge density as [Allender et al. (1974)]

$$\delta\rho(x) = \frac{1}{\pi}\nabla\phi. \tag{1.5}$$

When we ignore the fluctuations given in the elastic part, then by minimizing the Ginzburg-Landau functional by ψ, we find a minimum at $\psi = 0$ for $T > T_c^{\mathrm{MF}}$, while we have continuous minima of $|\psi| = \sqrt{|t|}$ for $T < T_c^{\mathrm{MF}}$ (Fig. 1.2). This is a very basic description of a second order phase transition. Now we consider the fluctuations $\delta\psi$

on top of these static configurations ψ_0. For $T > T_c^{\rm MF}$, we have

$$F = f \int d\vec{x} \left(t \left|\delta\psi\right|^2 + \xi^2 \left|\vec{\nabla}\delta\psi\right|^2 \right) + \text{constant}. \tag{1.6}$$

Thus, the fluctuations cost non-zero energy to excite (massive), and gives an exponential decay of the correlation function with a decay length $\xi' \sim \xi/\sqrt{t}$:

$$C(x) = \langle \delta\psi(\vec{x})\delta\psi(0)\rangle \sim T \int \frac{d\vec{p}}{(2\pi)^D} \frac{e^{i\vec{p}\cdot\vec{x}}}{t + \xi^2 p^2} \sim e^{-|\vec{x}|/\xi'}. \tag{1.7}$$

For $T < T_c^{\rm MF}$, the static solution is $\psi_0 = \sqrt{|t|}e^{i\phi_0}$. Writing $\delta\psi = \chi e^{i\phi_0}$, we have

$$F = f \int d\vec{x} \left\{ 2|t|\chi_1^2 + \xi^2 \left[\left(\vec{\nabla}\chi_1\right)^2 + \left(\vec{\nabla}\chi_2\right)^2 \right] \right\} + \cdots, \tag{1.8}$$

where $\chi = \chi_1 + i\chi_2$, and $\cdots$ are constants and the higher order terms. The χ_1 fields are massive amplitudons, while the χ_2 fields are massless phasons (Goldstone modes). The appearance of massless modes is a result of a continuous symmetry breaking; in this case U(1) symmetry (translational symmetry) is broken. We will discuss the cases when the commensurability becomes important, and explain how the continuous symmetry is broken into a discrete one in the next subsection. The fluctuation of the massive modes is not dangerous. However, the behavior of thermal fluctuations of phasons depends on the dimensionality D:

$$\langle \chi_2(0)^2 \rangle = \frac{T}{2f\xi^2} \int \frac{d\vec{p}}{(2\pi)^D} \frac{1}{p^2}. \tag{1.9}$$

When $D \geq 3$, the integral becomes constant, since we always have a ultra-violet (UV) cut-off. However, the integral becomes infra-red (IR) divergent for $D \leq 2$; the fluctuation is so big that the system wanders far away from the original state $\psi_0 = \sqrt{|t|}e^{i\phi_0}$. Thus, there is no long-range order. This is a natural consequence of the Coleman theorem [Coleman (1973)] or Mermin-Wagner-Hohenberg theorem

[Mermin and Wagner (1966); Hohenberg (1967)]. Thus, for the quasi-one-dimensional, and quasi-two-dimensional systems, the phase transition to true long-range order does not occur at the mean-field transition temperature, but occurs at a lower temperature after the inter-chain or inter-layer interactions establish the three dimensional CDW [Imry and Ma (1975)]. In two dimensions, the Kosterlitz-Thouless type transition [Kosterlitz and Thouless (1973)] to a quasi-long range order, where the correlation function is power-law, may occur at a finite temperature.

1.3.2 Effects of backscattering

So far we have not considered the effects of backscattering of electrons. The backscattering are quite important, since it can significantly modify the nature of CDWs; it tries to pin down the phase of the CDW. Complexities arising from these effects are non-trivial, and the main focus of this thesis is to understand the behavior of CDWs under such complicated circumstances. Three dominant contributions to backscattering are lattice potentials, electron-electron interactions, and impurities. We will explain these in the following.

When a lattice potential couples to electrons, it tends to make the period of a lattice distortion or a CDW to a commensurate value. When this tendency is strong as in a phonon-driven CDW, the fluctuation and the ordered phases shows different behaviors from the previous case. Phenomenologically the lattice potential adds a term,

$$-V_0 \cos(M\phi), \tag{1.10}$$

to the Ginzburg-Landau energy. Microscopically, this term arises due to the backscattering by Umklapp process [Lee et al. (1974)]. When V_0 is large, then the allowed values of ϕ are integer multiples of $2\pi/M$. Expanding the cos potential up to second

order, and ignoring the amplitude fluctuations, we have

$$F = F_0 + \int d\vec{x} \left[\frac{1}{2} c \left(\vec{\nabla} \phi \right)^2 + \frac{1}{2} V_0 M^2 \phi^2 \right]. \tag{1.11}$$

This means that dispersion is massive, and the phase-phase correlation decays exponentially implying long-range order even for $D \leq 2$. This is because that the strong potential makes the continuous U(1) symmetry into $\mathcal{Z}_M$. As the potential becomes weak, or the thermal fluctuations are large, however, then such a pinning stops working, and then the U(1) symmetry recovers.

The electron-electron interactions can also generate backscattering. For $D \geq 2$, the backscattering is irrelevant and not important in general. Instead forward scattering turns the system into a Landau's Fermi liquid, and determines the Landau parameters [Shankar (1994); Schulz et al. (2000)]. On the other hand, in one dimension, forward scattering makes the system Tomonaga-Luttinger liquids [Tomonaga (1950); Luttinger (1963)], and characterizes it by Luttinger parameters. The first order of backscattering is marginal for non-interacting electrons, while the forward scattering can make the backward scattering relevant. Hence, we cannot ignore the backscattering in one dimension. For example, for electrons in one dimension at half-filing, the backscattering generates a term like

$$g_1 \cos(\sqrt{8}\phi_\sigma) + g_3 \cos(\sqrt{8}\phi_\rho), \tag{1.12}$$

where $\phi_{\rho(\sigma)}$ are the phase for the charge (spin) density waves respectively. These terms again tend to pin the phase as the commensurate potential as we saw above. However, at low-temperatures, quantum fluctuations become important. In particular, when there are other scattering processes, quantum fluctuations usually lead to a non-trivial fixed point. We will discuss in detail the effects of such complexity arising from the orbital degeneracy in one dimension in Chap. 2 [Okamoto and Millis (2011, 2012)].

This work is motivated by the recent success of fabricating one-dimensional transition metal wires [Wang et al. (2008); Zaki et al. (2013)], and we consider a one-dimensional Hubbard model with orbital degeneracy having various electron-electron interactions, in particular a Hund coupling preferring a locally high-spin state. Such a interaction distinguishes our model from the previously studied two-leg ladder models, which prefer locally low-spin states.

Finally, another source of backscattering is disorder. In a real crystal, there are always defects or impurities to some extent. For a CDW compound, the effects of impurities are quite important to understand both static and dynamic properties of the CDW phase. For example, the nonlinear transport and current oscillations, which are often observed in CDW systems, are attributed to the effect of impurity pinning [Grüner (1988)]. Impurities are expressed as an electrostatic potential $v(\vec{x})$, and they are linearly coupled to the CDW density,

$$H_{\text{imp}} = \int d\vec{x} v(\vec{x}) \delta\rho_{\text{CDW}} = \sum_i \int d\vec{x} V(\vec{x} - \vec{R}_i) \delta\rho_{\text{CDW}}. \tag{1.13}$$

$\vec{R}_i$ is the position of the $i$the impurity. Using Eqs. (1.4) and (1.5), we find

$$H_{\text{imp}} = \int d\vec{x} v(\vec{x}) \left[\frac{e}{\pi} \nabla\phi + \rho_1 \Re \left(\psi e^{i\vec{Q}\cdot\vec{x}} \right) \right]. \tag{1.14}$$

The term coupling the impurity and the slow density modulation $\nabla\phi$ is not important; they are irrelevant for $D > 2$, and actually can be eliminated by a translation of the phase variable [Bak and Brazovsky (1978); Giamarchi and Le Doussal (1995)]. Thus, it does not destroy the long-range order. On the other hand, it is known that the last term, from a general argument presented in the next section, destroys the long-range order even with an arbitrary small impurity potential for $D < 4$. Therefore, we will focus on the second term in the following. For charged impurities, the impurity

energy becomes

$$\begin{aligned} H_{\text{imp}} &= \sum_i \rho_1 \Re \int d\vec{x} V(\vec{x}) \psi e^{i\vec{Q}\cdot(\vec{x}+\vec{R}_i)} \\ &= \sum_i \Re\rho_1 \int \frac{d\vec{p}}{(2\pi)^D} e^{i(\vec{p}+\vec{Q})\cdot\vec{R}_i} v(-\vec{p}-\vec{Q})\psi(\vec{p}) \\ &\sim \sum_i \Re\rho_1 e^{i\vec{q}\cdot\vec{R}_i} v(-\vec{Q})\psi(0), \end{aligned} \tag{1.15}$$

where we used the fact that ψ is a slowly varying object compared to Q. The Fourier component is given by $v(Q) = [4\pi e^2/\epsilon_\infty(Q)]Q^{-2}$, where $\epsilon_\infty(Q)$ is the dielectric function. For a large Q, screening is not significant, and thus charged impurities have a strong potential of the order of eV, while isoelectric impurities are presumably much weaker [Lee and Rice (1979)]. The total free energy below T_c^{MF} is found to be ($\psi = \sqrt{|t|}e^{i\phi_0} + \chi e^{i\phi_0}$)

$$F = f \int d\vec{x} \left\{ 2|t|\chi_1^2 + \xi^2 \left[\left(\vec{\nabla}\chi_1\right)^2 + \left(\vec{\nabla}\chi_2\right)^2 \right] \right\} + \int d\vec{x} v(\vec{x}) \rho_1 \Re \left(\psi e^{i\vec{Q}\cdot\vec{x}} \right). \tag{1.16}$$

1.4 Charge-density waves with impurities

In this section, we will give a brief overview about the impurity effects on charge-density waves. First, we present basic arguments about the effects starting from a single impurity embedded in a CDW. We then discuss that the result given by the basic arguments for many impurities is not self-consistent, and how the contradiction was resolved. We also mention several open problems related to our study in Chap. 3.

1.4.1 Basic arguments

Let us think about the effect of a single local impurity, $v(\vec{x}) = -|V|\delta(\vec{x})$, as a starting point. The phase which the impurity prefers is 0, while at the infinity the order parameter goes back to $\sqrt{|t|}e^{i\phi_0}$. Ignoring the thermal fluctuation, we would like to minimize the energy (1.16). As a result, we obtain

$$\begin{aligned} \frac{\delta F}{\delta \chi_1} &= f\left(4|t|\chi_1 - 2\xi^2\vec{\nabla}^2\chi_1\right) - |V|\rho_1\delta(\vec{x})\cos\phi_0 = 0. \\ \frac{\delta F}{\delta \chi_2} &= -2f\xi^2\vec{\nabla}^2\chi_2 + |V|\rho_1\delta(\vec{x})\sin\phi_0 = 0. \end{aligned} \tag{1.17}$$

Solving the differential equations with a boundary condition $\chi(\infty) = 0$, we find

$$\chi_1 = -\epsilon\cos\phi_0\frac{\xi}{|x|}e^{-\frac{|x|}{\xi'}}, \tag{1.18}$$

$$\chi_2 = \epsilon\sin\phi_0\frac{\xi}{|x|}, \tag{1.19}$$

where $\xi' = \xi/\sqrt{2|t|}$, and $\epsilon = |V|\rho_1/(8\pi f\xi^3)$. At small x, we must think that there is a short distance cut-off, since any impurity has a finite size. The solution indicates that the amplitude decays exponentially with the decay length with ξ', while the phase variation is long-ranged as Coulombic. Thus, we will mostly focus on the phase fluctuation ignoring the amplitude modulation appearing only near the impurity sites. For a weak potential $\epsilon \ll \sqrt{|t|}$, the elastic energy cost is $\sim \phi_0^2|t|f\xi^3$, since the phase changes from ϕ_0 at $x = \infty$ to 0 at $x = \xi$ in a power-law fashion $\sim 1/x$. On the other hand, the impurity energy gain is $\sim \rho_1|V|\sqrt{|t|}$. Therefore, for $\epsilon \ll \sqrt{|t|}$, a single impurity does not pin the phase.

Although a single impurity is not enough to pin the phase of a CDW when $\epsilon \ll \sqrt{t}$, Larkin (1970) noticed that a collection of impurities may pin the phase. He assumed that the phase fluctuation is small, so that the expansion of the impurity potential is

a good approximation in a weak coupling limit,

$$v(\vec{x})\cos\left[\phi(\vec{x})+\vec{Q}\cdot\vec{x}\right]\simeq -v(\vec{x})\sin(\vec{Q}\cdot\vec{x})\phi(\vec{x})+\cdots\equiv F(\vec{x})\phi(\vec{x})+\cdots . \tag{1.20}$$

This term represents the random force coupling linearly on the phase. When we ignore the amplitude fluctuation, we can integrate over the disorder potential, and find

$$\begin{aligned}\langle[\phi(L)-\phi(0)]^2\rangle &\sim \left(\frac{L}{L_c}\right)^{4-D} \quad \text{with} \quad L_c\sim\frac{\sigma_F^2}{\xi^2 t},\\ \langle\delta\rho(L)\delta\rho(0)\rangle &\sim e^{-\left(\frac{L}{L_c}\right)^{4-D}}.\end{aligned} \tag{1.21}$$

σ_F is the standard deviation of the random force F. This indicates that the order parameter correlation function decays exponentially with an arbitrary small impurity potential, and leads to short-range order for $D<4$. The same conclusion was derived by Imry and Ma (1975), and Sham and Patton (1976) in the context of a continuous spin model.

Fukuyama and Lee (1978) reached the same conclusion by the following simple scaling argument. They considered that the system consists of domains of length L where the phase is coherent. Between different domains, the phase varies by the order of π, so the elastic energy density is $E_{\rm el}\sim ft(\xi/L)^2$. The average value of the phases that impurities in the domain prefer is 0 (or undetermined). However, since the domain is finite, there is always a fluctuation of size $\sqrt{n_i L^D}$ (n_i: the impurity density), such that we can choose the phase which takes advantage of this. The total energy density is thus found to be

$$\frac{E}{L^D}\sim\frac{ft}{4}\left(\frac{\xi}{L}\right)^2-|V|\sqrt{\frac{n_i}{L^D}}. \tag{1.22}$$

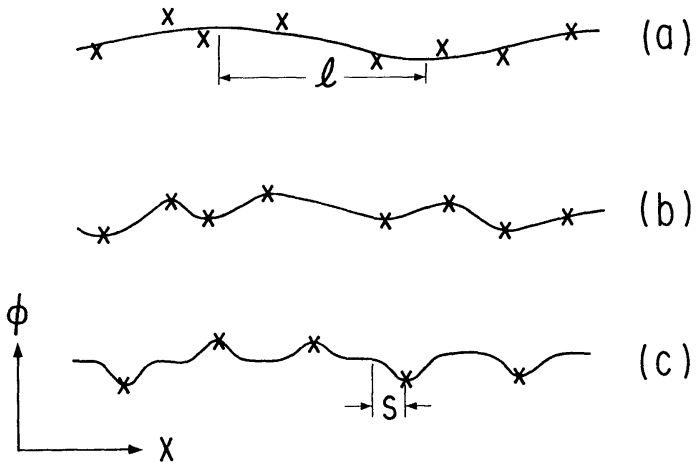

Figure 1.3: Schematic pictures of three different pinning scenarios [reproduced from Abe (1986)]. (a) Weak-pinning, (b) strong pinning when $\xi > l$, and (c) strong pinning when $\xi < l$.

Minimizing this by L gives us the optimal domain size L_0,

$$L_0 = \left(\frac{ft\xi^3}{D|V|\sqrt{n_i}}\right)^{\frac{2}{4-D}}, \quad \frac{E^*}{L_0^D} = \left(\frac{1}{4} - \frac{1}{D}\right)\left(\frac{ft\xi^2}{|V|\sqrt{n_i}D}\right)^{-\frac{4}{4-D}}. \tag{1.23}$$

Therefore, for $D < 4$, the total energy prefers to have a non-zero L_0, even for arbitrary small $|V|$. L_0 is called FLR length, or Larkin length. We note that the potential dependence of the energy $\sim V^4$ is different from the one $\sim V^2$ obtained by Efetov and Larkin (1977), who used a diagrammatic method, while the correlation length is the same for both cases. The difference comes from the fact that the FLR solution considers a constant phase in a domain, while the solution by Efetov and Larkin (1977) is a superposition of Coulombic forms.

For a strong impurity potential, it had been believed that the phase is completely fixed by impurities, and it is smoothly interpolated between the impurity sites (Fig. 1.3). In this case the correlation length is of the order of the average impurity distance. Abe (1985), later, noticed that this is not always the case. When the

coherence length is shorter than the inter-impurity distance l, we can modulate the phase in the vicinity of each impurity over the range of ξ, whose elastic energy is $\sim ft\xi^3$ as the single impurity case. Compared to the smooth interpolation of phase, whose energy is $\sim ftl^3$, such local modulation is more preferable when $\xi \ll l$. We expect that this phase profile leaves much larger phase coherent domains than l, and we will carefully study this scenario in Sec. 3.4. In the opposite limit, $l \gg \xi$, it is no longer possible to make such local modulation, and the phase profile looks as the conventional scenario.

Now we turn to the stability of the phase to topological defects such as vortices and dislocations. We will focus on the three dimensional case, since this is the relevant case for our later analysis of $NbSe_2$. The vortex cannot terminate inside the bulk, so the stable object in three dimensions is a vortex loop. The elastic energy is not important, since the contributions from the opposite sides of the loop cancel it. The important energy is the core energy of the vortex, which scales linearly in terms of the size of the loop L. By choosing the loop's location and orientation, the impurity energy inside the loop is optimized as in the Fukuyama-Lee argument; the energy scales as $L^{3/2}$. Balancing these two terms leads to the same conclusion as before, and the length scale of the domain and the vortex loops scales in the same manner. Therefore, the disordered state, which we expect from the scaling arguments for $l \ll \xi$, consists of phase coherent domains that are separated by the vortex loops of the same size. Since the vortex appears even in the weak pinning limit, there are many vortices in the strong pinning phase as well. The stability of the locally modulated phase appearing for $\xi \ll l$ to topological defects has not been studied, and we will study it in Chap. 3.

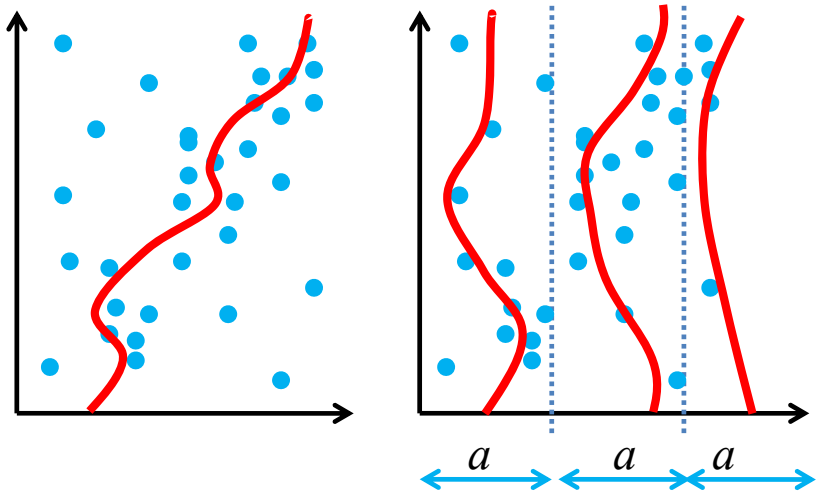

Figure 1.4: A schematic representation of an isolated elastic object (left) and a periodic media (right) subject to impurity pinning [reproduced from Giamarchi (2009)]. Lines are elastic objects, and dots are impurities. a is the lattice constant of the periodic media.

1.4.2 Bragg glass

In the late 1980s and early 1990s, people realized that the basic arguments given in the previous subsection becomes invalid at long distance [Feigel'man et al. (1989); Nattermann (1990); Bouchaud et al. (1991, 1992); Korshunov (1993); Giamarchi and Le Doussal (1994, 1995, 1997); Rosso and Giamarchi (2004)]. For example, the basic assumption for the Larkin's calculation was that the fluctuation of the phase is small such that the expansion of the impurity potential in terms of the phase is a good approximation. However, when $L > L_c$, the phase fluctuation becomes of the order of π, signaling the breakdown of the assumption.

Indeed, this approximation misses an important fact for a periodic media as follows. Fig. 1.4 sketches the difference between the effects of impurities on a single elastic object and a periodic elastic media. A single elastic object is, for example, a domain wall between different spin directions. When such an object is subject to

impurity potentials, the phase wanders such that the object optimizes the potential energy as the Larkin's argument. On the other hand, a periodic media such as a CDW consists of array of elastic objects aligned with an equal space λ. Thus, when the phase fluctuation of one object becomes comparable to π, this does not gain as much potential energy as the single isolated object; there is already another object enjoying the potential energy at distance λ. This naive physical picture indicates that the impurity effects are weaker than the one that Larkin considered when $L > L_c$ for a periodic media.

Indeed, using sophisticated methods such as functional renormalization group [Balents and Fisher (1993); Balents et al. (1996)] and replica method [Giamarchi and Le Doussal (1995)], it was shown that the phase fluctuation diverges only logarithmically

$$\begin{aligned} \langle [\phi(L) - \phi(0)]^2 \rangle &\sim \eta \log L, \\ \langle \delta\rho(L)\delta\rho(0) \rangle &\sim \frac{1}{L^\eta}. \end{aligned} \tag{1.24}$$

η is estimated as ~ 1, and presumably temperature independent. The correlation function of the order parameter decays by a power-law, and this gives a power-law diverging peak in the structure factor at the Bragg point, $S(\vec{p}) \sim p^{\eta-3}$; thus this phase is called a "Bragg glass".

The stability of a Bragg glass to generation of topological defects was studied by Gingras and Huse (1996) by Monte Carlo simulations. They showed that the Bragg glass phase does not have topological defects for a weak impurity potential. Above a certain threshold potential strength, the density of vortices becomes finite, and the autocorrelation of the order parameter decays exponentially.

A basic assumption for the discussion of the Bragg glass phase is that the impurity density is high and its pinning is weak. When the density is high and pinning is strong, the system is a disordered state. However, as we saw previously, the effects of the dilute, but strongly pinning impurities on a CDW are not so severe as had been

thought. Therefore, a natural question arising from these facts is that whether dilute, but strongly pinning impurities may exhibit a Bragg glass phase, or a disordered state. From experimental point of views, a new class of scanning tunneling microscopy (STM) measurements allows us to have detail examinations on states near impurities, and also the information about large field of views. Such an analysis of $NbSe_2$ based on a STM topographic image motivated us to study the impurity effects on a CDW, and prompted us to look at, in particular, the situation with dilute, but strongly pinning impurities [Okamoto et al. (2014)]. In Chap. 3, we will discuss the details of the analysis of the experimental data, and present several theoretical analysis to understand a behavior of CDW under such a situation.

1.5 Scanning tunneling microscopy

The development of scanning tunneling microscopy (STM) and spectroscopy (STS) techniques greatly accelerated the research of condensed matter physics [Wiesendanger (1994); Chen (2008)]. The conventional experimental techniques such as scattering or transport measurements can obtain only spatially averaged information. However, using STM, we can literally see the surface of samples at atomic levels over a wide field of view; both local information and spatially averaged information are available. Such features of STM are quite useful to study following systems in condensed matter systems:

1. One-dimensional systems: long-range order is often prohibited by thermal and quantum fluctuations as discussed in Sec. 1.3. However, a STM can observe such short-range order along with local spectroscopic information via STS.

2. Disordered systems: local information about defects and domain walls are available from STM.

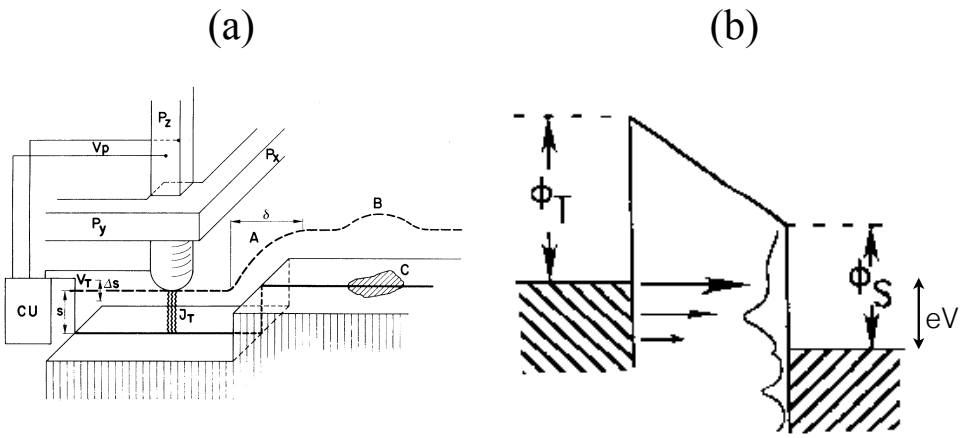

Figure 1.5: (a) Schematics of a STM [reproduced from Binnig et al. (1982)]. s is the tip-sample distance. V_T and J_T are the tunneling voltage and current. (b) Density of states (DoS) and tunneling between the sample and the tip [reproduced from Hamers (1989)]. The left side is the DoS of the tip with a work function ϕ_T. The right side is the sample's DoS (vertical curve) with a work function ϕ_S. The hatched region is occupied, and the arrows are tunneling rates.

Related to the first kind, in Chap. 2, we consider Co nanowires fabricated on a stepped copper surface. A STM study revealed that the Co nanowires show a dimerization below 100K. In Chap. 3, we focus on the second aspect, and study the disorder effects on the CDW phase of 2H-$NbSe_2$.

Now we briefly explain the principle of STM [Chen (2008)], since the data analysis in Chap. 3 requires some of the knowledge explained here. Fig. 1.5 shows a schematic set-up of STM. Using the Fermi's Golden rule, the tunneling current from the tip to the sample is

$$I_{\mathrm{t}\to\mathrm{s}} = -\frac{4\pi e}{\hbar}\int_{-\infty}^{\infty} d\epsilon \left\{ f(-eV+\epsilon)\rho_{\mathrm{t}}(-eV+\epsilon) \times [1-f(\epsilon)]\,\rho_{\mathrm{s}}(\epsilon) \times |M|^2 \right\}, \quad (1.25)$$

where the energy is measured from the Fermi energy of the sample, and M is the transition probability matrix from the tip to the sample. $f(\epsilon)$ is the Fermi distribution function, and $\rho_{\mathrm{t(s)}}$ is the density of states of the tip (sample). Similarly, for the current from the sample to the tip is

$$I_{\mathrm{s}\to\mathrm{t}} = -\frac{4\pi e}{\hbar}\int_{-\infty}^{\infty} d\epsilon \left\{ [1 - f(-eV+\epsilon)]\, \rho_{\mathrm{t}}(-eV+\epsilon) \times f(\epsilon)\rho_{\mathrm{s}}(\epsilon) \times |M|^2 \right\}. \quad (1.26)$$

The total current is

$$I = \frac{4\pi e}{\hbar}\int_{-\infty}^{\infty} d\epsilon \left\{ [f(\epsilon) - f(-eV+\epsilon)]\, \rho_{\mathrm{t}}(-eV+\epsilon)\rho_{\mathrm{s}}(\epsilon) \times |M|^2 \right\}. \quad (1.27)$$

The two realistic assumptions for experimental environments are: (a) temperature dependence is ignorable in $f(\epsilon)$, and (b) the density of states of the tip is nearly constant around the Fermi energy. These assumptions significantly simplify the expression, and we finally have

$$I \approx -\frac{4\pi e}{\hbar}\rho_{\mathrm{t}}\int_{0}^{eV} d\epsilon \rho_{\mathrm{s}}(\epsilon)|M|^2. \quad (1.28)$$

The tunneling matrix M in general depends on the energy ϵ. If we can ignore the energy dependence, and assume a s-wave tip, $|M|^2$ is approximated as

$$|M|^2 \approx e^{-2\frac{\hbar}{\sqrt{2m\varphi}}s}, \quad (1.29)$$

where m is the electron mass, φ is the difference of work functions between the sample and the tip, and s is the tip-sample distance.

The two modes of operations are (a) the topographic mode, and (b) the spectroscopic mode. The topographic mode uses a constant voltage and current adjusting the tip-sample distance to maintain the integrated DoS constant. Without spatial inhomogeneity of DoS, the tip will keep the same distance from the sample. However,

with spatial modulation of DoS, the tip height will change accordingly. The spectroscopic mode changes the voltage, and measures the differential conductance at each spatial point:

$$\frac{dI}{dV} = -\frac{4\pi e}{\hbar}|M|^2\rho_{\mathrm{t}}\rho_{\mathrm{s}}(eV), \tag{1.30}$$

where we ignored the energy dependence of M. We can infer the local DoS suppose we know the matrix elements and ρ_{t}. For the full treatment of the energy dependent M, see Chen (2008).

Chapter 2

Charge-density waves in Co nanowires

2.1 Overview

In this chapter, we consider the physics of Co nanowires at low temperatures. In the first section, we explain experimental findings on this material from STM measurements, and discuss the theoretical problems. Then, in the second section, a model is introduced, and its symmetry is discussed. We present a mean-field analysis of the model in Sec. 2.4. The mean-field analysis captures the basic physics of the model, but ignores the quantum fluctuations. In Sec. 2.5, using bosonization and renormalization group, we analyze the same model incorporating the quantum fluctuations, and obtain phase diagrams. The case in which spins are polarized is separately discussed in Sec. 2.6. The indication of first principles calculations is also discussed. The last section is the summary and the discussion about the connection between theoretical results and experimental findings.

2.2 Background

Fabrication of one-dimensional atomic wires composed of adatoms confined at step edges on surfaces of substrates becomes possible due to self-assembly epitax-

ial techniques [Himpsel et al. (2001); Barth et al. (2005); Snijders and Weitering (2010)]. By choosing appropriate substrates, we can realize a situation where the bulk substrate bands are decoupled from the electronic states of the adatoms, leading to ideal one-dimensional systems. This class of materials can exhibit CDW order at low temperatures due to the Peierls instability. One example is Au nanowires grown on the Si(577) surface [Ahn and Yeom (2003); Yeom et al. (2005)]. The physics of Au nanowires is still a subject of debate, but it appears that the relevant band is Au s-states for which electron-electron interactions are relatively weak, and the dominant physics may be associated with lattice instabilities [Johannes and Mazin (2008)]. However, recent success of fabricating one-dimensional transition metal nanowires such as Co nanowires on a Cu(111) surface indicates that the electrons confined on the one-dimensional geometry come from the transition metal d-orbitals, and hence have strong electron-electron interactions. As we discussed in Chap. 1, naively the large repulsive interactions among electrons tend to suppress the formation of CDWs. However, a STM study on Co nanowires revealed that the system undergoes a transition to a dimerized state below 100K (Fig. 2.1) [Wang et al. (2008); Zaki et al. (2009, 2013)]. This apparent contradiction motivates us to investigate the ground state of the transition metal nanowires.

From a theoretical point of view, the important feature of transition metal nanowires is the orbital degeneracy of the transition-metal d-levels, which permits a rich set of strong on-site interactions. For a single atom, the five d-levels are degenerate. Once the atoms form a crystal or put on a surface, the rotational symmetry is broken such that the degeneracy is lifted. In other situations, the orbital ordering occurs and shifts some of the d-levels upward or downward. These effects thus reduce the number of orbitals crossing the Fermi surface. Hence we consider a system with two transition metal orbitals for the sake of simplicity. Similar models involving two orbitals per unit cell has been previously considered in the literature, both for their

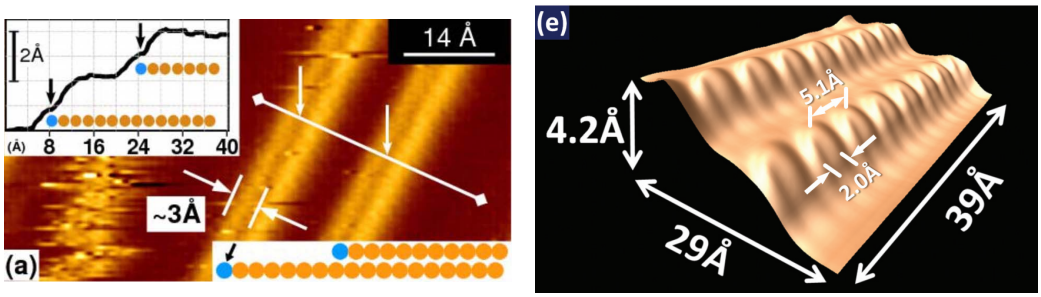

(a) at room temperature (b) at 5 K

Figure 2.1: Topographic pictures of Co nanowires on Cu(111) surface (a) at room temperatures, and (b) at 5K [reproduced from Zaki et al. (2009, 2013)].

intrinsic interest [Schulz (1996)], and as steps toward understanding heavy fermion systems [Varma and Zawadowski (1985); Strong and Millis (1994); Fujimoto and Kawakami (1994)], high T_c superconductors [Fabrizio et al. (1992); Finkel'stein and Larkin (1993); Khveshchenko and Rice (1994); Balents and Fisher (1996); Shelton and Tsvelik (1996); Lin et al. (1998); Lee et al. (2005); Chudzinski et al. (2008)], spin ladders [Shelton et al. (1996); Kim et al. (2000)], and Hubbard ladders [Azaria et al. (1999); Tsuchiizu and Furusaki (2002a); Wu et al. (2003)]. In these models, the multiple bands arise from physically different atoms: In the heavy fermion case, one band represents the local moments and the other the wide band of conduction electrons; in the high T_c case an important motivation has been models of "spin ladders". Although we expect some qualitative aspects of these models also apply to the model of interests here, the orbital degeneracy, which is specific to the transition metal nanowires, leads to different physical behaviors. In particular, the Hund coupling favors locally high spin configurations, potentially leading to interesting spin structures. We also find that the pair-hopping term, which has been often ignored in the past studies, is

important to retain a unique orbital symmetry. Once the orbital degeneracy is broken, in general the velocities between orbitals are also different. Such effects has been ignored in most of the past study, but are also investigated in our analysis. Finally, we discuss possibility of magnetic ordering or orbital ordering driven by the strong local interactions [Roth (1966); Penn (1966); Kugel and Khomskii (1972); Cyrot and Lyon-Caen (1975); Gill and Scalapino (1987); Sakamoto et al. (2002)].

2.3 Model

2.3.1 One-dimensional two-orbital Hubbard model

We start from a multi-orbital Hubbard-like model representing the Co d-orbitals with local onsite Coulomb interactions

$$H = \sum_{\langle i,j \rangle} \sum_{m,s} -t_{ij}^{mm'} \left(c_{ims}^{\dagger} c_{jm's} + \text{H.c.} \right) + H_{\text{int}}. \tag{2.1}$$

Here $c_{ims}^{(\dagger)}$ is the annihilation (creation) operator for a d-electron in orbital m with spin s at site i. $t_{ij}^{mm'}$ is the hopping between from orbital m on site i to orbital m' on site j. The interaction terms H_{int} will be discussed below. We set the lattice constant equal to unity. The presence of the surface breaks the symmetry between d levels and may lead to an arbitrary ionization level. For the sake of simplicity, we will consider here only the case where the Fermi energy crosses two orbitals, $m = A, B$, although in the general case one could have up to five d-derived bands with an arbitrary Fermi energy. Furthermore, the rotational symmetry in H_{int} as we will see always allows us to diagonalize the hopping matrix, so we will ignore t^{AB}.

In the weak coupling limit, the band structure is characterized by four Fermi points: two Fermi momenta, k_A and k_B, and two chiralities, $r = R, L$. R (L) represent

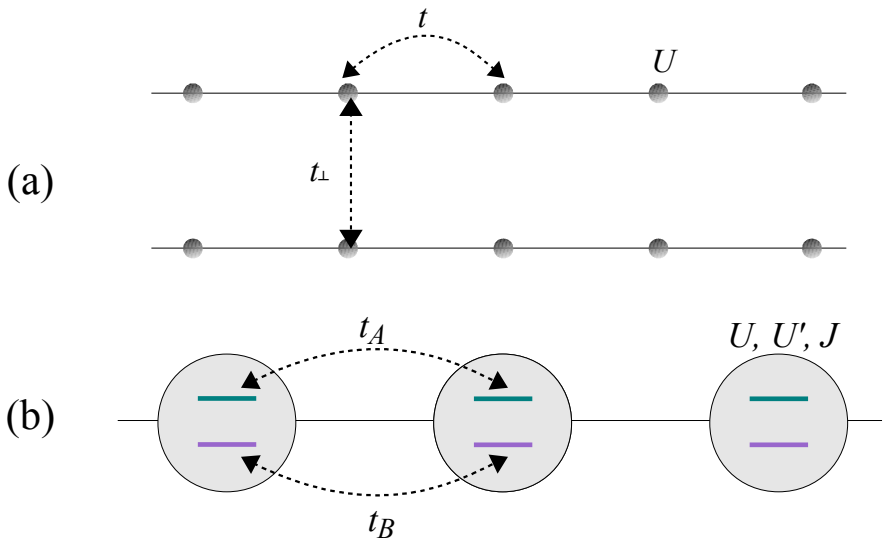

Figure 2.2: (a) Schematic of two-leg ladder models. (b) Schematic of two-orbital Hubbard model [reproduced from Okamoto and Millis (2011)].

electrons around positive (negative) Fermi momenta. The total particle number is $n = 2(k_A + k_B)/\pi$. In principle there are five possible cases, which are summarized in Table 2.1. In cases (a) and (b), the two Fermi momenta are equal, and the filling is commensurate and incommensurate respectively. In cases (c) and (d), the two Fermi momenta are different, while (c) is at half filling, and (d) is away from half filling. Finally in case (e), one band is commensurate and the other is not, allowing an orbital selective Mott state. When two bands have equal Fermi momenta and Fermi velocities, the kinetic term acquires O(3) $\simeq$ SU(2) orbital symmetry; this orbital symmetry is explicitly broken with interactions we consider below.

For the two-orbital system the interaction terms have the following form:

$$H_{\rm int} = U \sum_{i,m} n_{im\uparrow} n_{im\downarrow} + U' \sum_{i,s} n_{iAs} n_{iB\bar{s}} + (U' - J) \sum_{i,s} n_{iAs} n_{iBs} - J \sum_{i,s} c^\dagger_{iAs} c_{iA\bar{s}} c^\dagger_{iB\bar{s}} c_{iBs} + J' \sum_i \left(c^\dagger_{iA\uparrow} c^\dagger_{iA\downarrow} c_{iB\downarrow} c_{iB\uparrow} + \text{H.c.} \right), \quad (2.2)$$

where $n_{ims} = c^\dagger_{ims} c_{ims}$ is the electron density and $\overline{s} = -s$. U and U' indicates on-site Coulomb repulsion between two electrons in the same band or different bands, and J represents Hund coupling favoring high spin states. J' is the so-called pair-hopping term. We assume that the symmetry breaking by substrate primarily affects the hopping terms in the Hamiltonian without changing the local orbitals too much. This enables us to use free-space rotation symmetries to reduce the number of interaction constants [Dagotto et al. (2001)] In this case we have

$$J = J', \tag{2.3}$$

$$U = U' + 2J. \tag{2.4}$$

The first equality is derived from the fact that Wannier wave functions are real, and the second one represents rotational invariance in orbital space. With this simplification, the interaction terms now have $U(1)$ orbital rotational symmetry about y axis. To show the symmetry explicitly, we introduce the following charge, spin, and orbital (pseudospin) operators:

$$n_i = \sum_{ms} n_{ims}, \tag{2.5}$$

$$\boldsymbol{S}_i = \frac{1}{2} \sum_{mss'} c^\dagger_{ims} \boldsymbol{\sigma}_{ss'} c_{ims'}, \tag{2.6}$$

$$\boldsymbol{T}_i = \frac{1}{2} \sum_{mm's} c^\dagger_{ims} \boldsymbol{\tau}_{mm'} c_{im's}, \tag{2.7}$$

where $\boldsymbol{\sigma}$ and $\boldsymbol{\tau}$ are Pauli matrices. Then, the interactions in terms of U and J are given by

$$H_{\text{int}} = \sum_i \left(\frac{U}{2} n_i^2 + J \boldsymbol{S}_i^2 + 3J \boldsymbol{T}_i^2 - 2J (T_i^y)^2 - \frac{U + 5J}{2} n_i \right). \tag{2.8}$$

For a transition metal ion in free space, $U \gg J > 0$, so that all interaction parameters

are positive. Screening will reduce the value of U, but will lead to only negligible changes in J [Aryasetiawan et al. (2006)], and most calculations indicate that even the reduced value of U is greater than J.

As we mentioned earlier, this specific form of interactions between orbitals give different physics compared to the extensively studied two-leg ladder models (Fig. 2.2). Both the two-leg ladder models and our model have two orbitals per unit cell in one dimension (two sites on the same rung on the ladder or two atomic orbitals). However, the two-leg ladder models in general, have a transverse hopping $t_\perp$ along the rung of the ladder, which effectively generate an antiferromagnetic coupling ($-t_\perp^2/U < 0$) under the presence of the onsite interaction U. Thus, the two electrons on the same rung tend to form a spin singlet. On the other hand, our model does not have a transverse hopping, since the two orbitals are orthogonal. Instead, the Hund coupling favors a locally high-spin state.

2.3.2 Symmetry

Now we discuss the symmetry of our Hamiltonian at the bare level. When $J = 0$, the interaction term possesses $\mathrm{U}(1)_c \times \mathrm{SU}(4)_{s,o} \times \mathcal{Z}_2$; the indices "$c$", "$s$", and "$o$" denote the charge, spin and orbital parts, and the $\mathcal{Z}_2$ symmetry refers to the interchange of orbitals. When $J \neq 0$, the symmetry of the spin-orbital part is broken to $\mathrm{SU}(2)_s \times \mathrm{U}(1)_o$. We'd like to emphasize that in our convention, the U(1) axis is the orbital y-axis, wheres it is orbital z-axis in the convention of Nonne et al. (2010) and Lee et al. (2004). Only if $v_A = v_B$ and $k_A = k_B$, as in cases (a) and (b), does the total Hamiltonian have the same symmetry as the interaction. Otherwise, including cases (c)–(e), the total symmetry is reduced to $\mathrm{U}(1)_c \times \mathrm{SU}(2)_s$ at the bare level due to the lower symmetry of the kinetic term. However, it is known that low-energy theories in weak-coupling still have an effective $\widetilde{\mathrm{U}(1)}_o$ symmetry [Lin et al. (1998); Controzzi

Case	Fermi momentum	n	symmetries
(a)	$k_A = k_B$	$= 2$	$\mathrm{U}(1)_c \times \mathrm{SU}(2)_s \times \mathrm{U}(1)_o \times \mathcal{Z}_2$
(b)	$k_A = k_B$	$\neq 2$	$\mathrm{U}(1)_R \times \mathrm{U}(1)_L \times \mathrm{SU}(2)_s \times \widetilde{\mathrm{U}(1)}_o \times \mathcal{Z}_2$
(c)	$k_A \neq k_B$	$= 2$	$\mathrm{U}(1)_c \times \mathrm{SU}(2)_s \times \widetilde{\mathrm{U}(1)}_o$
(d)	$k_A \neq k_B$	$\neq 2$	$\mathrm{U}(1)_R \times \mathrm{U}(1)_L \times \mathrm{SU}(2)_s \times \widetilde{\mathrm{U}(1)}_o$
(e)	$k_A \neq k_B = \pi/2$	$\neq 2$	$\mathrm{U}(1)_c \times \mathrm{SU}(2)_s \times \widetilde{\mathrm{U}(1)}_o$

Table 2.1: Possible band structures in the two-orbital Hubbard model, and its symmetry at $v_A = v_B$. $\mathrm{U}(1)_r$ represents a gauge transformation of particles with chirality r.

and Tsvelik (2005); Boulat et al. (2009); Nonne et al. (2010)] at least if $v_A = v_B$. We will see this in detail later using bosonization.

2.4 Mean-field analysis

2.4.1 Method

We employ the standard Hartree-Fock approximation, assuming the deviation from the mean value of the operator is small:

$$\begin{aligned} \hat{A}\hat{B} &= \left(\hat{A} - \langle\hat{A}\rangle + \langle\hat{A}\rangle\right)\left(\hat{B} - \langle\hat{B}\rangle + \langle\hat{B}\rangle\right) \\ &\simeq \langle\hat{A}\rangle\hat{B} + \langle\hat{B}\rangle\hat{A} - \langle\hat{A}\rangle\langle\hat{B}\rangle, \end{aligned} \tag{2.9}$$

where $\langle\hat{A}\rangle$ and $\langle\hat{B}\rangle$ are determined by minimizing the energy. $\hat{A}$ and $\hat{B}$ are chosen to be various fermion bilinears discussed in the next subsection. These expectation values correspond to (quasi-) long-ranged orders[1] induced either by forward scattering

[1] In purely one-dimensional system, there is no long-range order corresponding to spontaneous symmetry breaking of continuous symmetry. In the mean field approximation, ordering tendency is overestimated leading to fictional long-range order.

or by backscattering. In the weak coupling regime, we focus on only the backscattering terms, since Stoner's scenario of phase transitions driven by forward scattering requires a coupling to be larger than a critical value [Stoner (1938)], although the backscattering always opens a gap even in the weak coupling limit in one dimension.[2]. In the strong coupling regime, we assume that the forward scattering drives the system to some kind of density polarization and study the effect of backscattering on each polarized state. We will not consider partially polarized states, which might appear between a non-polarized state and a fully polarized state, because the possible intermediate phases are complicated and depend sensitively on details. Thus, we focus on a treatment of backscattering here. We also assume a constant density of states (DoS). Although the detailed form of DoS is important to determinate the phase boundary between strong coupling phases and weak coupling phases, this approximation is justified within each regime: In the strong coupling regime, kinetic terms are less important than interactions; in the weak coupling regime, electrons far away from the Fermi energy is irrelevant.

We first focus on a single band case. The quadratic Hamiltonian obtained by a mean-field approximation can be diagonalized, and the system is gapped at the Fermi energy ϵ_F. Using the energy ϵ measured from ϵ_F, the new dispersion is found to be,

$$\pm \sqrt{\epsilon^2 + g^2\Delta^2} \tag{2.10}$$

where Δ is an order parameter or a fermion bilinear, and g is the corresponding coupling constant. Under the assumption of constant DoS, the energy gain by this gap is given by

$$\delta E = \nu \int_{-\Lambda}^{0} \left(\epsilon + \sqrt{\epsilon^2 + g^2\Delta^2}\right) d\epsilon - g\Delta^2, \tag{2.11}$$

[2] This is not always true if we consider quantum fluctuations. For example, a finite value of U is necessary to open a gap at SU(4) symmetric point with $J = 0$ [Assaraf et al. (1999)].

where ν is the density of states for a single band, and Λ is the cutoff or bottom of the band. The values of these parameters are different in the weak coupling and strong coupling regimes, as we will explain below. The second term in Eq. (2.11) comes from the decomposition of quadratic terms [see Eq. (2.9)], and represents the energy increase by the ordering.

By maximizing the energy gain in terms of Δ, we get the analytical solution to the gap equation,

$$\Delta = \frac{\Lambda}{g} \sinh^{-1}\left(\frac{2}{\nu g}\right). \tag{2.12}$$

The stability condition for the ordered phase is $g > 0$. In order to obtain the phase diagram, we compare the energies of possible phases, and choose the order that gives the smallest energy as the ground state. Thus, phase boundaries indicate first-order transitions from one minimum to another without coexistent regions.

In the weak coupling limit ($g \to 0$), Eq. (2.12) is reduced to

$$\Delta \to \frac{2\Lambda}{g} e^{-\frac{2}{\nu g}}, \tag{2.13}$$

and the energy gain for single band by gap opening is found to be

$$\delta E \sim \nu g^2 \Delta^2. \tag{2.14}$$

The density of states is fixed to be the value at the Fermi energy, and the cutoff Λ is taken to be small compared to the band width $4t$.

In the strong coupling limit, as a constant density of states, we will use the averaged value for the tight binding dispersion, $\nu = 1/(4t)$, since most of the electrons participate in density-wave formation in the strong coupling limit. The energy of each state consists of two parts: static energy, and energy reduced by backscattering. The former is simply given by the sum of kinetic terms, and the static density-density interaction. As we take the constant DoS to be $1/(4t)$, the kinetic term becomes

$2tn(n-1)$ with particle density n in each band. The reduction of energy by density wave formation is obtained from Eq. (2.11). In particular, in the limit of $g \to \infty$, it becomes

$$\delta E \sim \frac{1}{4} g \nu^2 \Lambda^2 - \frac{1}{2} \nu \Lambda^2 + \cdots , \tag{2.15}$$

with

$$\Delta \sim \nu \Lambda \left(\frac{1}{2} - \frac{1}{3\nu^2 g^2} \right) + \cdots . \tag{2.16}$$

The backscattering tries to use all the electrons to form a density wave in the strong coupling limit, so the cutoff Λ in Eq. (2.11) is taken as the energy of band bottom.

Finally, we also consider the case where the ordering vector is $q = \pi$ involving Umklapp processes, while the Fermi momenta is not $\pi/2$. Calculations very similar to those leading to Eqs. (2.11) and (2.12) give the following results for $q = \pi$ orderings in a single band with $n < 1/2$. The ground state energy is given by

$$E_{\rm GS} = \nu \int_{-2t}^{-2t(1-2n)} \left(-\sqrt{\epsilon^2 + g'^2 \Delta^2} \right) d\epsilon + g' \Delta^2 + (\text{static interaction energy}), \tag{2.17}$$

with $\nu = 1/(4t)$. We used $g' = 2g$ to emphasize that the coupling constant is doubled at $q = \pi$ due to Umklapp processes, while static energy from the $q = 0$ part is just with g. The kinetic energy for $n > 1/2$ can be obtained by the particle-hole symmetry. The solution for the gap equation is found to be

$$\Delta = \frac{2t}{g' \sinh\left(\frac{2}{\nu g'}\right)} \sqrt{(2n-1)^2 + 1 + 2(2n-1)\cosh\left(\frac{2}{\nu g'}\right)}. \tag{2.18}$$

This goes to $n/2$ in the strong coupling limit. The solution exists only when the density is close to half-filling, $n_c < n < 1 - n_c$, with

$$n_c = \frac{1}{2} \left(\sqrt{\cosh^2\left(\frac{2}{\nu g}\right) - 1} - \cosh\left(\frac{2}{\nu g}\right) + 1 \right). \tag{2.19}$$

This becomes $1/2$ at $g \to 0$, and goes to 0 as $g \to \infty$. Thus, at intermediate coupling, the density wave with $q = \pi$ is stable only around half-filling.

When multiple bands are involved, the calculation becomes more tedious. Now the coupling constant g in Eq. (2.10) is expressed by some linear combinations of U and J. Complete list of coupling constants expressed by U and J is given in Table 2.2. Note that there exist contributions from Umklapp processes at half-filling, and extra interband scattering when $k_A = k_B$. In our two-band model, the important possibilities are: two bands have the same order independently by intraband scattering, or two bands have an order by interband scattering. For the former case, Eq. (2.11) remains the same where ν is the density of states for each band, and the total energy only depends on the averaged density of states, $\nu_{\text{intra}} \equiv (\nu_A + \nu_B)/2$. For the latter case, the dispersion becomes more complicated in general, though the final result depends only on a single parameter, $\nu_{\text{inter}}^{-1} = (\nu_A^{-1} + \nu_B^{-1})/2$. Thus, there is an in-equivalence between interband and intraband density of states,

$$\nu_{\text{intra}} \geqslant \nu_{\text{inter}}. \tag{2.20}$$

Therefore different density of states leads to suppression of interband scattering. Since the density of states at the Fermi energy is connected to the Fermi velocity v, and it is given by $\nu = (2\pi v)^{-1}$, we see that the velocity difference suppresses interband processes from Eq. (2.20).

2.4.2 Order parameters

As mean-field order parameters, we take fermion bilinears characterized by the chirality, spin and orbital indices; thus in the model considered here there are particle-hole bilinears,

$$(\Delta_{\text{ph}})_{rr'}^{ss';mm'} = c_{rms}^{\dagger} c_{r'm's'} \tag{2.21}$$

and particle-particle bilinears,

$$(\Delta_{\rm pp})^{ss';mm'}_{rr'} = msc^{\dagger}_{rms}c^{\dagger}_{r'\overline{m's'}}, \tag{2.22}$$

where $c^{(\dagger)}_{rms}$ is the annihilation (creation) operator of electron with chirality r, orbital m, and spin s. When the momentum transfer q is zero, we have spatially uniform order such as ferromagnetism, ferroorbital order, and superconductivity. When $q \neq 0$, spatially non-uniform order such as density waves and Fulde-Ferrell-Larkin-Ovchinnikov (FFLO) or pair-density wave superconductivity appears. Combinations of $r = r'$ are irrelevant in a RG sense, while in the strong coupling they become important. We will use the following convenient basis to represent them,

$$\mathcal{O}^{ij}_{\rm ph} = \sum_{mm'ss'} \tau^{i}_{mm'}\sigma^{j}_{ss'}(\Delta_{\rm ph})^{ss';mm'} + \text{h.c.} \tag{2.23}$$

$$\mathcal{O}^{ij}_{\rm pp} = \sum_{mm'ss'} \tau^{i}_{mm'}\sigma^{j}_{ss'}(\Delta_{\rm pp})^{ss';mm'} + \text{h.c.} \tag{2.24}$$

where $i, j = (0, 1, 2, 3)$ and τ and σ are Pauli matrices with $\tau^0_{ab} = \sigma^0_{ab} = \delta_{ab}$. These transform as rank 2 tensors under SO(4) $\simeq$ SU(2)$_s\times$SU(2)$_o$ transformations; the SU(2)$_s$ rotations connect $\sigma^{1,2,3}$, and the U(1)$_o$ rotation (if it exists) connects τ^1 and τ^3. Thus, we take the quantization axis along z-direction for spins. As we will show below, in the mean-field treatment, the high spin states ($j = 3$) such as SDW states and triplet superconductivities appear in the phase diagrams, while in the bosonization treatment, these spin triplet combinations are excluded from the possible ground state.

The order parameters with $r = r'$ indicate that the momentum transfer is 0, i.e., spatially uniform density order. Considering the SU(2)$_s$ and possible U(1)$_o$ symmetry, here we only consider the cases with $i, j = 0, 3$ such that the fermion bilinears are diagonal in spin and orbital spaces. We may think about the off-diagonal orbital order

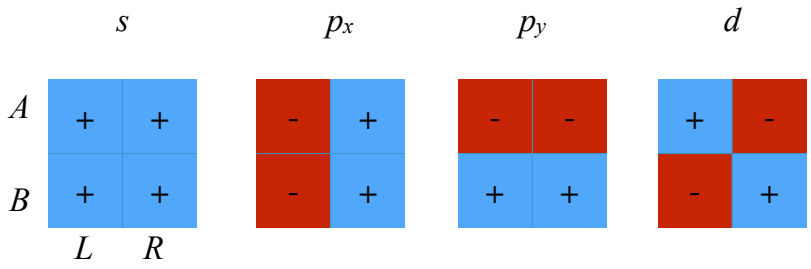

Figure 2.3: "Angular momentum" of order parameters and the phase at each Fermi point.

in general such as $(ic^{\dagger}_{rAs}c_{rBs'} + \text{h.c.})$ expressing an antibonding orbital occupancy. In that case, mean-field treatment generates an off-diagonal one-body term, and thus in order to solve the self-consistent equation, we need to diagonalize the non-diagonal dispersion matrix, which depends on the detail of the original dispersion. These lines are beyond the scope of our thesis. Thus, we focus on the simple diagonal cases. Due to the conservation of particles, the linearly independent diagonal order parameters are only ferromagnetism (FM), and orbital ferromagnetism (OFM):

$$\begin{aligned} \Delta_{\text{FM}} &= \langle n_{A\uparrow}\rangle - \langle n_{A\downarrow}\rangle + \langle n_{B\uparrow}\rangle - \langle n_{B\downarrow}\rangle \neq 0, \\ \Delta_{\text{OFM}} &= \langle n_{A\uparrow}\rangle + \langle n_{A\downarrow}\rangle - \langle n_{B\uparrow}\rangle - \langle n_{B\downarrow}\rangle \neq 0. \end{aligned} \tag{2.25}$$

For order parameters with $r \neq r'$, we label them by the transferred momentum and the sign at each Fermi point. Here we have four Fermi points each degenerate about spins, so, in principle, there are four possible cases (Fig. 2.3). We use s-wave when all four points have the same signs. p_x and p_y are odd under the inversion $R \leftrightarrow L$, and $A \leftrightarrow B$ respectively. d-wave is odd under both inversions. Applying this classification, we find that $i = 0, 1$ are both s-wave for the particle-hole channel, while the former is intraband type and the latter is interband type. We put " $'$ " for

an interband order to distinguish these two. $i = 2$ is found to be interband p_y-wave, and $i = 3$ is intraband p_y-wave. For the particle-particle channel, we found d'-, p_y-, s-, and s'-wave orders for $i = 0, \ldots, 3$ accordingly. Since p_x-wave does not appear in bosonization study, we will use p for p_y-wave orders when it is not confusing. We note that the d-wave superconductivity, which often appears in two-leg ladder models [Schulz (1996)], is the pSS state in our notation. The result is summarized in Table 2.3.

When a band is commensurate, we have another family of order parameters called "bond" order (BOW), which is basically the density-wave slid from on-site to"on-bond," and is the same as dimerization. The only difference between site order and bond order is the phase of the order parameter; Δ is real for on-site order, and imaginary for bond order. We found that the energy gain is maximized when the order parameter is real, indicating that always on-site orders have lower energy. Therefore, we will ignore the bond orderings for the mean-field calculations.

	$k_A \neq k_B \neq \pi/2$	$k_A \neq k_B = \pi/2$	$k_A = k_B \neq \pi/2$	$k_A + k_B = \pi$	$k_A = k_B = \pi/2$
CDW	$-U$	$-U, -2U$	$-3U + 5J$	$-3U + 5J$	$-6U + 10J$
SDW	U	$U, 2U$	$U + J$	$U + J$	$2U + 2J$
s'CDW	$U - 5J$	$U - 5J$	$U - 5J$	$2U - 10J$	$2U - 10J$
s'SDW	$U - J$	$U - J$	$U - J$	$2U - 2J$	$2U - 2J$
p'CDW	$U - 3J$	$U - 3J$	$U - 3J$	$2U - 6J$	$2U - 6J$
p'SDW	$U - 3J$	$U - 3J$	$U - 3J$	$2U - 6J$	$2U - 6J$
pCDW	$-U$	$-U, -2U$	$U - 5J$	$U - 5J$	$2U - 10J$
pSDW	U	$U, 2U$	$U - J$	$U - J$	$2U - 2J$
d'SS	$-U + J$	$-U + J$	0	$-U + J$	0
p'_yTS	$-U + 3J$	$-U + 3J$	$-2U + 6J$	$-U + 3J$	$-2U + 6J$
p_ySS	$-2U + 2J$	$-2U + 2J$	$-2U + 2J$	$-2U + 2J$	$-2U + 2J$
dTS	0	0	0	0	0
sSS	$-2U - 2J$	$-2U - 2J$	$-2U - 2J$	$-2U - 2J$	$-2U - 2J$
p_xTS	0	0	0	0	0
s'SS	$-U - J$	$-U - J$	$-2U + 2J$	$-U + J$	$-2U + 2J$
p'_xTS	$-U + 3J$	$-U + 3J$	0	$-U + 3J$	0

Table 2.2: Mean-field coupling constant for each phase.

(i,j)	Particle-hole order ($\mathcal{O}^{ij}_{\mathrm{ph}}$)	Particle-particle order ($\mathcal{O}^{ij}_{\mathrm{pp}}$)	P	L	S
$(0,0)$	Charge density wave (CDW)	d'-wave singlet SC(d'SS)	-1	0	0
$(0,3)$	Spin density wave (SDW)	p'_y-wave triplet SC (p'_yTS)	1	0	1
$(1,0)$	s'-wave charge density wave (s'CDW)	p_y-wave singlet SC (p_ySS)	1	1	0
$(1,3)$	s'-wave spin density wave (s'SDW)	d-wave triplet SC (dTS)	-1	1	1
$(2,0)$	p'_y-wave charge density wave (p'CDW)	s-wave singlet SC (sSS)	1	1	0
$(2,3)$	p'_y-wave spin density wave (p'SDW)	p_x-wave triplet SC (p_xTS)	-1	1	1
$(3,0)$	p_y-wave charge density wave (pCDW)	s'-wave singlet SC (s'SS)	1	1	0
$(3,3)$	p_y-wave spin density wave (pSDW)	p'_x-wave triplet SC (p'_xTS)	-1	1	1

Table 2.3: Classification of order parameters. " ' " indicates that the order is an interband type. The eigenvalues of each superconducting phase under parity (P), orbital rotation (L), and spin rotation (S), are also listed. The corresponding order parameters are given in Eqs. (2.21), (2.22), and (2.24). Particle-hole channels are even under parity.

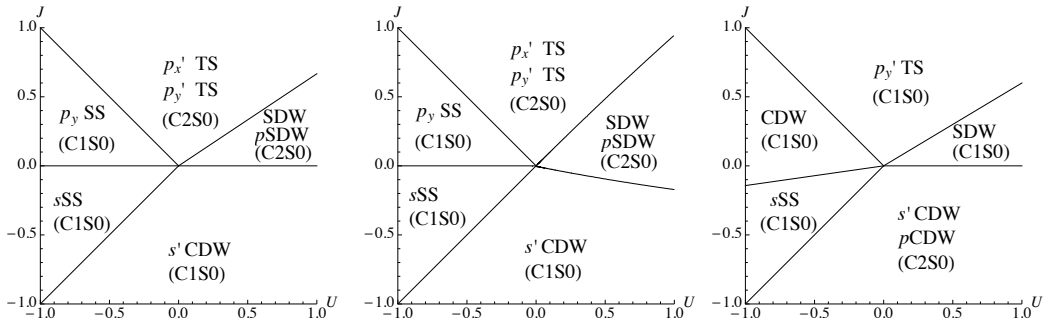

(a) $k_A \neq k_B \neq \pi/2$ (b) $k_A \neq k_B = \pi/2$ (c) $k_A = k_B \neq \pi/2$

Figure 2.4: Mean-field phase diagrams for incommensurate cases [reproduced from Okamoto and Millis (2011)].

2.4.3 Results

Here we present Hartree-Fock (HF) phase diagrams in the weak coupling regime. In order to obtain the phase diagrams, we compare the energy of possible phases, and choose the one with the lowest energy as the ground state. Along with the order parameter with (quasi-) long-range correlation, these phases are characterized by the number of gapless excitations in the charge and spin modes. We denote a system with m massless charge modes and n massless spin modes as $CmSn$ [Balents and Fisher (1996)]. Without any interaction, the original Hamiltonian has four bands and this corresponds to $C2S2$. We first explain the three cases away from half-filling, and then see the phase diagrams for systems at half-filling. For all the cases, the physically relevant parameter region is $U \gg J > 0$, although we investigated various parameter regions beyond this restriction.

First, we discuss the incommensurate cases, whose phase diagrams are given in Fig. 2.4. When $U \gg |J|$, the Coulomb repulsion U dominates the physics, and as in the one orbital Hubbard model [Overhauser (1960)] the ground state is a spin density

wave. In the generic case of two incommensurate Fermi wavevectors the phase of the spin density wave is not pinned between the two channels and there is a continuous family of solutions. When $k_A = k_B$, the relative phase mode is pinned down; there is no degeneracy here. The total charge mode and the relative charge mode are both massless in the degenerate SDW phase where both spin modes are massive. Thus, the degenerate SDW phase is expressed as $C2S0$. This represents two independent metallic spin-gapped chains of $C1S0$. The non-degenerate SDW phase in $k_A = k_B$ case has a massive relative charge mode so it becomes $C1S0$.

One notable feature for $J \gg |U|$ is that we have p-wave superconductivity, which is also observed in numerical calculation [Sakamoto et al. (2002); Shirakawa et al. (2008)] This is different from the case of two-leg ladder systems, where a purely repulsive Coulomb interaction leads to a spin-singlet d-wave superconducting ground state [Schulz (1996)]; the p-wave superconductivity is triggered by an attractive interaction. We can understand this by looking at the limit of $J \to +\infty$, where the spin on the same site is fully polarized, but an orbital degeneracy remains. So the only on-site interaction with dynamical consequences is $(U - 3J)n_{A\sigma}n_{B\sigma}$ in Eq. (2.2). By employing the knowledge that the negative-U Hubbard model has spin singlet superconductivity as the ground state [Auerbach (1994)], we find that the analogous ground state of this limit is the interband orbital singlet superconductivity with parallel spins, i.e., p'_yTS. The degeneracy of p'_yTS with p'_xTS arises from the absence of pinning effect between the two SCs as is the case for the SDW and pSDW states. When two Fermi momenta are not equal, these superconductivities show periodic modulation of order parameters in real space similar to that found in a FFLO state. At last, the degenerate p'_xTS and p'_yTS state is $C2S0$, and the non-degenerate p'_yTS state for $k_A = k_B$ is $C1S0$.

Next, we turn our attention to the negative U region, $-U \gg |J|$. When $|U|$ is large enough, it is naturally expected that attractive $U < 0$ gives some kind of

superconductivity; indeed, we found the p_ySS state for positive J, and the sSS state for negative J when two Fermi momenta are different. The p_ySS state is replaced to the CDW state when $k_A = k_B$. To understand these phases, here we consider two-particle local eigenstates. There are ${}_4C_2 = 6$ locally possible states. The spin triplet ($S = 1$) states are

$$\begin{aligned} |S=1, S_z=1\rangle &\equiv c^\dagger_{A\uparrow} c^\dagger_{B\uparrow}|0\rangle, \\ |S=1, S_z=0\rangle &\equiv \frac{1}{\sqrt{2}}\sigma^x_{ss'} c^\dagger_{As} c^\dagger_{Bs'}|0\rangle, \\ |S=1, S_z=-1\rangle &\equiv c^\dagger_{A\downarrow} c^\dagger_{B\downarrow}|0\rangle \end{aligned} \tag{2.26}$$

The on-site energy is $E_{S=1} = U - 3J$. Among the three spin singlet ($S = 0$) states, $U(1)_{\text{orbital}}$ doublet states are

$$\begin{aligned} |S=0, x\rangle &\equiv \frac{1}{\sqrt{2}}\sigma^x_{mm'} c^\dagger_{m\uparrow} c^\dagger_{m'\downarrow}|0\rangle, \\ |S=0, z\rangle &\equiv \frac{1}{\sqrt{2}}\sigma^z_{mm'} c^\dagger_{m\uparrow} c^\dagger_{m'\downarrow}|0\rangle \end{aligned} \tag{2.27}$$

with $E_{S=0,-} = U - J$. The last piece is $U(1)_{\text{orbital}}$ singlet

$$|S=0, +\rangle \equiv \frac{1}{\sqrt{2}}\delta_{mm'} c^\dagger_{m\uparrow} c^\dagger_{m'\downarrow}|0\rangle \tag{2.28}$$

with $E_{S=0,+} = U + J$. This indicates that, for large negative U, interband superconductivity with $S = 1$ is preferable for $J > 0$, and intraband spin singlet superconductivity is preferable for $J < 0$. The latter superconductivity is indeed the sSS phase in the negative J region. On the other hand, the positive J region does not match with the p_ySS state in the phase diagram. This discrepancy is attributed to the different numbers of allowed scattering processes; when two Fermi momenta are different, the number of interband scattering processes is fewer than that of intraband ones. Therefore, interband orderings are suppressed. For example, the following interband

process is prohibited when $k_A \neq k_B$,

$$n_{A\sigma}n_{B\bar{\sigma}} \simeq c^{\dagger}_{AL\sigma}c_{AR\sigma}c^{\dagger}_{BR\bar{\sigma}}c_{BL\bar{\sigma}} + \text{H.c.}, \tag{2.29}$$

although a similar intraband process is allowed,

$$n_{m\sigma}n_{m\bar{\sigma}} \simeq c^{\dagger}_{mL\sigma}c_{mR\sigma}c^{\dagger}_{mR\bar{\sigma}}c_{mL\bar{\sigma}} + \text{H.c.}. \tag{2.30}$$

Therefore, $|S = 0, z\rangle$ is more suitable in positive J, and this corresponds to the p_ySS state. Of course, when J becomes sufficiently strong, the energy gain by spin alignment becomes predominant, and the system exhibits spin-triplet superconductivity. Similarly, the CDW phase in upper left area for equivalent bands appears since it is strongly enhanced due to the "nesting" of $k_A = k_B$ although the p_ySS state is not affected. Here all the phases are non-degenerate, so only the total charge mode is massless, $C1S0$.

The large negative J region ($-J \gg |U|$) is again described by the $n_{A\sigma}n_{B\sigma}$ term in Eq. (2.2), and the ground state should be an interband orbital density wave, which corresponds to the SDW state of the simple Hubbard model. So the possible candidates are either the s'CDW state, or the pCDW state. Taking into account the ordering of the fermionic operators in $n_{A\sigma}n_{B\sigma}$, we find that the s'CDW state has correct sign to be the ground state. For $k_A = k_B$ case, the s'CDW and pCDW states are degenerate as the $\mathrm{U}(1)_o$ symmetry requires.

The phase diagrams for half-filling cases are shown in Fig. 2.5. At half-filling, the most of the arguments presented for the case of general filling still apply, but we have to take Umklapp processes into consideration. Since Umklapp processes enhance only density-wave states, superconducting states that appear in the negative U region are now replaced by the CDW state as in the $k_A = k_B$ case away from half-filling. An interesting new phase is the s'SDW state, which is located between the s'CDW and

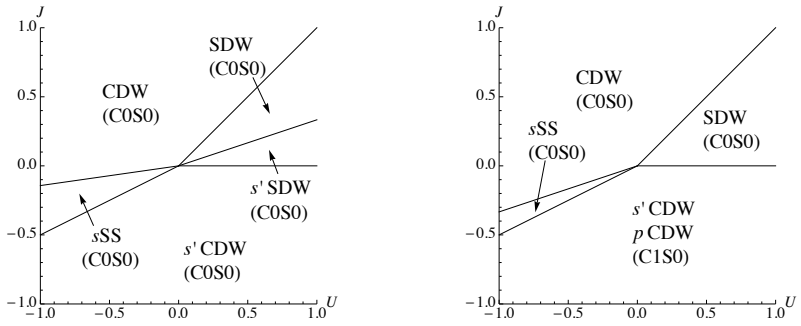

(a) $k_A \neq k_B$ (b) $k_A = k_B = \pi/2$

Figure 2.5: Mean-field phase diagrams for commensurate cases [reproduced from Okamoto and Millis (2011)].

SDW states for the $k_A \neq k_B$ case. At this special filling, interband Umklapp processes are enhanced, so the s'SDW state is dominant at small J. However, the s'SDW state is stable only when $U > J$, although the SDW state is stable for all $U, J > 0$ region. Thus at large J, the SDW state is again dominant, and we obtain the above phase diagram.

The sSS phase at half-filling should be read as the S-Mott or S'-Mott state at commensurate filling, we know that the system is insulating due to Umklapp processes. These Mott insulating states have similar order parameters as the sSS state except the total charge mode when it is written in bosonic fields, and turn into the sSS state upon doping.

Finally most of the phases appearing at half-filling are completely gapped, $C0S0$, except a region where the s'CDW and pCDW states are degenerate. In this degenerate region, the orbital sector is massless, $C1S0$.

As we pointed out in Eq. (2.20), the velocity difference suppresses interband scattering processes, and intraband orders become dominant. In our cases, the dominant

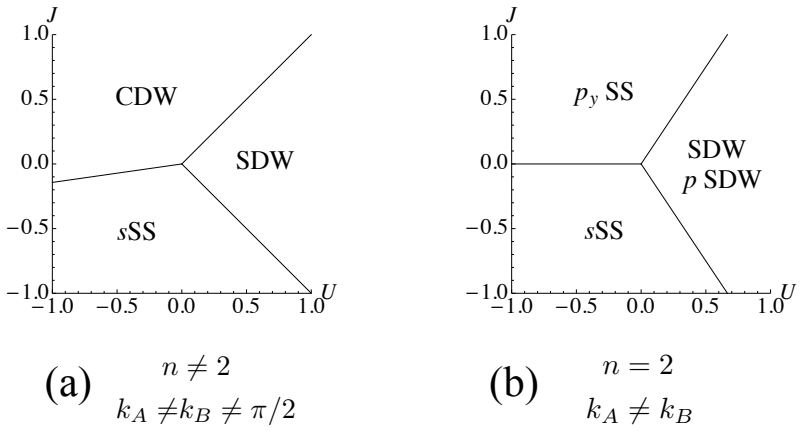

Figure 2.6: Mean-field phase diagrams with different velocities [reproduced from Okamoto and Millis (2011)].

phases appearing are p_ySS, CDW, SDW, pSDW and sSS. As the velocity difference gets larger from $v_A/v_B = 1$, the phases governed by interband scattering are gradually excluded, and beyond $v_{A(B)}/v_{B(A)} \approx 40$, which corresponds to $\nu_{\text{intra}}/\nu_{\text{inter}} \approx 10$, the whole phase diagram is covered by intraband type orderings (Fig. 2.6). The $k_A \neq k_B = \pi/2$ case looks like Fig. 2.6(a) when either v_A/v_B or v_B/v_A becomes large. When $k_A = k_B$, the phase diagrams are similar to Fig. 2.6(b) regardless of the filling.

2.5 Bosonization and renormalization group analysis

2.5.1 Bosonization

The mean-field analysis presented in the previous section captures basic physical aspects of our model, but it does not incorporate the quantum fluctuations, which may drive the system into a non-trivial fixed point different from the mean-field

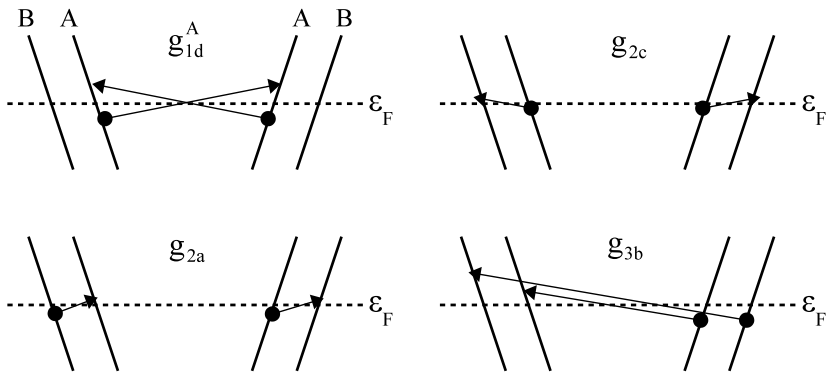

Figure 2.7: Various scattering processes and "g-ology" [reproduced from Okamoto and Millis (2012)].

results. Furthermore, we have ignored the possibility of non-local order, which are also products of purely quantum mechanical nature.

Here in order to include these ingredients, we employ bosonization and renormalization group to analyze the same model. In particular, bosonization enables us to describe the low energy physics including all the forward scattering effects. Without backscattering terms, the effective model describes the hydrodynamic phonon modes of electron densities with a renormalized velocity due to the forward scattering. We present an Abelian-bosonization analysis, which is useful for the cases when difference in velocities is negligible. The details of the Appendix A outlines the more complicated formalism needed for unequal velocities.

We briefly recall formulas from Abelian-bosonization [Voit (1995); Giamarchi (2003); Gogolin et al. (2004); Carpentier and Orignac (2006)]. The following formula gives transformation from a fermionic Hamiltonian to a bosonic Hamiltonian,

$$\psi_{m\sigma r} = \frac{\eta_{m\sigma}}{\sqrt{2\pi\alpha}} e^{\mp i\Phi_{m\sigma r}}, \tag{2.31}$$

where $m = A, B$ is orbital, $r = R, L$ is chirality, and η is a Majorana fermion or Klein factor, which takes care of the fermionic properties. The bosonic fields satisfy the

commutation relations,

$$\begin{aligned}[\Phi_{m\sigma R(L)}(x), \Phi_{m'\sigma' R(L)}(x')] &= \pm i\pi\delta_{mm'}\delta_{\sigma\sigma'}\mathrm{sgn}(x-x') \\ [\Phi_{m\sigma R}(x), \Phi_{m'\sigma' L}(x')] &= i\pi\delta_{mm'}\delta_{\sigma\sigma'}.\end{aligned} \tag{2.32}$$

The Majorana fermions obey anti-commutation relations

$$\{\eta_{m\sigma}, \eta_{m'\sigma'}\} = 2\delta_{mm'}\delta_{\sigma\sigma'}. \tag{2.33}$$

A more convenient representation is given by the non-chiral fields,

$$\phi_{m\sigma}, \theta_{m\sigma} = \frac{1}{2}(\Phi_{m\sigma L} \pm \Phi_{m\sigma R}). \tag{2.34}$$

They are connected to density and current as $\nabla\phi \propto n$ and $\nabla\theta \propto j$, and satisfy commutation relations,

$$\begin{aligned}[\phi_{m\sigma}(x), \phi_{m'\sigma'}(x')] &= [\theta_{m\sigma}(x), \theta_{m'\sigma'}(x')] = 0 \\ [\phi_{m\sigma}(x), \theta_{m'\sigma'}(x')] &= i\pi\delta_{mm'}\delta_{\sigma\sigma'}\Theta(x'-x),\end{aligned} \tag{2.35}$$

where $\Theta(x)$ is the Heaviside step function. Finally we move to different combinations of these fields,

$$\begin{bmatrix}\phi_{c0} \\ \phi_{c\pi} \\ \phi_{s0} \\ \phi_{s\pi}\end{bmatrix} = \frac{1}{2}\begin{bmatrix}1 & 1 & 1 & 1 \\ 1 & 1 & -1 & -1 \\ 1 & -1 & 1 & -1 \\ 1 & -1 & -1 & 1\end{bmatrix}\begin{bmatrix}\phi_{A\uparrow} \\ \phi_{A\downarrow} \\ \phi_{B\uparrow} \\ \phi_{B\downarrow}\end{bmatrix}, \tag{2.36}$$

where $\mu = (c, s)$ represents charge and spin modes, and $\nu = (0, \pi)$ gives bonding/antibonding basis. θ's are transformed in the same manner. The sign of each coupling constant is determined by Klein factors, and by a commutator between different chirality, $[\Phi_{R,n}(x), \Phi_{L,n'}(x')] = i\pi\delta_{n,n'}$. The eigenvalues of Klein factors composed

of two Majorana fermions (different from the ones introduced for refermionization later) are taken to be

$$i = \eta_{As}\eta_{Bs} = \eta_{A\uparrow}\eta_{A\downarrow} = \eta_{A\uparrow}\eta_{B\downarrow} = \eta_{B\uparrow}\eta_{A\downarrow} = -\eta_{B\uparrow}\eta_{B\downarrow}. \tag{2.37}$$

To classify the various scattering processes we follow the notation of Chudzinski et al. (2008). "1–4" corresponds to conventional "g-ology" indices for left and right moving fields, and "a–d" are similar but label orbital indices. Some examples are given in Fig. 2.7. Using the standard bosonization formalism,Voit (1995); Giamarchi (2003); Gogolin et al. (2004) the Hamiltonian density $\mathcal{H}_0$ of the free-boson part becomes,

$$\mathcal{H}_0 = \frac{1}{2\pi}\sum_{\substack{\mu=c,s\\ \nu=0,\pi}} v_{\mu\nu}\left[K_{\mu\nu}(\nabla\theta_{\mu\nu})^2 + \frac{1}{K_{\mu\nu}}(\nabla\phi_{\mu\nu})^2\right] \tag{2.38}$$

where ϕ and θ are connected to density and current: $\nabla\phi \propto n$, and $\nabla\theta \propto j$. The renormalized Luttinger parameters and velocities are given by

$$\begin{aligned}
K_{c0(\pi)} &= \sqrt{\frac{1-(y_{1d}\pm y_{2b})/2}{1+(y_{1d}\pm y_{2b})/2}} \equiv 1 - y_{c0(\pi)}\\
K_{s0(\pi)} &= \sqrt{\frac{1+(y_{1d}\pm y_{1a})/2}{1-(y_{1d}\pm y_{1a})/2}} \equiv 1 - y_{s0(\pi)}\\
v_{c0(\pi)} &= v\sqrt{1-(y_{1d}\pm y_{2b})^2/4}\\
v_{s0(\pi)} &= v\sqrt{1-(y_{1d}\mp y_{1a})^2/4}
\end{aligned} \tag{2.39}$$

with $y_i \equiv g_i/4\pi v$ and $y_{2b} \equiv y_{2b}^{\perp} + y_{2b}^{\parallel}$. "$c$" and "$s$" represent the charge and spin modes, and "0" and "π" are used for bonding and antibonding combination. We introduced $y_{\mu\nu}$ for each Luttinger parameter for later use. We ignore the velocity difference induced by the g_4 process, since its effect is to shift the phase boundaries slightly. We will provide a separate treatment for systems in which difference of initial velocities

is quite large.

The interaction part of the Hamiltonian is rather complicated. The interaction terms common to all cases are

$$\begin{aligned} H_{\rm int} = & \, g_{1d} \int \cos\left(2\phi_{s0}\right) \cos\left(2\phi_{s\pi}\right) \\ & + g_{1a} \int \cos\left(2\phi_{s0}\right) \cos\left(2\theta_{s\pi}\right) \\ & - g_{1c} \int \cos\left(2\phi_{s0}\right) \cos\left(2\theta_{c\pi}\right) \\ & - g_{2c} \int \cos\left(2\phi_{s\pi}\right) \cos\left(2\theta_{c\pi}\right) \\ & + g_{\|c} \int \cos\left(2\theta_{s\pi}\right) \cos\left(2\theta_{c\pi}\right). \end{aligned} \tag{2.40}$$

Here $\int$ stands for $(2\pi\alpha)^{-2} \int dx$, and α is the cut-off which is of the order of the lattice constant. The last term does not exist in the original Hamiltonian, but will be generated after the one-loop renormalization. When $k_A = k_B$, in cases (a) and (b), additional processes are allowed,

$$\begin{aligned} H'_{\rm int} = & \, g_{\|a} \int \cos\left(2\phi_{s\pi}\right) \cos\left(2\phi_{c\pi}\right) \\ & + g_{1b} \int \cos\left(2\phi_{s0}\right) \cos\left(2\phi_{c\pi}\right) \\ & + g_{2a} \int \cos\left(2\theta_{s\pi}\right) \cos\left(2\phi_{c\pi}\right). \end{aligned} \tag{2.41}$$

Finally when the filling is commensurate, we have

$$\begin{aligned} H''_{\rm int} = & \, g_{3a} \int \cos\left(2\phi_{c0}\right) \cos\left(2\theta_{s\pi}\right) \\ & - g_{3b} \int \cos\left(2\phi_{c0}\right) \cos\left(2\phi_{s\pi}\right) \\ & - g_{3c} \int \cos\left(2\phi_{c0}\right) \cos\left(2\theta_{c\pi}\right) \\ & - g_{3d} \int \cos\left(2\phi_{c0}\right) \cos\left(2\phi_{c\pi}\right) \\ & - g_{\parallel b} \int \cos\left(2\phi_{c0}\right) \cos\left(2\phi_{s0}\right). \end{aligned} \tag{2.42}$$

The g_{3d} process exists only when both bands are commensurate, case (a). Again, we ignored the g_4 type interactions whose scaling dimension is always larger than two, and this is consistent with the equal velocity approximation. The initial values of these coupling constants are: $g_{1d} = g_{3d} = 4U$, $g_{1a} = g_{1c} = g_{2c} = g_{2a} = g_{3a} = g_{3c} = 4J$, $g_{2b}^{\parallel} = g_{\parallel a} = g_{\parallel b} = 4(U-3J)$, and $g_{1b} = g_{2b}^{\perp} = g_{3b} = 4(U-2J)$. They will take different values after renormalization.

The $\mathrm{SU}(2)_s$ symmetry constrains coupling constants as

$$\begin{aligned} g_{1d}^{m} - g_{2d}^{m} &= 0, \\ g_{2b}^{\perp} - g_{2b}^{\parallel} - g_{1a} &= 0, \\ g_{1c} - g_{2c} + g_{\parallel c} &= 0, \\ g_{s0(\pi)} + \frac{1}{2}(g_{1d} \pm g_{1a}) &= 0. \end{aligned} \tag{2.43}$$

For the rest of the chapter, we will omit $\perp$ when it is not confusing. When two Fermi points coincide, we have additional processes $g_{\parallel a}$, g_{1b}, and g_{2a}, which are connected by the $\mathrm{SU}(2)_s$ symmetry as,

$$g_{\parallel a} - g_{1b} + g_{2a} = 0. \tag{2.44}$$

$k_A = k_B$ means that we have the $\mathrm{U}(1)_o$ symmetry, and this implies

$$\begin{aligned} g^A_{1(2)d} - g^B_{1(2)d} &= 0, \\ -g^m_{2d} + g^{\perp}_{2b} + g_{2c} + g_{2a} &= 0, \\ -g^m_{1d} + g_{1b} + g_{1c} + g_{1a} &= 0, \\ g^{\parallel}_{2b} + g_{\parallel c} - g_{\parallel a} &= 0, \\ g_{c\pi} + \frac{1}{2}(-g_{1d} + g_{2b}) &= 0. \end{aligned} \tag{2.45}$$

As Umklapp processes, we have $g_{\parallel b}$ and g_{3i} ($i = a$–d). The g^m_{3d} process represents the intraband Umklapp process, so it only exists for $k_m = \pi/2$. Other Umklapp processes are possible whenever $n = 2$. The $\mathrm{SU}(2)_s$ symmetry gives

$$g_{3a} + g_{\parallel b} - g_{3b} = 0, \tag{2.46}$$

and the $\mathrm{U}(1)_o$ symmetry leaves

$$g_{3d} = g_{3a} + g_{3b} + g_{3c}. \tag{2.47}$$

Contrary to the classical case in Sec. 1.3, these potentials do not immediately lead to the destruction of massless modes because of two reasons. First, the forward scattering among electrons renormalizes the velocity and Luttinger parameters. Due to these renormalization effects, the scaling dimensions of backscattering terms usually deviate from the non-interacting values at the first order of RG equations; some coupling constants may be irrelevant. Furthermore, when we consider the second order effects in RG equations, the complicated coupling among various scattering channels further change the fixed points from the ones obtained from simple scaling arguments. Thus, in general, we need to integrate the RG equations to figure out the final fixed points; the final Hamiltonian can be totally different from the initial one.

Finally we will discuss the symmetry of the linearized model (Table 2.1). First, $U(1)_c$ and $SU(2)_s$ (around z-axis) are displayed in the invariance of the Hamiltonian under the translation of θ_{c0} and θ_{s0}. In fermionic language, each corresponds to the following gauge transformation:

$$c_{rms} \to e^{i\alpha} c_{rms}, \quad c_{rms} \to e^{is\alpha} c_{rms}. \tag{2.48}$$

The indices r, m, and s represent chirality, orbital, and spin, and α expresses the constant phase shift. The conserved Noether currents, corresponding to the $U(1)_c$ and $SU(2)_s$ symmetries are,

$$\begin{aligned} \sum_{rms} N_{rms} &\propto \int dx \nabla \phi_{c0}, \\ \sum_{rms} s N_{rms} &\propto \int dx \nabla \phi_{s0}, \end{aligned} \tag{2.49}$$

where N_{rms} is the particle number at the branch specified by r, m, and s. Since $\nabla\phi$ is momentum conjugate of θ, the operator $\exp\left(\int dx \nabla\phi\right)$ gives a constant shift of θ. The $SU(2)_s$ rotation around x- and y-axis are not manifest in Abelian bosonization.

Away from half filling, there is also a continuous chiral symmetry under the transformation, $c_{rms} \to e^{ir\alpha} c_{rms}$. Thus, the Hamiltonian is invariant under arbitrary translation of ϕ_{c0}, with conserved total currents, $J_A + J_B \propto \int dx \nabla\theta_{c0}$ where $J_m = \sum_s N_{Rms} - N_{Lms}$. At half filling, this symmetry is broken to a discrete symmetry, and true long-range order can be realized.Wu et al. (2003) When a system has both the chiral symmetry and the $U(1)_c$ symmetry, this implies that left, and right moving parts have separate conservation laws corresponding to the $U(1)_R \times U(1)_L$

symmetry. Similarly, other gauge transformations such as

$$\begin{aligned} c_{rms} &\to e^{im\alpha} c_{rms}, \\ c_{rms} &\to e^{ims\alpha} c_{rms}, \\ c_{rms} &\to e^{irs\alpha} c_{rms}, \\ c_{rms} &\to e^{irms\alpha} c_{rms}, \end{aligned} \tag{2.50}$$

leave the Hamiltonian invariant for discrete values of $\alpha = n\pi/2$; each corresponds to the discrete shift of $\theta_{c\pi}$, $\theta_{s\pi}$, ϕ_{s0}, and $\phi_{s\pi}$. When $k_A = k_B$, there is an explicit orbital rotational symmetry about y-axis. This transformation mixes fermions in different orbitals, so its generator cannot be expressed as a local operator in Abelian bosonization. This fact leads to a new combination of possible ground states as will be shown.

The effective $\widetilde{\mathrm{U}(1)}_o$ symmetry appearing when $k_A \neq k_B$ and $v_A = v_B$,Lin et al. (1998); Controzzi and Tsvelik (2005); Boulat et al. (2009); Nonne et al. (2010) corresponds to the invariance under the translation of $\phi_{c\pi}$ or the gauge transformation,

$$c_{rms} \to e^{irm\alpha} c_{rms}. \tag{2.51}$$

The conserved "charge" corresponding to this symmetry is the difference of two orbital currents: $J_A - J_B \propto \int dx \nabla \theta_{c\pi}$.

2.5.2 Renormalization group

The idea of renormalization was first introduced in particle physics [Peskin and Schroeder (1995)], and later K. Wilson developed a renormalization group (RG) [Wilson (1975)]. The basic spirit of RG is deriving a low-energy Hamiltonian by successively integrating out the higher energy degrees of freedom. RG equations describe

the flow of coupling constants as the ultraviolet cut-off Λ changes from the original one Λ_0.

In the RG equations obtained from Abelian bosonization, we use normalized coupling constants defined as

$$y_i \equiv \frac{g_i}{4\pi v}. \tag{2.52}$$

RG equations are derived using the operator product expansion (OPE) [Cardy (1996); Balents and Fisher (1996); Delft and Schoeller (1998)] and integrating out higher frequency modes. The RG equations are complicated, so we will not show them explicitly. In all of the cases that we have examined, the RG equations may be expressed as

$$\frac{dy_i}{dl} = -\frac{\partial V}{\partial y_i}. \tag{2.53}$$

with a potential function, $V[y_1(l), y_2(l), \cdots, y_n(l)]$, and the flow parameter $l = \ln \Lambda_0/\Lambda$. The RG flow is to the valleys of the potential in the beginning and then along the valley. The potential structure is consistent with the arguments of Chen et al. (2004). For the commensurate case, $k_A = k_B = \pi/2$, the potential is

$$\begin{aligned} V[y_i] = & -y_{1a}y_{1c}y_{\parallel c} + y_{1a}y_{1b}y_{2a} - y_{1a}y_{3a}y_{\parallel b} + y_{1c}y_{1d}y_{2c} - y_{1c}y_{3c}y_{\parallel b} + y_{1d}y_{\parallel a}y_{1b} \\ & + y_{1d}y_{3b}y_{\parallel b} - y_{2c}y_{3b}y_{3c} - y_{\parallel c}y_{3a}y_{3c} + y_{1b}y_{3d}y_{\parallel b} - y_{2a}y_{3a}y_{3d} + y_{\parallel a}y_{3b}y_{3d} \\ & - \frac{1}{2}\left(y_{3a}^2 - y_{3b}^2 - y_{3c}^2 - y_{3d}^2 - y_{\parallel b}^2\right) y_{c0} \\ & - \frac{1}{2}\left(-y_{1c}^2 - y_{2c}^2 - y_{\parallel c}^2 + y_{\parallel a}^2 + y_{1b}^2 + y_{2a}^2 - y_{3c}^2 + y_{3d}^2\right) y_{c\pi} \\ & - \frac{1}{2}\left(y_{1d}^2 + y_{1a}^2 + y_{1c}^2 + y_{1b}^2 + y_{\parallel b}^2\right) y_{s0} \\ & - \frac{1}{2}\left(y_{1d}^2 - y_{1a}^2 + y_{2c}^2 - y_{\parallel c}^2 + y_{\parallel a}^2 - y_{2a}^2 - y_{3a}^2 + y_{3b}^2\right) y_{s\pi}, \end{aligned} \tag{2.54}$$

where we introduced $K_{\mu\nu} \equiv 1 - y_{\mu\nu}$ for each Luttinger parameter. For $k_A \neq k_B$ or doped cases, we should remove some coupling constants which are not allowed by momentum conservation. The RG equations valid even when velocities are different

are given in Appendix A. We checked that both RG equations give consistent results when $v_A = v_B$.

To get phase diagrams, we integrate the RG equations numerically until one of the coupling constant becomes of the order of $1(\equiv t)$. We used initial values of coupling constants as small as 10^{-8}–10^{-3}. Due to the hidden potential structure, the asymptotic behavior of the RG flow is captured by the following ansatz [Balents and Fisher (1996); Chen et al. (2004)],

$$g_i'[l] = \frac{g_{0i}}{l_c - l}, \tag{2.55}$$

where l_c is the length at which the relevant couplings diverge, and the g_{0i} determines the ratio among them. This represents the fixed ray of relevant coupling constants. Then, the bosonic fields are pinned down to the minima of the effective potential. These values enable us to determine the order parameter that takes a non-zero value.

2.5.3 Order parameters

The relevant local order parameters for RG study are only the spin-singlet part $j = 0$, and their bosonized forms are:

$$\begin{aligned}
\mathcal{O}^{00}_{\rm ph} &\propto \cos\left(k_0 x - \phi_{c0}\right) \sin\left(k_\pi x - \phi_{c\pi}\right) \sin\left(\phi_{s0}\right) \sin\left(\phi_{s\pi}\right), \\
\mathcal{O}^{10}_{\rm ph} &\propto \cos\left(k_0 x - \phi_{c0}\right) \sin\left(\theta_{c\pi}\right) \cos\left(\phi_{s0}\right) \cos\left(\theta_{s\pi}\right), \\
\mathcal{O}^{20}_{\rm ph} &\propto \cos\left(k_0 x - \phi_{c0}\right) \cos\left(\theta_{c\pi}\right) \cos\left(\phi_{s0}\right) \cos\left(\theta_{s\pi}\right), \\
\mathcal{O}^{30}_{\rm ph} &\propto \cos\left(k_0 x - \phi_{c0}\right) \sin\left(k_\pi x - \phi_{c\pi}\right) \cos\left(\phi_{s0}\right) \cos\left(\phi_{s\pi}\right), \\
\mathcal{O}^{00}_{\rm pp} &\propto e^{-i\theta_{c0}} \sin\left(k_\pi x - \phi_{c\pi}\right) \cos\left(\phi_{s0}\right) \cos\left(\theta_{s\pi}\right), \\
\mathcal{O}^{10}_{\rm pp} &\propto e^{-i\theta_{c0}} \sin\left(\theta_{c\pi}\right) \sin\left(\phi_{s0}\right) \sin\left(\phi_{s\pi}\right), \\
\mathcal{O}^{20}_{\rm pp} &\propto e^{-i\theta_{c0}} \cos\left(\theta_{c\pi}\right) \sin\left(\phi_{s0}\right) \sin\left(\phi_{s\pi}\right), \\
\mathcal{O}^{30}_{\rm pp} &\propto e^{-i\theta_{c0}} \sin\left(k_\pi x - \phi_{c\pi}\right) \sin\left(\phi_{s0}\right) \sin\left(\theta_{s\pi}\right),
\end{aligned} \tag{2.56}$$

with $k_{0(\pi)} = k_A \pm k_B$. If coupling constants grow to the order of t after renormalization, the corresponding bosonic fields are pinned to the values that minimize the resultant potential. For incommensurate fillings, the total charge mode is massless, and the interaction terms pin the other modes to definite values (in mod of π). The pinned values determine the order parameter that gives a finite value of correlation. It is easy to find such pinned values from the above expressions, e.g., $(\theta_{c\pi}, \phi_{s0}, \phi_{s\pi}) = (\pi/2, 0, 0)$ for the s'CDW state.

When a filling is commensurate, insulating phases (with the gapped total charge mode) become possible, and it turns out that the generic behavior is either that all fields are massless or all fields are gapped. We discuss the fully gapped phases here. In the bosonized representation, the physics is described by the conjugate fields, $\phi_{\mu\nu}$ and $\theta_{\mu\nu}$, in the four sectors, $\mu = c, s$, and $\nu = 0, \pi$. In a fully gapped situation, in each sector, one of $\phi_{\mu\nu}$ or $\theta_{\mu\nu}$ is pinned at a value that may be 0 or $\pi/2$ (mod π); the conjugate variable fluctuates strongly. Naively this implies $(2 \times 2)^4 = 256$ possible

Phase	$\langle\phi_{c\pi}\rangle$	$\langle\theta_{c\pi}\rangle$	$\langle\phi_{s0}\rangle$	$\langle\phi_{s\pi}\rangle$	$\langle\theta_{s\pi}\rangle$
CDW	$\pi/2$		$\pi/2$	$\pi/2$	
BDW(SP)	0		0	0	
s'CDW(CDW$_\pi$)		$\pi/2$	0		0
s'BDW(PDW)		0	$\pi/2$		$\pi/2$
p'CDW(SF)		0	0		0
p'BDW (FDW)		$\pi/2$	$\pi/2$		$\pi/2$
pCDW(ODW)	$\pi/2$		0	0	
pBDW(SP$_\pi$)	0		$\pi/2$	$\pi/2$	
HC	$\pi/2$		$\pi/2$		$\pi/2$
RS	0		0		0
S-Mott		$\pi/2$	0	0	
S'-Mott		0	$\pi/2$	$\pi/2$	
D-Mott		0	0	0	
D'-Mott		$\pi/2$	$\pi/2$	$\pi/2$	
HO	$\pi/2$		0		0
RT	0		$\pi/2$		$\pi/2$

Table 2.4: Expectation values of bosonic variables in the fully gapped phases. We set $\langle\phi_{c0}\rangle = 0$. The commonly used names are given in parentheses. SP: spin-Peierls, SF: staggered flux, PDW: p-wave density wave, FDW: f-wave density wave.

insulating states, but only a few of these are relevant. The charge conservation implies that only ϕ_{c0} can be pinned, and the gauge invariance under translating all angles by $\pi/2$ allows us to set $\langle\phi_{c0}\rangle = 0$. The spin conservation means that only ϕ_{s0} can be pinned and additional constraints arising from the structure of the interactions may further limit the possibilities. In the end, only eight density-wave states and the corresponding eight dual Mott insulating states are relevant. The Mott states are obtained from the density-wave states by interchanging which of $\phi_{s\pi}$ and $\theta_{s\pi}$ is pinned, and The pinned values of bosonic variables in the sixteen insulating phases are given in Table 2.4.

The density-wave states have a straightforward description in terms of local order parameters defined as local combinations of fermion bilinears. The transcription is

given in the previous subsection, and will not be elaborated on here with one proviso: the gap in the total charge mode implies a breaking of translational invariance, corresponding to a U(1) invariance in boson language. Therefore, only a $\mathcal{Z}_2$ invariance (shift of ϕ_{c0} by $\pi/2$) remains, and this allows us to distinguish site-centered states (CDW's), and bond-centered states (BDW's).

Dual to the density-wave stats are the Mott insulating states. These evolve into superconducting states upon doping. We do not know a general representation in terms of bilinears constructed from the original fermion operators, even if non-local string states are allowed. In some cases, approximate wave functions can be written down in the strong coupling limit, essentially by analogy to the superconducting states that appear upon doping [Lin et al. (1998); Tsuchiizu and Furusaki (2002b); Momoi and Hikihara (2003)]:

$$\begin{aligned}
|S\text{-Mott}\rangle &\equiv \prod_i \left[c^\dagger_{iA\uparrow}c^\dagger_{iA\downarrow} + c^\dagger_{iB\uparrow}c^\dagger_{iB\downarrow}\right]|0\rangle\,, \\
|D\text{-Mott}\rangle &\equiv \prod_i \left[c^\dagger_{iA\uparrow}c^\dagger_{iA\downarrow} - c^\dagger_{iB\uparrow}c^\dagger_{iB\downarrow}\right]|0\rangle\,, \\
|\text{RS}\rangle &\equiv \prod_i \left[c^\dagger_{iA\uparrow}c^\dagger_{iB\downarrow} - c^\dagger_{iA\downarrow}c^\dagger_{iB\uparrow}\right]|0\rangle\,, \\
|\text{RT}\rangle &\equiv \frac{1}{2}\prod_i \left[c^\dagger_{iA\uparrow}c^\dagger_{i+1,B\downarrow} - c^\dagger_{iA\downarrow}c^\dagger_{i+1,B\uparrow} - (A \leftrightarrow B)\right]|0\rangle\,,
\end{aligned} \tag{2.57}$$

where RS stands for the rung-singlet state, and RT for the rung-triplet state [Nishiyama et al. (1995); Kim et al. (2000)]. These four states evolve into the sSS, pSS, s'SS, and d'SS states upon doping respectively. The bonding counterparts of these phases are the S'-Mott, D'-Mott, Haldane-charge (HC), and Haldane-orbital (HO) phases [Nonne et al. (2010)]. However, finding wave functions for these four Mott states remains a challenge.

Also, in some particular cases, string operators can be constructed. For example, in the strong-coupling limit, where the charge mode is decoupled, we expect the

RS and RT states become the ones that appear in spin-$\frac{1}{2}$ Heisenberg two-leg ladders [Nishiyama et al. (1995); Kim et al. (2000)]. The RS state appears in chains with antiferromagnetic coupling along rung (or ferromagnetic coupling over plaquette diagonals), and it is a resonance-valence-bond (RVB) state whose stable configurations are the singlet along rung or ladder. This state is characterized by a non-zero expectation value of a string operator

$$\langle \left(S^z_{A,i} + S^z_{B,i+1}\right) e^{i\pi \sum_{k=i+1}^{j-1} \left(S^z_{A,k} + S^z_{B,k+1}\right)} \left(S^z_{A,j} + S^z_{B,j+1}\right) \rangle, \tag{2.58}$$

and exhibits a "hidden antiferromagnetic order"; the total spin over plaquette diagonals, $S^z_{A,i} + S^z_{B,i+1}$, align antiferromagnetically along ladder except spin-0 site. For chains coupled ferromagnetically along rung (or antiferromagnetically over plaquette diagonals), the above order disappears, and the RT state with the Valence-Bond-Solid (VBS) configuration [Affleck et al. (1987)] becomes stable. Singlet pairs are formed in a staggered manner, and this results in triplet pair along a rung. The following order parameter takes a non-vanishing value,

$$\langle \left(S^z_{A,i} + S^z_{B,i}\right) e^{i\pi \sum_{k=i+1}^{j-1} \left(S^z_{A,k} + S^z_{B,k}\right)} \left(S^z_{A,j} + S^z_{B,j}\right) \rangle, \tag{2.59}$$

which represents a hidden order about the spin-triplet on a rung. The string operators for these disordered states are non-local, so complications arise in the transcription to bosonic variables. Generally accepted forms for Eqs. (2.58) and (2.59) are [Nakamura (2003)]:

$$\begin{aligned} &\langle \cos\left[\phi_{s0}(x)\right] \cos\left[\phi_{s0}(y)\right] \rangle, \\ &\langle \sin\left[\phi_{s0}(x)\right] \sin\left[\phi_{s0}(y)\right] \rangle. \end{aligned} \tag{2.60}$$

These correlation functions take non-zero values for the RS and RT phases respectively.

The bonding counterparts of the RS and RT phases are the Haldane-charge (HC), and Haldane-orbital (HO) phases proposed by Nonne et al. (2010) as the Haldane gapped states of pseudo spin-1 antiferromagnetic Heisenberg chain; this realizes when the charge or orbital symmetry is promoted from U(1) to SU(2). The form of string operators for these states is similar to Eq. (2.59) if we replace the SU(2) spin operators by the charge and orbital SU(2) operators:

$$J_i^z = \frac{1}{2}(n_i - 2), \;\; J_i^\dagger = c_{i,A\uparrow}^\dagger c_{i,B\downarrow}^\dagger - c_{i,A\downarrow}^\dagger c_{i,B\uparrow}^\dagger; \tag{2.61}$$

$$T_i^z = \frac{1}{2}(n_{A,i} - n_{B,i}), \;\; T_i^\dagger = c_{i,A\uparrow}^\dagger c_{i,B\uparrow} + c_{i,A\downarrow}^\dagger c_{i,B\downarrow}. \tag{2.62}$$

The bosonized form of the strong operators are

$$\begin{aligned} \langle J_i^z e^{i\pi \sum_{k=i+1}^{j-1} J_k^z} J_j^z \rangle &\sim \langle \sin(\phi_{c0}(x)) \sin(\phi_{c0}(y)) \rangle, \\ \langle T_i^z e^{i\pi \sum_{k=i+1}^{j-1} T_k^z} T_j^z \rangle &\sim \langle \sin(\phi_{c\pi}(x)) \sin(\phi_{c\pi}(y)) \rangle, \end{aligned} \tag{2.63}$$

where $\nabla\phi_{c0} \sim J^z(x)$ and $\nabla\phi_{c\pi} \sim T^z(x)$. These expressions become non-zero for the HC and HO phases respectively.

2.5.4 Quantum phase transitions

Two of the most prominent features of one-dimensional systems are *dynamical symmetry enlargement (DSE)* [Lin et al. (1998); Konik et al. (2002)] and *duality* [Momoi and Hikihara (2003); Boulat et al. (2009); Nonne et al. (2010)]. Employing these two ideas enables us to narrow down the possible phases appearing in the phase diagram; without these and other symmetry considerations, there are 256 possible phases.

DSE means that the effective theory describing the low energy fixed point exhibits a higher symmetry than that of the original lattice Hamiltonian. This phenomenon

was noted by Lin et al. (1998), who found that the low-energy theory of half-filled two-leg Hubbard ladder is the SO(8) Gross-Neveu (GN) model. Since their work, DSE to O(8) or O(6) GN models has been seen in other multiband systems [Assaraf et al. (2004); Bunder and Lin (2007)]. As we will see, our model also exhibits DSE for equal velocities.

The ground states of different low-energy O(8) or O(6) GN models are related to each other by duality mappings, which are generalizations of the Kramers-Wannier duality seen in the two dimensional Ising model [Kramers and Wannier (1941)]. The idea of duality is based on the observation that the low energy theory is invariant under some discrete operations apart from the continuous symmetries listed in Table 2.1. These discrete symmetries enable us to understand quantum phase transitions among them.

Now, as a preparation, in order to exhibit the symmetries of the Hamiltonian, we refermionize the model using eight Majorana fermions as explained in Shelton et al. (1996) and Tsvelik (2011). We introduce four refermionized fields ($\lambda = c0,\ c\pi,\ s0$, or $s\pi$.),

$$\psi_{\lambda r} = \frac{\eta_\lambda}{\sqrt{2\pi\alpha}} e^{-ir\phi_\lambda + i\theta_\lambda}. \tag{2.64}$$

They satisfy the following identities:

$$\psi^\dagger_{\lambda R}\psi_{\lambda L} - \psi^\dagger_{\lambda L}\psi_{\lambda R} = \frac{-i}{\pi\alpha}\cos(2\phi_\lambda), \quad \psi^\dagger_{\lambda R}\psi^\dagger_{\lambda L} - \psi_{\lambda L}\psi_{\lambda R} = \frac{i}{\pi\alpha}\cos(2\theta_\lambda). \tag{2.65}$$

We decompose each mode into two Majorana fermions as

$$\begin{aligned} \psi^{c0}_r &= \frac{1}{\sqrt{2}}\left(\xi^7_r + i\xi^8_r\right), \quad \psi^{c\pi}_r = \frac{1}{\sqrt{2}}\left(\xi^5_r + i\xi^6_r\right), \\ \psi^{s0}_r &= \frac{1}{\sqrt{2}}\left(\xi^1_r + i\xi^2_r\right), \quad \psi^{s\pi}_r = \frac{1}{\sqrt{2}}\left(\xi^4_r + i\xi^3_r\right). \end{aligned} \tag{2.66}$$

Thus, the above identities can be rewritten for $\psi_{\lambda r} = \left(\xi_r^a + i\xi_r^b\right)/\sqrt{2}$ as

$$\xi_R^a\xi_L^a + \xi_R^b\xi_L^b = \frac{-i}{\pi\alpha}\cos(2\phi_\lambda), \quad \xi_R^a\xi_L^a - \xi_R^b\xi_L^b = \frac{i}{\pi\alpha}\cos(2\theta_\lambda). \tag{2.67}$$

Also, using the following identity (: : indicates the normal ordering),

$$:\psi_{\lambda r}^\dagger\psi_{\lambda r}: = -\frac{1}{2\pi}(\nabla\phi_\lambda - r\nabla\theta_\lambda) = -\frac{1}{2\pi}\nabla\Phi_{\lambda r}, \tag{2.68}$$

the forward scattering terms can be written as

$$\frac{1}{2}g_\lambda\int dx\xi_R^a\xi_L^a\xi_R^b\xi_L^b. \tag{2.69}$$

After substituting the these formula to the bosonized Hamiltonian, it is easy to find that at half filling, the expression for the $\mathrm{U}(1)_o$ symmetric case, (a), is,

$$\begin{aligned}\mathcal{H} = -i\frac{v}{2\pi}\sum_{a=1}^{8}(\xi_R^a\partial\xi_R^a - \xi_L^a\partial\xi_L^a) + \frac{g_1}{2}\kappa_s^2 + g_2\kappa_s\kappa_o + g_3\kappa_s\kappa_I \\ + g_4\kappa_o\kappa_I + \frac{g_5}{2}\kappa_o^2 + \frac{g_6}{2}\kappa_c^2 + g_7\kappa_s\kappa_c + g_8\kappa_o\kappa_c + g_9\kappa_I\kappa_c\end{aligned} \tag{2.70}$$

with $\kappa_s = \sum_{a=1}^{3}\xi_R^a\xi_L^a$, $\kappa_o = \sum_{a=4}^{5}\xi_R^a\xi_L^a$, $\kappa_I = \xi_R^6\xi_L^6$, and $\kappa_c = \sum_{a=7}^{8}\xi_R^a\xi_L^a$. The indices "$s$", "$o$", "$I$", and "$c$" refer to the $\mathrm{SU}(2)_s$, $\mathrm{U}(1)_o$, $\mathcal{Z}_2$, and $\mathrm{U}(1)_c$ symmetries respectively.[3]

Away from half filling, case (b), the charge mode is decoupled from the other modes, and we do not need to consider $g_{i=6\sim9}$. Thus, we have

$$\mathcal{H} = -i\frac{v}{2\pi}\sum_{a=1}^{6}(\xi_R^a\partial\xi_R^a - \xi_L^a\partial\xi_L^a) + \frac{g_1}{2}\kappa_s^2 + g_2\kappa_s\kappa_o + g_3\kappa_s\kappa_I + g_4\kappa_o\kappa_I + \frac{g_5}{2}\kappa_o^2 \tag{2.71}$$

[3] The initial values of each coupling constant are: $g_1 = -(2g_{1a} + g_{1b} + g_{1c})/4$, $g_{2,3} = \mp(g_{1c} \pm g_{1b})/4$, $g_{4,5} = (-g_{1b} \mp g_{1c} + 2g_{2a} \pm 2g_{1c})/4$, $g_6 = g_{c0}/2$, $g_{7,8} = (\mp g_{3a} + g_{3b})/4$, $g_9 = (g_{3a} + g_{3b} + 2g_{3c})/4$.

As we mentioned before, even without an explicit U(1) orbital symmetry for the lattice Hamiltonian, the low energy theory may have the effective $\widetilde{\mathrm{U}(1)}_o$ symmetry [Lin et al. (1998); Controzzi and Tsvelik (2005); Nonne et al. (2010)]. In that case, the structure of the refermionized forms is the same as above. Thus, cases (c) and (d) have the same form as Eqs. (2.70) and (2.71) with different values of g's.[4] [5]

For the refermionized forms, duality mappings are defined as, $\xi_L^a \to -\xi_L^a$ while keeping right-moving parts untouched. It is easy to see that Eqs. (2.70) and (2.71) are invariant under such transformations if we change the signs of some coupling constants as well. To retain the form of the Hamiltonian, only mappings that transform all the Majorana fields in the same symmetry sector are permitted. For example, for the SU(2) spin part, we should map the three left Majorana fermions, $\xi_L^{a=1\sim3}$, at the same time. For notational convenience, we define Ω_ν as an operation of $\xi_L^a \to -\xi_L^a$ for all the a's in a symmetry sector ν. With this at hand, it is obvious that allowed mappings for half filling cases are

$$\Omega_{O(8)} \equiv \{\Omega_c, \Omega_o, \Omega_I, \Omega_s, \Omega_{c,o}, \Omega_{c,I}, \Omega_{o,I}\}. \tag{2.72}$$

The number of independent mappings is three, and other mappings just follow from them ,e.g., $\Omega_{o,I} = \Omega_o\Omega_I$. Away from half filling, the charge mode is separated, so only three of the above mappings are left,

$$\Omega_{O(6)} \equiv \{\Omega_o, \Omega_I, \Omega_s\}, \tag{2.73}$$

and two of them are independent. An immediate consequence of these dualities and DSE is that although we showed sixteen insulating phases for half filling systems, and

[4] To get the same form, we have to redefine $\psi_L^{c\pi} = \frac{1}{\sqrt{2}}\left(\xi_L^5 - i\xi_L^6\right)$. Here the modes correspond to the new orbital part are ξ_5 and ξ_6, and the Ising mode is carried by ξ_4.

[5] The bare values of coupling constants are: $g_{1,3} = \mp(g_{1a} \pm g_{1d})/4$, $g_2 = -g_{1c}/4$, $g_4 = (g_{1c} - 2g_{2c})/4$, $g_5 = -g_{c\pi}/2$, $g_6 = g_{c0}/2$, $g_{7,9} = (\mp g_{3a} + g_{3b})/4$, $g_8 = -g_{3c}/4$

eight metallic phases for incommensurate filling, only a part of them are realized.

Now, we will show such possible ground states for each model. We start from the "fundamental" SO(8) Gross-Neveu (GN) model,

$$\mathcal{H} = -i\frac{v}{2\pi}\left(\vec{\xi}_R\partial\vec{\xi}_R - \vec{\xi}_L\partial\vec{\xi}_L\right) + \frac{g}{2}\left(\vec{\xi}_R\vec{\xi}_L\right)^2, \tag{2.74}$$

which appears at low-energy when all the g's in Eq. (2.70) converge to the same value as a result of DSE. For case (a), this model represents the BDW phase, and other possible phases are found by applying $\Omega_{O(8)}$ to the BDW state (see Table 2.5). We denote them as Γ_y, and they are

$$\Gamma_y : \text{BDW, CDW, } p'\text{CDW, } p'\text{BDW, } S\text{-Mott, } S'\text{-Mott, RT, HO.} \tag{2.75}$$

The case (b) follows from the relation between insulating states and metallic states, or applying $\Omega_{O(6)}$ to the CDW phase, which is "fundamental". The original lattice model we are considering here is invariant under the orbital U(1) rotation about y-axis. As we mentioned previously, a single local bosonic field within Abelian-bosonization scheme cannot express the generator of this symmetry .

This combination, Γ_y, is different from the ones that have been studied extensively; previously studied phases are

$$\Gamma_z : \text{BDW, CDW, } p\text{BDW, } p\text{CDW, RS, HC, RT, HO} \tag{2.76}$$

and

$$\widetilde{\Gamma_z} : S\text{-Mott, } S'\text{-Mott, } D\text{-Mott, } D'\text{-Mott, } s'\text{CDW, } s'\text{BDW, } p'\text{BDW, } p'\text{CDW.} \tag{2.77}$$

The former, Γ_z, appears in models with weak transverse hopping, and with the $\mathrm{U}(1)_o$ symmetry about z-axis [Lee et al. (2004); Nonne et al. (2010)]. The latter, $\widetilde{\Gamma_z}$, appears

	1	Ω_c	Ω_o	$\Omega_{c,o}$	Ω_I	$\Omega_{c,I}$	Ω_s	$\Omega_{c,s}$
(a)	BDW	CDW	p'CDW	p'BDW	S-Mott	S'-Mott	RT	HO
(b)	CDW	CDW	p'CDW	p'CDW	sSS	sSS	d'SS	d'SS
(c)	S-Mott	S'-Mott	D-Mott	D'-Mott	s'CDW	s'BDW	p'BDW	p'CDW
(d)	sSS	sSS	pSS	pSS	s'CDW	s'CDW	p'CDW	p'CDW

Table 2.5: Possible ground states for case (a)–(d) in Table 2.1 at equal velocities. The BDW, CDW, S-Mott, and sSS phases in the second column are expressed by the fundamental SO(8) or SO(6) Gross-Neveu model for case (a)–(d) respectively. The other states are mapped from these fundamental states by the duality transformation Ω in the top row. Ω_ν is an operation of $\xi^a_L \to -\xi^a_L$ for all the a's in a symmetry sector ν. For example, in case (a), the BDW state is mapped to the p'CDW state by Ω_o. For doped cases, (b) and (d), the charge mode is separated from the rest, and the ground states are invariant under Ω_c.

when the model has strong transverse hopping, and the low energy theory possesses the $\widetilde{\mathrm{U}(1)}_o$ symmetry [Balents and Fisher (1996); Lin et al. (1998); Tsuchiizu and Furusaki (2002b); Wu et al. (2003); Chudzinski et al. (2008)]; our cases (c) and (d) belong to this category (see Table 2.5).

The connection between Γ_y and Γ_z is obvious. Since the generator of the orbital symmetry for each case is y- or z-component of Eq. (2.62), they are simply mapped to each other by a rotation around x-axis:

$$R_x : \begin{pmatrix} c'_{rAs} \\ c'_{rBs} \end{pmatrix} = \frac{1}{\sqrt{2}} \begin{pmatrix} 1 & -i \\ -i & 1 \end{pmatrix} \begin{pmatrix} c_{rAs} \\ c_{rBs} \end{pmatrix}. \tag{2.78}$$

This transformation does not affect the charge and spin generators. For instance, the S'-Mott state in Γ_y goes to the HC state in Γ_z by R_x. The correspondence among other states is given in Fig. 2.8. On the other hand, $\widetilde{\Gamma_z}$ and Γ_z transform each other by so-called *strong-weak tunneling duality* [Controzzi and Tsvelik (2005); Nonne et al. (2010)].

$$\Omega_\perp : \quad c_{Lm\uparrow} \to c^\dagger_{Lm\downarrow}, \quad c_{Lm\downarrow} \to -c^\dagger_{Lm\uparrow}. \tag{2.79}$$

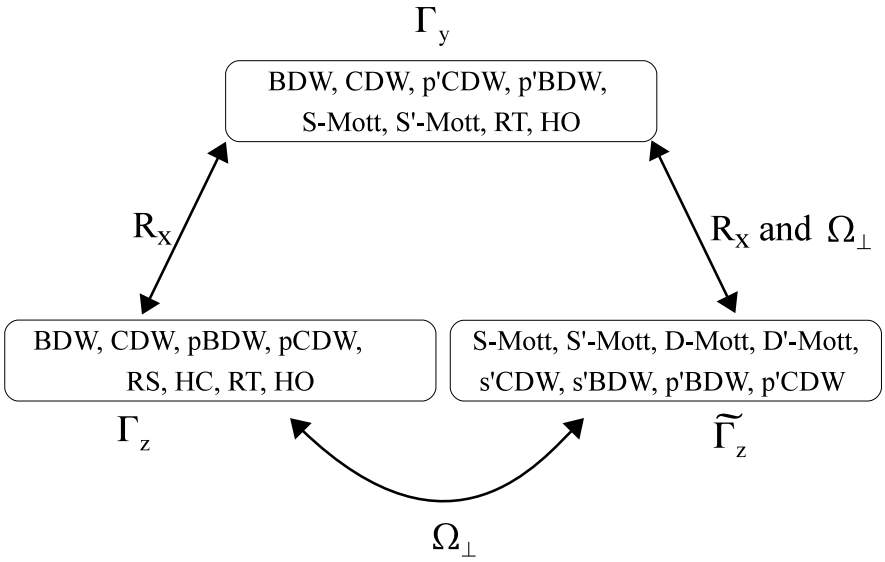

Figure 2.8: Relationships among three groups of insulating ground states [reproduced from Okamoto and Millis (2012)]. R_x indicates the rotation about x-axis in orbital space in Eq. (2.78), and $\Omega_\perp$ is strong-weak tunneling duality mapping in Eq. (2.79). For example, the S'-Mott state in Γ_y maps to the HC state in Γ_z by R_x.

Therefore, we found that in addition to underlying band structure, the form of interaction also affects the possible combinations of ground states. We summarized these results in Table 2.5 and Fig. 2.8.

The quantum phase transitions among gapped ground states could be either first order or second order. For the transitions among states connected by a duality mapping, the modes which are not involved in the mapping become massive at higher energy, and the effective low energy theory near the transition contains only Majorana fields flipped by the mapping [Boulat et al. (2009)].

For a single Majorana field, it becomes the critical Ising model,

$$\mathcal{H} = -i\frac{v}{2\pi}\left(\xi_R\partial\xi_R - \xi_L\partial\xi_L\right) - im\xi_R\xi_L \tag{2.80}$$

Over the transition, the mass changes its sign, and this represents a second-order phase transition. With more than one field, the low-energy effective theory becomes the massive O(N) Gross-Neveu (GN) model,

$$\mathcal{H} = -i\frac{v}{2\pi}\left(\vec{\xi}_R\partial\vec{\xi}_R - \vec{\xi}_L\partial\vec{\xi}_L\right) - im\vec{\xi}_R\vec{\xi}_L + \frac{g}{2}\left(\vec{\xi}_R\vec{\xi}_L\right)^2. \tag{2.81}$$

The fate of further renormalization to lower energy determines whether the phase transition is first-order or second-order depending on the final fixed point for the critical fields [Gross and Neveu (1974); Shankar (1985); Lin et al. (1998); Tsuchiizu and Furusaki (2002b); Controzzi and Tsvelik (2005)]. The transition line is defined as the point where the m in Eq. (2.81) goes to zero, and the critical fields are expressed by a massless GN model in the vicinity of transition. For $N = 2$, it is known that the system can be mapped to a Gaussian model, so it is a second order transition. For $N \geq 3$, however, if the coupling constant in the GN model is positive ($g > 0$), the renormalization flow departs to a strong coupling fixed point (asymptotic free), since the RG equation is given by

$$\dot{g} \propto g^2. \tag{2.82}$$

At this fixed point, the mass is generated dynamically, and the system is off-critical. We can see this either by mean-field treatment of the interaction (reducing the quartic part to quadratic with the order parameter $\langle\xi_R\xi_L\rangle$), or by stationary phase approximation, which becomes exact when $N \to \infty$. At this massive fixed point, there are two degenerate minima about two signs of mass, and they correspond to two phases connected by this first-order transition. On the other hand, when $g < 0$, further renormalization reduces g to 0, and the system reaches a massless fixed point; this represents a second-order transition.

When the transition is second order, the critical theory is described by a conformal field theory (CFT) due to its dimensionality, (1+1). Each CFT is characterized by its

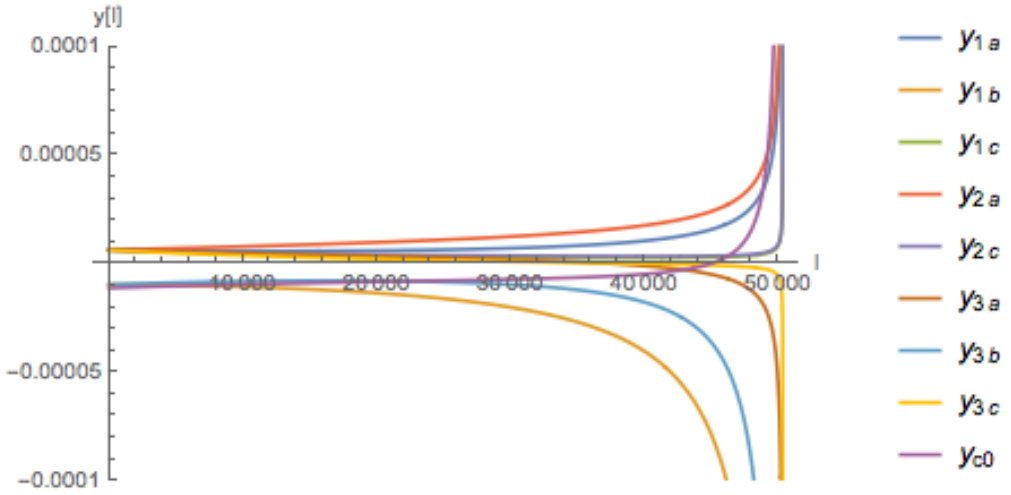

Figure 2.9: An example of RG flow

central charge, c, which roughly expresses the number of critical fields. $c = 1/2$ is the $\mathcal{Z}_2$ Ising critical theory, $c = 1$ is the U(1) Gaussian theory, and $c = 3/2$ is the $SU(2)_2$ Wess-Zumino-Novikov-Witten theory. With the duality mappings, it is easy to read off the central charge of each CFT. Since each Majorana fermion carries $c = 1/2$, the number of fields flipped by a mapping directly tells us the central charge. We will identify the phase transitions appearing in our phase diagrams more precisely later.

2.5.5 Results

A typical RG flow obtained by numerically integrating the RG equations are given in Fig. 2.9. In all the cases with equal velocities, we find that the coupling constants eventually exhibit the dynamical symmetry enlargement, and obtained phases are the ones predicted in the previous subsection. The phase diagrams obtained from the RG analysis are shown in Figs. 2.10 and 2.11. We also investigated the effect of velocity

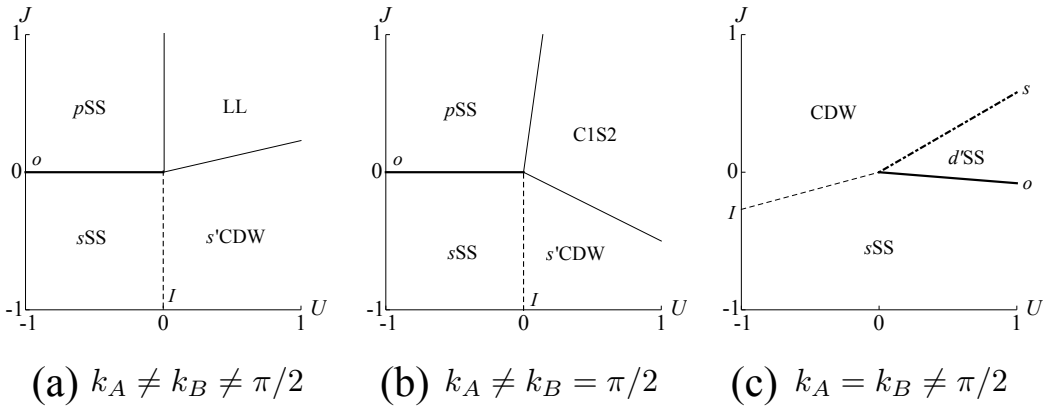

Figure 2.10: Bosonization phase diagrams for incommensurate cases [reproduced from Okamoto and Millis (2012)].

anisotropy to the phases in physically relevant parameter region, $U/2 > J > 0$ in Fig. 2.12, using the RG equations based on the fermionic Hamiltonian. We studied the range, $10 \geq v_A/v_B \geq 1$.

With inequivalent Fermi momenta at incommensurate filling (Fig. 2.10), the physically relevant region is covered by a Luttinger Liquid (LL) phase, where all the modes are massless, and the s'CDW phase. The transition between massive phases and a LL phase is Kosterlitz-Thouless (KT) in the sense that a LL phase is critical with a power-law correlation, while massive phases have exponentially decaying correlations. The HF phase diagram in this case is similar to the RG phase diagram. We have the $p(s)$SS state with large negative U and small positive (negative) J. For large negative J, we have the s'CDW state. The pTS and SDW states appearing in positive J regime of the HF phase diagram are renormalized to the Luttinger liquid phase. As the velocity anisotropy becomes larger, the s'CDW phase is gradually suppressed, and whole area in physically relevant region is covered by the LL state for $v_A/v_B \geq 6$. The population imbalance and velocity difference between orbitals largely suppress

the scattering processes, leading to a LL phase.

Even when one of the orbital is half-filled, the phase diagram does not change much [Fig. 2.10(b)]; only the Luttinger liquid state is replaced by a $C1S2$ phase, where a commensurate band opens a charge gap, and the rest of the modes remain massless. This is an orbital-selective Mott state. The velocity anisotropy in both directions, $v_A/v_B < 1$ and $v_A/v_B > 1$, does not modify the $C1S2$ state in the region, $U/2 > J > 0$.

The phase diagram for the orbital degenerate case ($k_A = k_B$) is given in Fig. 2.10(c). The HF phase diagram of this case [Okamoto and Millis (2011)] has the SDW phase for $0.6U > J > 0$, which corresponds to the d'SS phase found by bosonization; both of them are locally high-spin states. In the negative J region, we have the sSS state, while the HF calculation gives not only the sSS state, but also a large region of the s'CDW phase. As we mentioned, this CDW state is Ising dual to the S-Mott phase, which is the insulating analogue of the sSS state. In the large $J > 0$ region, we found p'_y-wave spin-triplet superconductivity in the HF phase diagram, which is replaced by CDW in the bosonic calculation. The CDW state around $-U > J > 0$ is robust, and we observe it both at HF level and after renormalization. The velocity difference in a quadrant, $U, J > 0$, does not modify the large J regime, though a $C2S1$ state appears at small J [Fig. 2.12 (a)]. The $C2S1$ phase was observed in other two-leg ladder systems when the velocity difference becomes large [Balents and Fisher (1996); Chudzinski et al. (2008)].

For the system at half filling, but with two different Fermi momenta, the phase diagram is given in Fig. 2.11(a). There is a narrow Luttinger Liquid (LL) phase near $U \simeq J > 0$. Again, transitions between the LL phase and massive phases are KT type except the total charge mode remaining massive in both phases. The D'-Mott and $S(')$-Mott states can be understood as the reminiscent of the pSS and sSS phases which exist away from half-filling. The corresponding HF phase diagram shows the

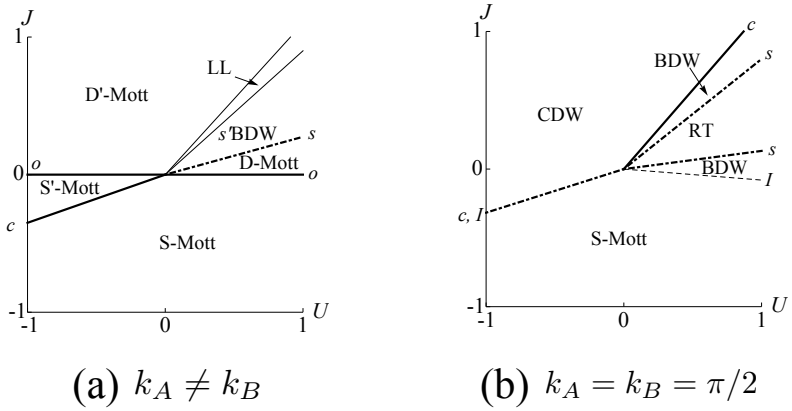

Figure 2.11: Bosonization phase diagrams for commensurate cases [reproduced from Okamoto and Millis (2012)].

SDW and s'SDW states in the physically relevant region [Okamoto and Millis (2011)], while they are replaced by the s'BDW and D-Mott phases in the RG phase diagram. The CDW phase, which dominates large positive J region at mean-field level, is replaced by the D'-Mott state after renormalization. For this case, the pSS state, the metallic analogue of the D'-Mott state, is subdominant with large positive J at the HF level, and this is more enhanced than the CDW order during the renormalization flow. Negative J region of the HF phase diagram is again covered by the sSS and s'CDW phases, which are related to the $S(')$-Mott state. In this case, the velocity difference does not modify the phase diagram in physically relevant region essentially.

Now we look at the orbital degenerate case, $k_A = k_B$ [Fig. 2.11(b)]. The phase diagram is similar to the one away from half filling if we replace the insulating states to corresponding metallic ones; S-Mott to sSS, RT to d'SS, and BDW to CDW. Although precise boundaries do not coincide exactly, the corresponding HF phase diagram shows similar structure [Okamoto and Millis (2011)]. There, we have the SDW phase instead of the RT state in $U > J > 0$; they are both locally high-

spin configurations with anti-ferromagnetic orders along the chain. The S-Mott state found in the bosonization result corresponds to mainly the degenerate state of the s'CDW and pCDW orders with a smaller region of sSS in the HF phase diagram. In the bosonic language, the order parameter of the sSS phase is the same as that of the S-Mott state except the total charge mode. The s'CDW and pCDW states are degenerate due to the orbital symmetry, and they are Ising dual to the S-Mott and Haldane orbital (HO) phases respectively. The CDW state stays almost the same regime in both phase diagrams. The BDW phase does not appear in the HF phase diagrams, since its HF energy is higher than that of the CDW phase.

There is a notable difference between the orbital degenerate case, and non-degenerate case. When $k_A = k_B$, locally high-spin states, RT and d'SS, are dominant in $U/2 > J > 0$, while low-spin configurations, s'BDW and D-Mott, are found for $k_A \neq k_B$. We understand these low-spin states as a result of decoherence by two different wave numbers. In essence, density waves with different phases in the two bands mean that the energy contribution from the J interaction averages out to zero.

We noticed that the phase transition from the RT state to the CDW state with increasing J is similar to the SDW-CDW transition found in the extended Hubbard model (EHM) [Nakamura (2000); Tsuchiizu and Furusaki (2002a)]. The EHM has a nearest neighbor interaction, Vn_jn_{j+1}, in addition to the Hubbard interaction, $Un_{j\uparrow}n_{j,\downarrow}$. As the former interaction becomes predominant, particles try to form a CDW state, while strong U prefers SDW. In the weak coupling regime, it is found that the SDW state undergoes a spin-gap transition to a BDW state, and then becomes the CDW state through a Gaussian transition of the charge sector. In the strong-coupling regime, these two transition lines are coupled to a first order transition line. In our model, strong J plays the same role as V in the EHM; large J induces an attractive on-site interaction [see Eq. (2.2)] leading to the CDW state. The properties of transitions from the RT phase to the CDW phase, and the existence of the narrow BDW region

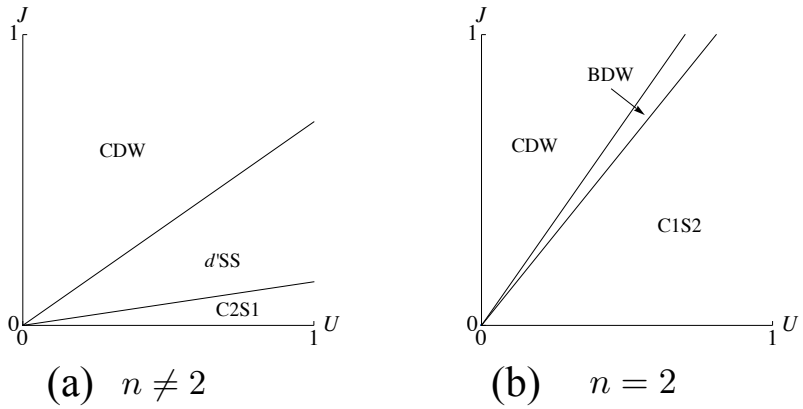

Figure 2.12: Bosonization phase diagrams with different velocities [reproduced from Okamoto and Millis (2012)]

are also the same as in the EHM. Therefore, we expect that in the strong-coupling regime, the RT-CDW transition in our model also becomes first order, although this has not been demonstrated.

Now, we consider the effect of velocity difference in the first quadrant; $U, J > 0$ [Fig. 2.12(b)]. As v_A/v_B becomes as large as 1.5, we found that the RT and BDW states in small $J > 0$ are completely replaced by a $C1S2$ state, where only a charge mode of a single band becomes massive, and the rest is massless. The CDW and BDW states in $J > U > 0$ are robust to the change in velocity. This is because the large anisotropic velocities suppress the interband scattering, resulting in the domination of intraband scattering. As v_A/v_B is increased beyond 1.5, the $C1S2$ phase becomes larger, although the BDW phase always exists between the CDW and $C1S2$ phases.

2.6 Spin-polarized solutions

Lastly, we examine the possibilities of having a density polarization such as ferromagnetism and orbital ferromagnetism. Considering the fact that a bulk Co crystal is a ferromagnet, it is quite important to consider the effects of such polarizations in order to understand the experimental results. Since the Stoner's argument shows that the spatially uniform order develops above a certain interaction strength, we investigate the strong coupling regime ($U \gg J \gg t$) in the following.

2.6.1 Mean-field results

Here we show a mean-field phase diagram. Since we are mostly interested in high-spin states, we compared the energies of following four ferromagnetic states and four antiferromagnetic (or SDW) states:

(1) FM, FM(+OFM), FM+ODW, FM+OAFM

(2) SDW, AFM, OFM+SDW, OFM+AFM,

where AFM stands for antiferromagnetism, and OAFM is orbital-antiferromagnetism. In particular, we will distinguish two spin-density waves: the AFM state with $q = \pi$ and the SDW state with $q = 2k_F$. The two states are identical when $k_F = \pi/2$ but while the SDW state is driven by a Fermi surface instability and is the only important state in the limit of weak coupling, the AFM state is stabilized by commensurability (Umklapp) effects and may exist for a range of carrier concentrations near the commensurate value. We similarly define the orbital density wave (ODW) with a wave vector $q = 2k_F$, and the OAFM state with a wave vector $q = \pi$.

For simplicity, we assumed two degenerate bands with a constant density of states. The particle-hole symmetry allows us to investigate only $0 < n < 2$. Comparing the

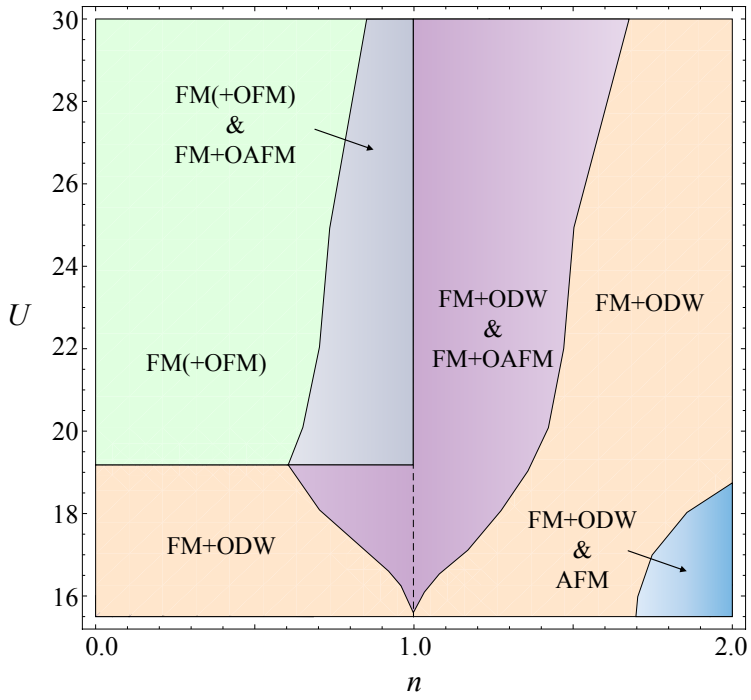

Figure 2.13: Mean-field diagram for strong coupling [reproduced from Okamoto and Millis (2011)]

energies of the eight states discussed above, we obtained the ground state phase diagram which is given in Fig. 2.13. Below quarter-filling, the FM(+OFM) state – where only single band is occupied – is dominant with large U; this configuration does not cost any interaction energy. The transition between the FM+ODW and FM(+OFM) states below $n = 1$ can be understood by Stoner's scenario where the orbital sector becomes polarized above a critical value U_c. The precise behavior of the phase boundary as $n \to 0$ depends on details; for example, the DoS of an isolated chain diverges at very small n leading to the smaller value of critical interaction strength.

As the filling becomes closer to quarter-filling, the FM+OAFM state is found to be stable because it can use Umklapp processes to cancel the static interaction energy, although this solution is unstable if too many holes or electrons are doped

[see Eq. (2.19)]. As we plot the energies of these states, we found that a phase separated state exists below $n = 1$. This state is the mixture of the FM+OAFM and FM(+OFM) states for large U and of the FM+OAFM and FM+ODW states for small U. At exactly quarter-filling, the system is a homogeneous FM+OAFM state.

Above quarter-filling, the FM+ODW state is more stable than the FM(+OFM) and FM+OAFM states; the energy of the FM+ODW state in the strong coupling regime is roughly

$$E \sim \frac{1}{8}(U - 3J)n^2, \tag{2.83}$$

while the energies of the FM(+OFM) and FM+OAFM states are linear in n, $E \sim (U-3J)(n-1)$. Thus, the FM+ODW state is energetically preferable above $n \approx 1.18$. Again the transition from the FM+OAFM state to the FM+ODW state is smeared by a phase separated state of these two.

Near half-filling, $n \approx 2$, an AFM state appears in the weak U regime by the same reason for the FM+OAFM phase to appear around quarter-filling. However, the kinetic part of the AFM state does not cancel the static part completely, and the residual interaction makes this state unstable as U gets larger. The AFM state forms an inhomogeneous mixed state with the FM+ODW state below half-filling, and at half-filling, the system is totally occupied by the AFM state.

Now, we would like to compare our mean-field phase diagram to previously obtained results. At quarter-filling ($n = 1$), Kugel and Khomskii (1972), and Cyrot and Lyon-Caen (1975) found the FM+OAFM state as the ground state by strong coupling expansion, and this is confirmed by numerical calculations [Gill and Scalapino (1987); Sakamoto et al. (2002)]. This result can be understood as follows: When spins are totally aligned, Fermi momenta are doubled, and effectively the system is at half-filling. Then we may regard the orbital index as pseudospins, and the system exhibits a pseudospin density wave, i.e., OAFM.

Away from quarter-filling, the Umklapp process is killed so we expect OAFM is less dominant; indeed, Sakamoto et al. (2002) found the FM+ODW state with a tight-binding DoS. They also found that adding further neighbor hopping to get a constant DoS replaces the FM+ODW state with a paramagnetic state ($S = 0$) for $n < 1$ though the system remains FM for $n > 1$. This is because the FM state is induced by double-exchange mechanism for the electron-doped case, but for the hole-doped case, it is driven by purely one-dimensional "spin-charge separation," [Ogata and Shiba (1990)], which is fragile to perturbation of further-neighbor hopping. These observations do not contradict our result above quarter-filling, though we have the FM(+OFM) state instead below quarter-filling. We think the FM(+OFM) state is actually more or less similar to the paramagnetic state without double occupancy in Sakamoto et al. (2002), since both configurations do not cost any interaction energy below quarter-filling. The mean-field treatment picks up the FM(+OFM) state among other configurations which do not have doubly occupied sites. On the other hand, the ferromagnetism in Sakamoto et al. (2002) is induced by spin-charge separation, which is not a phenomenon captured by mean-field theory. Therefore, we conclude that the ferromagnetism of the FM(+OFM) state in Fig. 2.13 and the state seen in the numerical results of Sakamoto et al. (2002) have different origins.

At half-filling, the system is claimed to be a Haldane type where fully-polarized spin 1 on each site are antiferromagnetically coupled by exchange interactions. Slightly below half-filling, a phase separation between the Haldane phase and the FM+ODW phase was found [Sakamoto et al. (2002)], which agrees with our results for small U.

2.6.2 Bosonization results

In this subsection, we investigate the possible orbital orders by bosonization assuming that the system is fully spin polarized. In other words, we consider the effect

of residual backscattering in the subspace of the charge and orbital sectors assuming the spin excitations are frozen. We leave the investigation of the regime close to half filling for future study.

Suppose that all the electrons have the same spins, the model in Eq. (2.1) and Eq. (2.2) is then reduced to,

$$H = H_{\text{kinetic}} + \sum_i (U - 3J)\, n_{iA} n_{iB}, \tag{2.84}$$

where we omit the spin index. Now the $\mathrm{SU}(2)_s$ symmetry is lost, but we can regard the orbital part as pseudo spins. If the two bands have the same k_F and velocities, the system has the orbital SU(2) symmetry. The band splitting in orbital sector is isomorphic to the Zeeman splitting by magnetic field. Therefore, the model now turns to a simple Hubbard model with effective interaction $U_{\text{eff}} = U - 3J$, with or without magnetic field.

Depending on the effective crystal field splitting between the two orbitals Δ, and the band widths, there may be three different scenarios in this model. The first case is that the two bands are completely degenerate: $\Delta = 0$, and $k_A = k_B$. We expect a staggered orbital order to appear. On the other hand, when there exists either small splitting or when the band widths are slightly different, the two momenta are not equal, and orbital orders might be suppressed. We will discuss these two scenarios below using bosonization method. However, there is another scenario, which may arise when either splitting is large, or two band widths are greatly different. Then, only one band has states at the Fermi surface and the physics is trivial.

We first look at the degenerate case, $k_A = k_B$, corresponding to the absence of magnetic field. The bosonized form of the Hamiltonian in Eq. (2.84) at half filling is

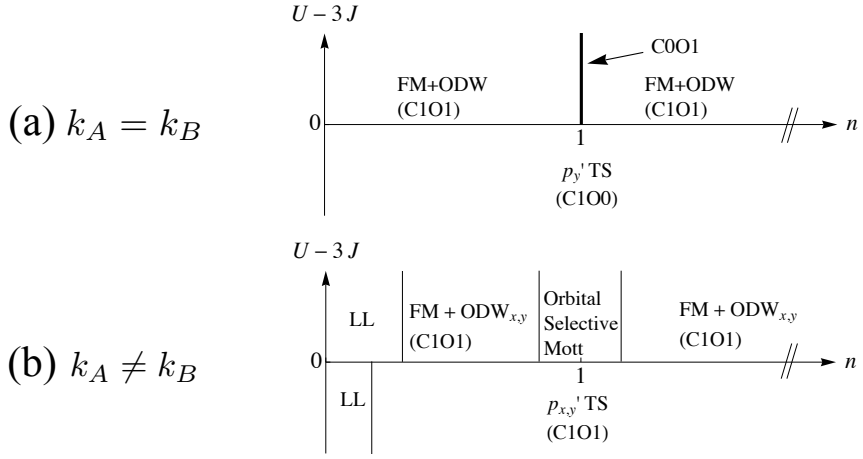

Figure 2.14: Bosonization phase diagram with spin polarization [reproduced from Okamoto and Millis (2012)].

given by

$$\begin{aligned}\mathcal{H} = \frac{1}{2\pi}\sum_{\nu=c,o} v_\nu \left[K_\nu(\nabla\theta_\nu)^2 + \frac{1}{K_\nu}(\nabla\phi_\nu)^2\right] \\ + \frac{2}{(2\pi\alpha)^2}U_{\text{eff}}\cos\left(2\sqrt{2}\phi_o\right) \\ - \frac{2}{(2\pi\alpha)^2}U_{\text{eff}}\cos\left(2\sqrt{2}\phi_c\right),\end{aligned} \tag{2.85}$$

where the Luttinger parameters and velocities are,

$$K_c v_c = K_o v_o = v \tag{2.86}$$

$$v_{c(o)}/K_{c(o)} = v\left(1 \pm \frac{U_{\text{eff}}}{\pi v}\right). \tag{2.87}$$

Thus, the charge and orbital modes are decoupled, and each mode has a SU(2) symmetry. The total symmetry is SU(2) × SU(2) = SO(4).

Translating the analysis for the Hubbard model [Giamarchi (2003)] to our charge-

orbital model, we found the following results. For incommensurate filling, the last Umklapp term in Eq. (2.85) vanishes, and the charge mode is massless. Also the $SU(2)_c$ symmetry is broken to $U(1)_c$. About the orbital sector, we find:

(1) $U_{\mathbf{eff}} > 0$ Orbital density wave (ODW) has the longest correlation, and both orbital and charge modes are massless. The $SU(2)_o$ symmetry requires that ODW's about all three directions (x, y, z) are degenerate.

(2) $U_{\mathbf{eff}} < 0$ The orbital sector becomes massive, and the phase with slowest decaying correlation is orbital-singlet superconductivity with parallel spins ,i.e., p'_yTS in Okamoto and Millis (2011).

At half filling, the charge mode becomes massive ($K_c = 1/2$) when the effective interaction is repulsive; the system is Mott insulating. The orbital part still gives ODW, and this FM+ODW state in $U > 3J$ regime is observed both analytically [Kugel and Khomskii (1972); Cyrot and Lyon-Caen (1975); Okamoto and Millis (2011)] and numerically [Gill and Scalapino (1987); Sakamoto et al. (2002)]. For the attractive side, the charge mode is gapless ($K_c = 1$) with an orbital gap by the p'_yTS order; this is the Luther-Emery phase. This triplet superconductivity agrees with the numerical result by Sakamoto et al. (2002). The results are summarized in Fig. 2.14.

Now we turn to the case with $k_A \neq k_B$; there is a pseudo magnetic field acting on the orbital space. At very small filling, only a single band is filled, so the ground state is ferromagnetic Luttinger liquid of a single gapless mode. When we dope enough the two bands start to share the Fermi surface. The $SU(2)_o$ symmetry is reduced to $U(1)_o$, and the $\cos\left(2\sqrt{2}\phi_o\right)$ term vanishes due to two different Fermi momenta. Thus, the orbital sector is always massless. With an attractive interaction, the band degeneracy occurs with smaller filling than with a repulsive interaction, since we guess the upper band is pulled down by the lower filled band for $U_{\text{eff}} < 0$. The charge mode is massive (massless) for repulsive (attractive) interaction at half filling. At tree-level, the states

with longest correlations are ODW_x and ODW_y for $U_{\mathrm{eff}} > 0$, and $p'_x\mathrm{TS}$ and $p'_y\mathrm{TS}$ for $U_{\mathrm{eff}} < 0$. Since the orbital symmetry is explicitly broken, the exponents of correlation may differ for different directions. Finally, contrary to the complete degenerate case, we speculate that an orbital selective Mott phase appears near $n = 1$ for inequivalent bands; once one band is half filled, the commensurate wave vector opens a gap, and the other band remains metallic. Further filling just goes to the metallic band until it reaches half filling. Fig. 2.14 presents the general phase diagram for this case.

2.6.3 Indications of first-principles calculations

Here we briefly explain the relevant numerical results obtained by density functional theory (DFT) [Zaki et al. (2013)]. The calculations simulate isolated Co nanowires, whose width of the terrace is six Cu atomic wide ≈ 14 Å. The key finding of the DFT simulation is that the ground state shows dimerized Co atoms, whose d-shell occupations are fully spin polarized, and that the spins are ordered in a ferromagnetic manner. Antiferromagnetic order has higher energy, and does not favor the structural distortion. The energy difference between two magnetic structures are due to the cost of hopping between neighboring sites; with the antiferromagnetic order, electrons need to flip their spins paying the extra cost of the spin exchange energy. The origin of the structural distortion is understood from the band occupancy of the ferromagnetic state. The orbitals with the majority spins are fully occupied while the ones with minority spins are nearly half-filled (Fig. 2.15). Thus, from the Peierls argument, inducing dimerization for the electrons with minority spins can further lower the total energy.

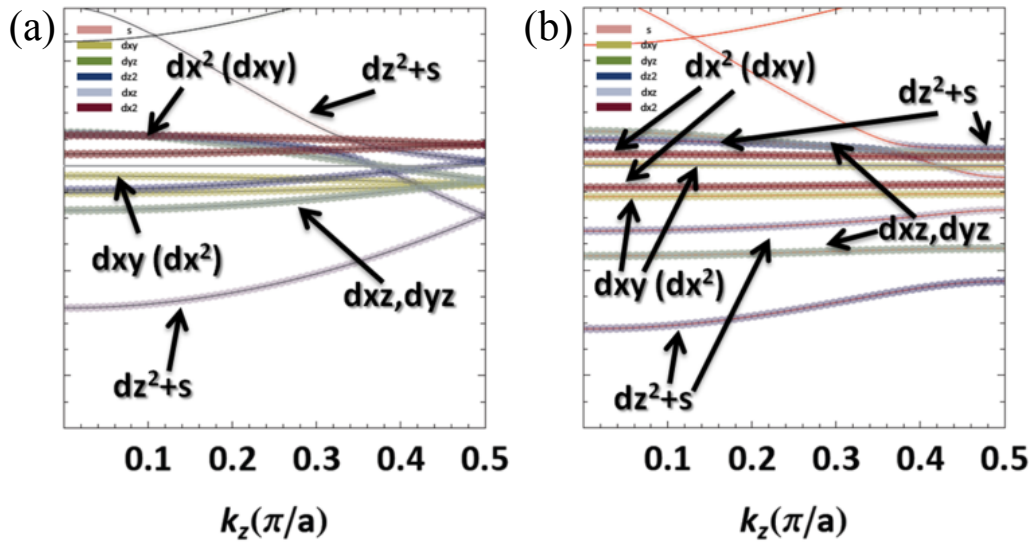

Figure 2.15: Band structures of Co nanowires on a stepped Cu surface (a) without structural distortion and (b) with structural distortion [reproduced from Zaki et al. (2013)].

2.7 Conclusions

In this chapter, we investigated a one-dimensional two-orbital Hubbard model, possibly relevant to a transition metal nanowires. From the mean-field analysis, we find that, in a physically relevant parameter region, in a weak coupling limit, various SDW orders (SDW, s'SDW, and pSDW) are dominant similarly to the simple Hubbard model (Figs. 2.4, and 2.5). The velocity difference between two orbitals suppresses the interband processes, while in order to completely suppress it, it requires the ratio of the two velocities to be $\sim$ 40 (Fig. 2.6). From the bosonization and renormalization group analysis, we find that quantum fluctuations drive the system into non-trivial fixed points such as BDW, RT, D-Mott, and d'-SS phases (Figs. 2.10, and 2.11). In particular, the RT and d'-SS phases are locally high-spin configurations, which we expected from the Hund coupling. By lifting the degeneracy and doping away from the commensurate values, orbital selective Mott phase, and Luttinger

liquids appear. These results do not agree with the ferromagnetic ground state with dimerization seen in the experiment and the DFT simulation [Zaki et al. (2013)]. This indicates that the important physics are beyond the weak coupling regime of our model.

In a strong coupling limit, ferromagnetic order is dominant in the mean-field phase diagram (Fig. 2.13). Although the first principle calculation indicates also a ferromagnetic ground state, our calculation does not show a dimerization. An important missing ingredient for our model is the effect of the substrate or phonons, which prefers to form a CDW state instead of the orbital density waves, which are more preferred by the electron-electron interactions. Therefore, generalizing our model to the one with a lattice might be an interesting future problem.

Chapter 3

Effects of impurities on the charge-density wave in $NbSe_2$

3.1 Overview

In this chapter, we consider the effects of dilute but strongly pinning impurities on the charge-density wave in $NbSe_2$. First, we give a brief explanation about $NbSe_2$, and its CDW order. Then we analyze the experimental data obtained from STM measurements, and argue that the impurities in the material are dilute, but strongly pinning. Our analysis shows that the CDW phase is still topologically ordered, with quasi-long-range autocorrelations, i.e., a Bragg glass. This result cannot be explained by the conventional theories, which we explained in Sec. 1.4. In order to understand such a behavior, we analytically and numerically study a Ginzburg-Landau model in Secs. 3.4 and 3.5 respectively.

3.2 Background

A class of transition metal calcogen compounds are prototype inorganic materials showing charge-density waves at low temperatures. Their crystal structures are spatially anisotropic, and transition metal trichalcogenides as $NbSe_3$ are quasi-one-dimensional while transition metal dichalcogenides as $NbSe_2$ are quasi-two-dimensional.

In this section, we will focus on 2H-$NbSe_2$, and explain the properties of the CDW phase of this material.

The crystal structure of $NbSe_2$ is depicted in Fig. 3.1. Its unit cell consists of two blocks of Se-Nb-Se layers; the Nb atoms in each layer form a triangular lattice and the electrical conductivity is much larger for in-plane directions. Scattering [Moncton et al. (1977)] and specific heat [Harper and Geballe (1975)] measurements indicate that a second order phase transition occurs at $T_c \approx 34$ K; below this temperature a charge density wave forms. The charge density wave involves condensation of electronic density at three wavevectors $\vec{Q}_{i=1,2,3}$ related by 120° rotations. $|\vec{Q}_i| \approx \vec{G}_i/3 \approx 0.7$ Å^{-1} with $\vec{G}_i$ the smallest nonzero reciprocal lattice vectors. The CDW wavevectors are slightly deviated from the commensurate values by 2%. We may write the modulation of the electron density $\delta\rho$ in the charge density wave phase as

$$\delta\rho(x) = \sum_{i=1}^{3} \Re\left(\psi_i(\vec{x})e^{i\vec{Q}_i\cdot\vec{x}}\right) \tag{3.1}$$

The CDW order parameters ψ_i are complex numbers that may be written in terms of a real magnitude η_i and a phase ϕ_i. Deviations from perfect charge density wave order involve spatial variations of η and ϕ. Phenomenological theory using Ginzburg-Landau models of this type can be found in McMillan (1975); Walker and Jacobs (1982); Nakanishi and Shiba (1984). The relevant part for our later analysis is

$$F = t\sum_{i_1}^{3}|\psi_i|^3 + c_3\Re\psi_1\psi_2\psi_3 + b_1\sum_{i_1}^{3}|\psi_i|^4 + b_2\sum_{i\neq j}|\psi_i|^2|\psi_j|^2 + \cdots . \tag{3.2}$$

A crucial issue in the following analysis is the dimensionality of the system. While $NbSe_2$ has very anisotropic electronic properties [Dordevic et al. (2001)], we believe that the appropriate CDW model is three dimensional for the following reasons. First, three dimensional critical scattering is observed in the similar compound 2H$-TaSe_2$ [Moncton et al. (1977)], with correlation lengths in the in-plane and out-of-plane

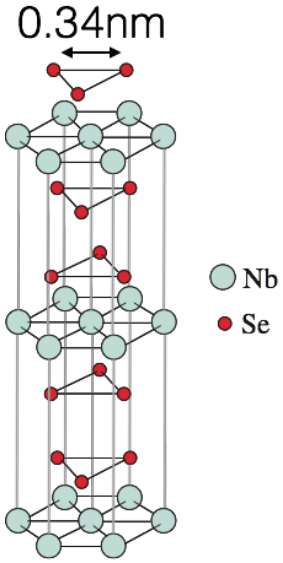

Figure 3.1: Crystal structure of 2H-$NbSe_2$ [reproduced from Wang et al. (2009)]

directions differing only by a factor of three. Second, below the transition temperature, the development of the order parameter agrees with mean-field theory [Moncton et al. (1977)], while a two dimensional incommensurate CDW cannot show a true long-range order [Mermin and Wagner (1966); Hohenberg (1967); Coleman (1973)]. Third, a first-principles calculation showed that single layer $NbSe_2$ does not exhibit the 3×3 periodicity [Calandra et al. (2009)]. These arguments suggest that, most likely because of lattice effect, the CDW in $NbSe_2$ is not unusually anisotropic. Indeed, the importance of lattice effect in this material has been recognized since the theoretical work by McMillan (1977) showing that the displacive model by phonons better explains the CDW transition rather then BCS or nesting scenario. Such an observation is further supported by inelastic X-ray scattering measurements finding a large collapse of a phonon mode around the CDW wavevector [Weber et al. (2011)]. Also, the hydrodynamic pressure does not change the CDW wavevector, indicating the irrelevance of the Fermi surface nesting to the formation of the CDW. Considering

these, it seems appropriate to consider that the CDW in $NbSe_2$ is three dimensional, while the electronic response is more anisotropic. Thus, in the following analysis, we assume that the system is three dimensional unless explicitly mentioned.

3.3 Analysis of STM data of $NbSe_2$

In this section, we present various quantities obtained from STM measurements on a surface of $NbSe_2$ at 22 K. All the measurements were done by Carlos J. Arguello, and Ethan P. Rosenthal. First, we show a topographic picture of the surface, and argue that the impurities are strongly pinning the CDW phase. Next, autocorrelations of the amplitude, and total charge modulations are presented. The data indicate that the impurities have more severe effects on the phase of the CDW rather than the amplitude. The order parameters of the CDW are extracted from the topographic image, and the local modulations of phases by impurities are directly observed. To study the topological defects near impurities in the phase of the CDW, we construct a Delaunay diagram. We find that the dislocations always appear in pairs, and that the system is topologically ordered up to the scale of the picture. Thus, the system is in a Bragg glass phase. In summary, the data imply that the impurities observed in this $NbSe_2$ sample are strong pinning centers, but nevertheless leave the system in a Bragg glass phase, in apparent disagreement with the conventional idea that the strong impurities induce free topological defects and completely destroy the long-range order [Fukuyama and Lee (1978); Lee and Rice (1979)]. Some of the detail procedures about data processing are given in Appendix B.

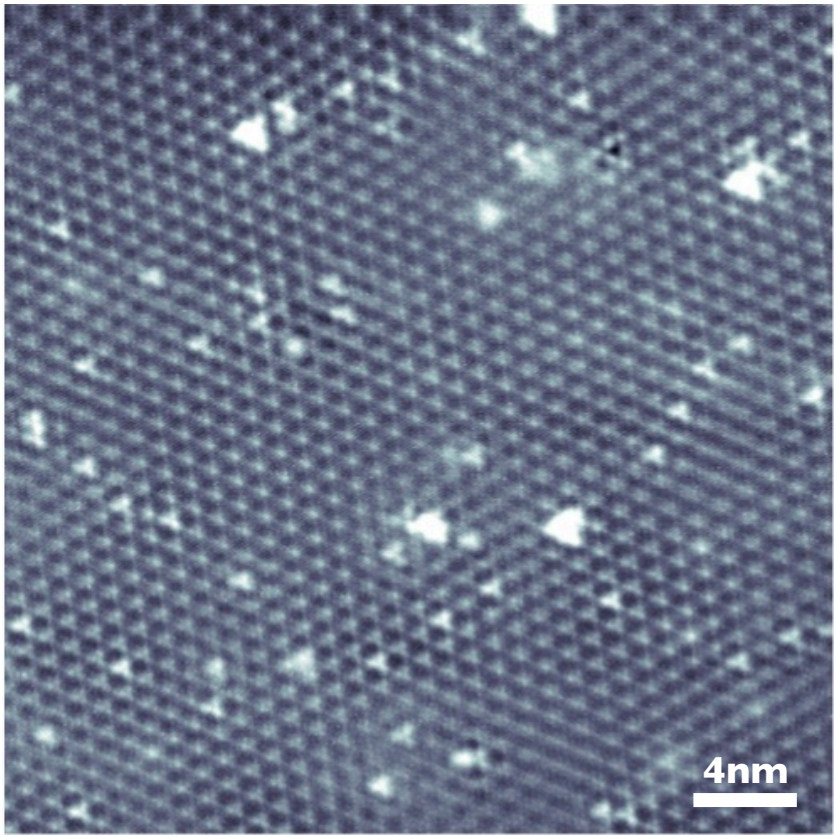

Figure 3.2: A topographic image of a $\sim$ 32 nm $\times$ 32 nm region of $NbSe_2$ at 22 K $< T_c = 34$ K taken under conditions of constant sample-tip current and bias voltage [reproduced from Okamoto et al. (2014)]. Data was taken by C. Arguello, E. Rosenthal, and A. Pasupathy. The heavy white spots are the strong pinning centers.

3.3.1 Topography

We use the scanning tunneling microscopy (STM) data shown in Fig. 3.2 to obtain real-space information about the spatial dependence of the amplitude $\eta(x)$ and phase $\phi(x)$. The sample used here is the one described in Arguello et al. (2014), and is made by vapor transport. The cleaved surface is believed to be a Se layer, since a Se-Se bond is van deer Waals, while a Se-Nb bond is Coulombic. Fig. 3.2 shows the topographic image of the cleaved surface at 22 K $< T_c = 34$ K. The voltage and

current are fixed to be −100 mV and 20 pA respectively. The measured signal is the vertical displacement of the STM tip; this depends on the physical topography and on the near Fermi-level electronic density of states at the tip position (Sec. 1.5). The large number of lighter white spots form an approximately triangular lattice with mean lattice constant $\lambda \sim 1$ nm about three times the basic lattice constant, consistent with the CDW wavevector found in scattering measurements [Moncton et al. (1977)]. We therefore believe that these are local maxima in $\delta\rho$ arising from CDW formation. The small number of heavy white spots indicate impurities. There are about 40 impurities in this field of view, which contains $\sim 10^3$ CDW unit cells; in other words, the impurity density $n_{\mathrm{imp}} \simeq 0.4\%$. The signal associated with impurities may come either from a physical change in surface height (associated e.g. with an impurity in the Se layer) or from a change in the local density of states. However, one may see that in almost all cases the impurity sits in the center of a hexagon of CDW maxima and has a triangular shape of size $\lesssim 1$ nm consistent with interference of three CDW wave vectors [Fig. 3.3(c)]. This suggests that a significant contribution of the impurity signal arises from impurity-induced modulations of the density of states, and that in particular impurities lead to an increase in the local density of states which acts as a strong pinning center fixing the local CDW maximum to the impurity site.

In order to confirm this basic observation, in Figs. 3.3, we show the bias voltage dependence of topographic pictures, whose amplitudes are normalized such that maximum and minimum are fit into $[-0.5, 0.5]$. First, as the voltage increases from the negative one to the positive one, we see that the shape of CDW changes from a configuration with three deep minima surrounding one maximum to the one with six shallow minima. This change of the number of minima is due to the change of CDW phases, and can be understood as follows. The total CDW density is given by the linear superposition of three CDWs as in Eq. (3.1). The three phases ϕ_i can be

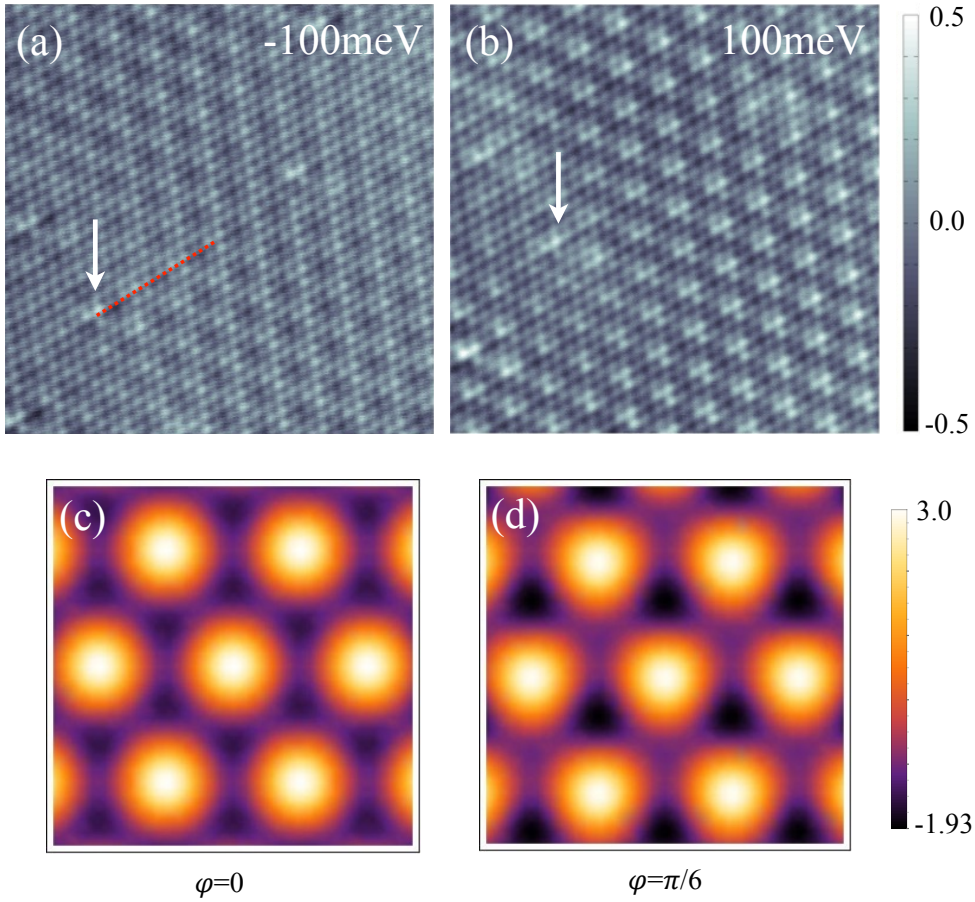

Figure 3.3: Topographic pictures at different bias voltages [reproduced from Okamoto et al. (2014)]. Data was taken by C. Arguello, E. Rosenthal, and A. Pasupathy. Arrows indicate the same impurity site at difference voltages. The intensity along the dotted line, which includes an impurity at the left end, is given in Fig. 3.4 for negative and positive voltages respectively. (c) and (d) are the density modulations at $\varphi = 0$ and $\varphi = \pi/6$ with $\eta = 1$ in Eq. (3.1).

decomposed into the relative displacement vector $\vec{u}$ and the total phase φ,

$$\phi_i = \vec{u} \cdot \vec{Q}_i + \varphi. \tag{3.3}$$

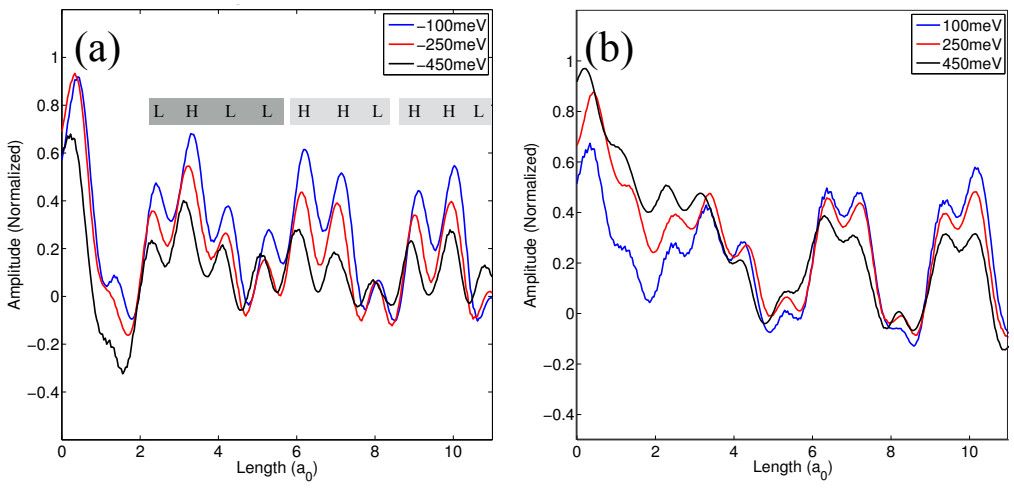

Figure 3.4: Line-cut pictures near an impurity [reproduced from Okamoto et al. (2014)]. Data was taken by C. Arguello, E. Rosenthal, and A. Pasupathy. The intensity along the dotted line in Fig. 3.3, which includes an impurity at the left end for negative and positive voltages respectively. We set the absolute maxima of the intensity in each picture to 1. In (a), the periodicity of CDW is expressed by the ordering of high maximum "H", and low maximum "L". Near the impurity, the periodicity is distorted from the ideal one "HHL".

We depicted the density modulation given by Eq. (3.1) with $\varphi = 0$ and $\pi/6$ in Figs. 3.3(c) and (d). With $\varphi = 0$, each maximum is surrounded by six equivalent shallow minima like a Kagome lattice, while the degeneracy among six is lifted once we make $\varphi \neq 0$. At $\varphi = \pi/6$, there are three deep minima surrounding one maximum. Therefore, at negative voltages φ is close to $\pi/6$, and at positive voltages φ seems closer to 0. The intensity modulations around impurities such as the one near the arrows in Fig. 3.3 follow the same change as the voltage changes, indicating that these modulations are triggered by the same mechanism as other CDW modulations, i.e., local density modulations not the height modulations.

Second, we also see in Fig. 3.3(a) and (b) that impurity sites are always at CDW maximum, and that the CDW amplitudes near them are enhanced, as more

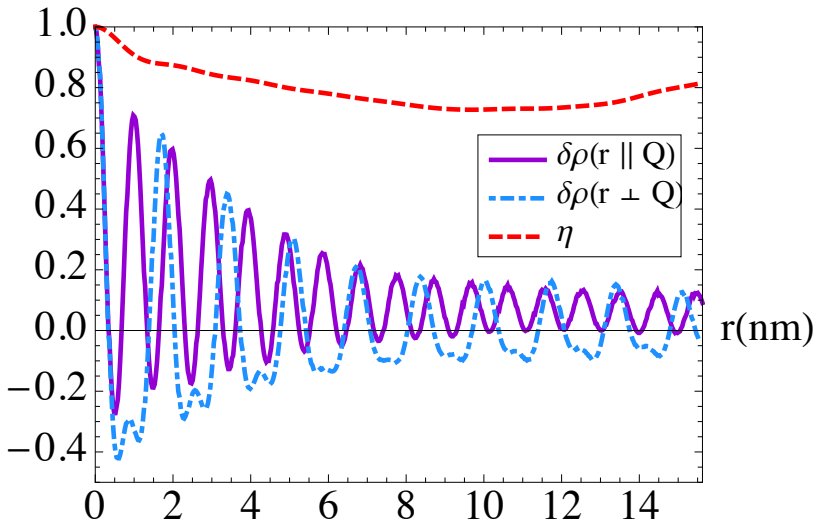

Figure 3.5: Autocorrelations of the CDW component $\delta\rho$ parallel to and perpendicular to a CDW wave vector $\vec{Q}_1$, and of the amplitudes η [reproduced from Okamoto et al. (2014)]. Data was taken by C. Arguello, E. Rosenthal, and A. Pasupathy.

clearly presented in the line-cut pictures in Figs. 3.4(a) and 3.4(b). For instance, in Fig. 3.4(a), in the vicinity of the impurity, the ideal periodicity, two high peaks followed by one low peak, is distorted to have a maximum at the impurity, and the CDW amplitude is increased as well. These observations indicate that impurities strongly pin the CDWs and distort them locally.

3.3.2 Autocorrelations

In Fig. 3.5, we present the autocorrelation of the experimental signal, interpreted as a density of states modulation. An unbiased autocorrelation of a quantity $A(\vec{x})$

confined in a finite size of $L \times L$ is defined as

$$\langle A(\vec{x})A(0)\rangle = \frac{\int d^2y A\left(\vec{x}+\vec{y}\right) A\left(\vec{y}\right)}{\int d^2y A\left(\vec{y}\right) A\left(\vec{y}\right)} \times \frac{L^2}{\text{Overlapped area}}. \tag{3.4}$$

The last factor normalizes the autocorrelation depending on the shifting vector $\vec{x}$. The integration becomes a summation for a discrete quantity. For the CDW component, we angular averaged the autocorrelations about $\pi/3$ rotations;

$$\bar{A}(\vec{x}) \equiv \frac{1}{3}\left[A(\vec{x}) + A(\vec{x}') + A(\vec{x}'')\right], \tag{3.5}$$

where $\vec{x}'$, and $\vec{x}''$ are the rotated coordinates of $\vec{x}$ by $\pi/3$ and $2\pi/3$.

We present both the density modulation relative to the average value, $\delta\rho$ and the absolute value or amplitude η. The amplitude autocorrelation is characterized by an initial rapid decay followed by a more gradual relaxation to a nonzero value while the autocorrelation of the total CDW modulation $\delta\rho$ decays exponentially with a decay length ~ 4 nm comparable to the inter-impurity spacing $l \approx 5$ nm. Taken together, these facts indicate that the main effect of the impurity is on the phase of the CDW order parameter.

3.3.3 Order parameters

The three order parameters are extracted from the topographic picture, and their phases are presented in Fig. 3.6. In general, the phases are coherent over large regions if we ignore the overall drifts. These drifts are artificial and not intrinsic properties of the CDW (see Appendix B for details). While all impurities produce a local maximum in the amplitude of the order parameter, different impurities have different consequences for the phase. The two insets show expanded views of the phase near impurity sites. The right inset shows an impurity that induces a smooth and small

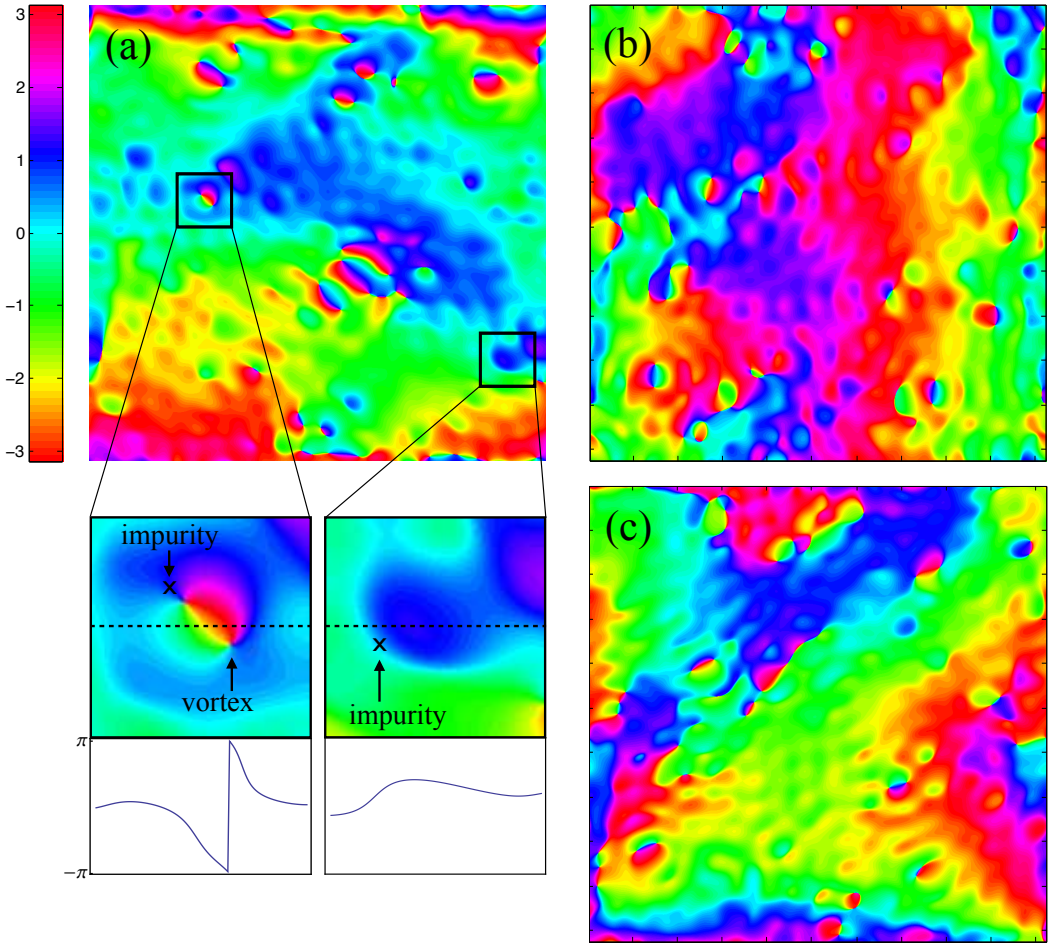

Figure 3.6: The phases of three order parameters [reproduced from Okamoto et al. (2014)]. Data was taken by C. Arguello, E. Rosenthal, and A. Pasupathy. The gradual change along the horizontal axis in (b) is an artifact in order to take the ordering vector $\vec{Q}_i$ such that $\sum_i \vec{Q}_i = 0$; $\vec{Q}$ are specified only through integer numbers due to the periodic boundary conditions for the Fourier transformation.

phase modulation. The left inset shows that a different impurity induces a large phase modulation from $-\pi$ to π as we move in a counterclockwise fashion around the defect. Only about $\sim 20\%$ of the identifiable defects produce 2π phase modulations;

the remainder produce smoothly varying modulations of the phase. Interestingly, at slightly larger distances from the impurity shown in the lower left inset of Fig. 3.6, the phase variation becomes smooth; the impurity actually induces a bound vortex-antivortex pair.

Expressing the phase in the different notation in Eq. (3.3) is also useful. If φ is fixed to a specific value, this indicates that the cubic term in the Ginzburg-Landau energy, Eq. (3.2), is strong enough to pin φ. As a physically distinct choice of the phases, we restrict their values to be

$$-\pi \leq \vec{Q}_{1,2} \cdot \vec{u} < \pi, \tag{3.6}$$

$$-\frac{\pi}{3} \leq \varphi < \frac{\pi}{3}. \tag{3.7}$$

One difficulty arises since the corresponding ϕ_i are multivalued. The first restriction leads to

$$-\pi + \bar{\varphi} \leq \phi_{1,2} < \pi + \bar{\varphi}, \tag{3.8}$$

so if we know $\bar{\varphi}$, we can obtain $\vec{Q}_{1,2} \cdot \vec{u}$ from these. ϕ_i are restricted in $[-\pi, \pi]$, and then we can find $\vec{Q}_{1,2} \cdot \vec{u}$ by

$$\vec{Q}_i \cdot \vec{u} = \begin{cases} \phi_i - \varphi + 2\pi & (-\pi \leq \phi_i < -2\pi/3 \text{ and } \varphi > \phi_i + \pi) \\ \phi_i - \varphi - 2\pi & (2\pi/3 \leq \phi_i < \pi \text{ and } \varphi < \phi_i - \pi) \\ \phi_i - \varphi & (\text{otherwise}) \end{cases} . \tag{3.9}$$

In order to determine φ, we substitute the above results into ϕ_3,

$$\begin{aligned} \phi_3 &= \vec{Q}_3 \cdot \vec{u} + \varphi \\ &= -\vec{Q}_1 \cdot \vec{u} - \vec{Q}_2 \cdot \vec{u} + \varphi \\ &= -\phi_1 - \phi_2 + 3\varphi - 2\pi n \end{aligned} \tag{3.10}$$

with an integer n. The right-hand side is a one-to-one function of $\varphi \in [-\pi/3, \pi/3]$ with a range of 2π. Now, by taking the modulo of 2π, we can determine the value of φ using this expression from $\{\varphi_i\}$,

$$3\varphi \equiv \phi_1 + \phi_2 + \phi_3 \pmod{2\pi}. \tag{3.11}$$

Thus obtained φ is plotted in Fig. 3.7(a). The mean value of φ is 0.286, and the standard deviation is 0.32. This distribution is neither extremely sharp nor broad; it is not clear whether the cubic term is important or not.

We also plotted $\vec{u}$ as well in Fig. 3.7(b). The vector $\vec{u}$ is determined by the displacement of CDW maxima from an ideal lattice position. The origin of the ideal lattice is chosen arbitrary, and a vector from a center of a unit cell to a CDW maximum inside the unit cell (if exists) is drawn. The ideal lattice constant and the orientation of the lattice are calculated from the Fourier peaks corresponding to CDW maxima. Since it depends on our eyes to determine the center of the Fourier peaks, there might be a artificial overall drift in $\vec{u}$ over the size of the image due to the deviation from the exact lattice constant and the obtained lattice constant. If we ignore such a drift, the vector $\vec{u}$ changes very smoothly over the size of the picture.

3.3.4 Delaunay diagram

To analyze the appearance of topological defects such as dislocations more quantitatively, we study a Delaunay diagram [Murray et al. (1990); Grier et al. (1991); Dai and Lieber (1992, 1993); Chaikin and Lubensky (2000)] constructed from the CDW maxima in Fig. 3.2. Dislocations are characterized by the following line integral in a periodic media:

$$\oint d\vec{u} = \vec{b}, \tag{3.12}$$

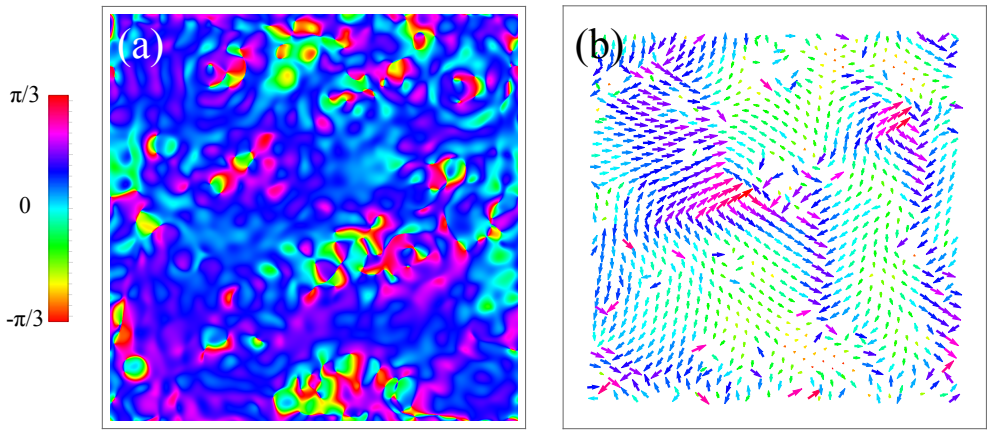

Figure 3.7: Total phase φ, and displacement vectors $\vec{u}$. Data was taken by C. Arguello, E. Rosenthal, and A. Pasupathy.

where $\vec{u}$ is the displacement vectors, and $\vec{b}$ is a Burgers vector. The path of the integral (Burgers circuit) is arbitrary as far as it encloses the position of the dislocation. An easy way of identifying dislocations is using a Delaunay digram, whose lines are the constant phase of the three CDWs. In order to construct a Delaunay diagram, first we divide the image such that each CDW maximum has a region inside which any point is closer to the CDW maximum than other CDW maxima. The boundary of two neighboring regions is a part of the bisection line of the neighboring CDW maxima (This is called a Voronoi diagram). For any two neighboring regions, we draw a line connecting the two CDW maxima inside. It is known that the any two dimensional image is filled by triangles given by these lines after these procedures. Thus it is called Delaunay triangulation. For detail procedures to extract the position of the CDW maxima is given in the Appendix. The obtained Delaunay diagram is given in Fig. 3.8.

Examples of dislocations near impurities are shown by the failure of some Burgers circuits (shown as broken lines) to close. Each dislocation consists of disclinations,

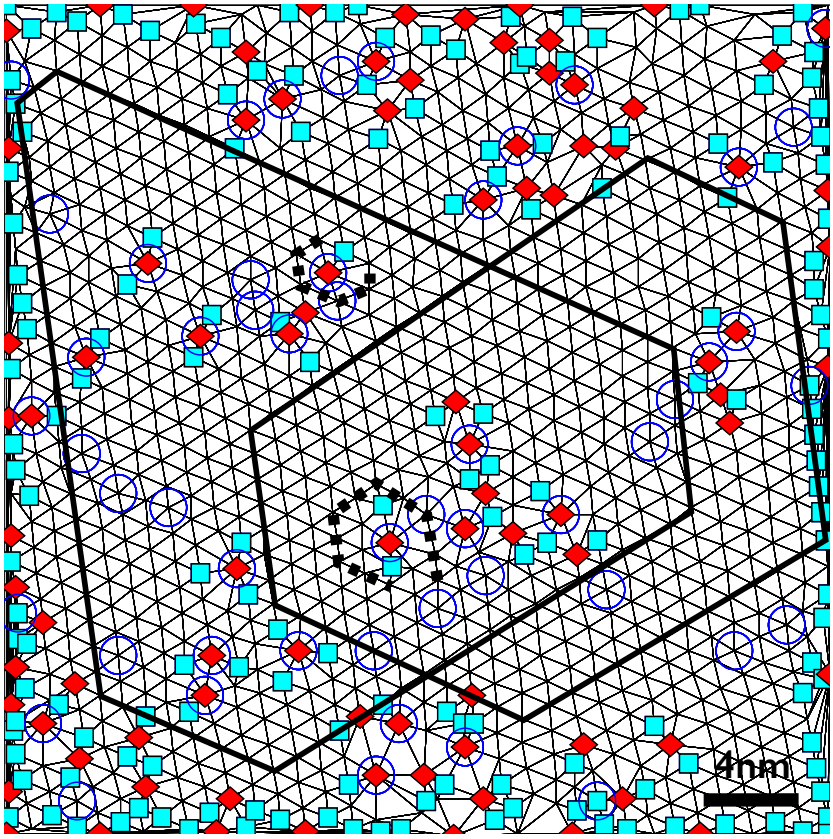

Figure 3.8: Delaunay diagram constructed from the topographic image (Fig. 3.2) [reproduced from Okamoto et al. (2014)]. Data was taken by C. Arguello, E. Rosenthal, and A. Pasupathy. The blue squares (red diamonds) are the vertices having fewer (more) than six edges. The blue circles indicate the locations of impurities. Solid lines are the Delaunay loops which do close, and dashed one are loops which do not close.

where a vertex has fewer (more) than six edges represented by blue squares (red diamonds). The locations of impurities are indicated by the blue circles. We find that dislocations are only visible on short length scales; in general loops of size larger than a few lattice constants (solid lines) close, indicating that in this field of view the dislocations appear only in bound dislocation-antidislocation pairs; this agrees with the observation in the phase of the order parameters. The loops continue to close

even if the size of the loop becomes as large as the image size, indicating that on the length scales accessible to this experiment, there are no free dislocations. Therefore, the system is in a Bragg glass phase [Feigel'man et al. (1989); Nattermann (1990); Bouchaud et al. (1991, 1992); Korshunov (1993); Giamarchi and Le Doussal (1994, 1995, 1997); Rosso and Giamarchi (2004)].

3.4 Analytical study of a Ginzburg-Landau model

In this section, we analyze a simplified Ginzburg-Landau model describing a CDW transition in Eq. (1.3). Although the distribution of φ in our data is not broad enough for us to ignore the cubic term in the Ginzburg-Landau model, it is known that the phase transition is second order [Harper and Geballe (1975); Moncton et al. (1977)] implying that the cubic term is negligible. Thus, for simplicity, we consider a CDW described by one phase variable ϕ, and further neglect amplitude modulation. We now add impurities at positions x_a; these impurities act to locally pin the phase to the values θ_a. In the original expression, we have $\theta_a = \vec{Q} \cdot \vec{x}_a$, although we simply assume that they are random variables irrelevant to their positions. At distances $|\vec{x} - \vec{x}_a| \gg \xi$ (ξ is the coherence length of the CDW) the phase will change; this may take place either by a smooth modulation (as shown in the right inset of Fig. 3.6) or by creation of a defect-antidefect pair (as shown in the left inset of Fig. 3.6). In the absence of defects the free energy of this phase only model is

$$F = \int d^3\vec{x} \rho_S \left(\vec{\nabla}\phi\right)^2 - |V| \sum_a \cos\left[\theta_a - \phi(\vec{x}_a)\right], \tag{3.13}$$

where ρ_S is the phase stiffness, x_a labels the positions of the impurities, θ_a is the phase energetically favored by the impurity at x_a (this depends on the position of the impurity), and V is the magnitude of the impurity potential (taken to be the same for

all impurities in light of the weak variation of amplitudes found in Fig. 3.2). We have rescaled lengths by the ratio of in-plane to out of plane coherence lengths. In a simple model, we expect that $\rho_S \sim f|\psi|^2\xi^2 \sim ft\xi^2$ with f a measure of the condensation energy per unit volume at $T = 0$, ψ the CDW amplitude, ξ a bare coherence length, and $t = (T_c - T)/T_c$ the reduced temperature, while $V \sim V_0\psi \sim V_0\sqrt{t}$ is proportional to a bare pinning potential V_0 and to the first power of the CDW amplitude. We assume the impurities are dilute (mean inter-impurity distance l much greater than CDW correlation length $\xi' = \xi/\sqrt{2t}$) [McMillan (1977); Weber et al. (2011)]; this condition breaks down close to the transition temperature, or for dense impurities.

Abe (1985, 1986) pointed out that when $\xi \ll l$ and pinning is strong the previously anticipated disordered state with many topological defects does not appear; he showed that a locally modulating state near impurities over the distance ξ has lower energy by a scaling argument. Then he assumed that the interaction between impurities is only nearest neighboring type when he simulated impurities put on a regular lattice. Although his scaling argument casts a serious doubt to the previously anticipated disordered state for strong pinning, the assumption of local interaction between impurities is not correct as we will discuss in the following. We obtained an analytical solution to the problem of impurities put on a regular lattice, and further confirm the basic features of the solution by Monte Carlo simulations.

3.4.1 Ground states

Minimization of Eq. (3.13) shows that ϕ obeys the Laplace equation, $\nabla^2\phi = 0$ for all $\vec{x}$ not within a distance ξ of an impurity site. The most general solution of the Laplace equation is

$$\phi(\vec{x}) = \sum_a \frac{\bar{\theta}_a \xi}{|\vec{x} - \vec{x}_a|}, \tag{3.14}$$

where the $\bar{\theta}_a$ are parameters and Eq. (3.14) applies only if $|\vec{x} - \vec{x}_a| > \xi$ for all a. For $|\vec{x} - \vec{x}_b| < \xi$ we regularize the formally divergent term in the sum as $\bar{\theta}_b$. To determine the parameters $\bar{\theta}_a$ we substitute Eq. (3.14) into Eq. (3.13) and minimize the result with respect to the $\bar{\theta}_a$. We focus here on the strong pinning limit, in which we expect that the phase $\phi(x \to x_a) \approx \bar{\theta}_a$, so we can expand the impurity potential up to second order. We find

$$\frac{E}{V} \simeq \frac{\epsilon}{2} \sum_{ab} K_{ab} \bar{\theta}_a \bar{\theta}_b + \frac{1}{2} \left(\theta_a - \sum_b K_{ab} \bar{\theta}_b + 2\pi n_a \right)^2 \tag{3.15}$$

with $K_{ab} \equiv \delta_{ab} + (1 - \delta_{ab})\, \xi / |\vec{x}_a - \vec{x}_b|$, and $\epsilon = 8\pi \rho_S \xi / V \ll 1$. The integer n_a takes care of the periodicity of the cosine potential. For a single impurity, $n_a \neq 0$ simply increases the elastic energy compared to $n_a = 0$. We expect that with many impurities, $n_a \neq 0$ solutions are energetically expensive most of the time. We will consider $n_a = 0$ until we will come back to this problem later. Eq. (3.15) is an analogue of a Coulomb gas with the constraint that the potential take specific values on particular sites. Minimizing the total energy in terms of $\bar{\theta}_a$, we find

$$\bar{\theta}_a = \sum_b (\epsilon I + K)^{-1}_{ab}\, \theta_b \equiv \sum_b J_{ab} \theta_b \tag{3.16}$$

where I is the identity matrix.

The key physics of Eqs. (3.14) and (3.15) is that because of the long ranged nature of the Laplacian problem, the phase at a given site is determined by the collective response at many impurity sites. To gain analytical insights into this physics we place the impurities on a cubic lattice with lattice constant l; the randomness enters only through the values of the parameters θ_a. Defining $\vec{p}$ to be a vector in the reciprocal lattice of the lattice of impurity positions, we find

$$K(p) = \frac{1}{r_{\mathrm{TF}}^2 p^2} + 1 \cdots, \tag{3.17}$$

where $\vec{p}$ lies within the Brillouin zone of the lattice of impurity positions and $\cdots$ denotes terms that are smaller by powers of ξ/l than the terms that have been retained. $r_{\rm TF} = \sqrt{l^3/4\pi\xi}$ is a characteristic screening length. Eq. (3.17) implies that J has the familiar screening form:

$$J(p) \simeq \frac{p^2 r_{\rm TF}^2}{p^2 r_{\rm TF}^2 + 1}. \tag{3.18}$$

Note that in Eq. (3.18) terms of $\mathcal{O}(\epsilon)$ have been neglected; these do not affect the basic screening properties. Abe considered a similar scenario but assumed a simple exponential form of $J(x)$ instead of the screening form given by Eq. (3.18) [Abe (1986)]. The total energy is now found to be

$$E = 4\pi\rho_S\xi \sum_{ab} J_{ab}\theta_a\theta_b. \tag{3.19}$$

The physics encoded bf Eqs. (3.17) and (3.18) is that that phase at any given site is determined collectively; thus even delta-correlated randomness $\langle\theta_a\theta_b\rangle \sim \delta_{ab}$ leads to phase parameters $\bar{\theta}$ with long ranged correlations while phase fluctuations are suppressed. Explicitly, use of Eqs. (3.16) and (3.18) leads to

$$\begin{aligned}\langle\phi(\vec{x})\phi(\vec{y})\rangle &= \sum_{ab} \frac{\langle\bar{\theta}_a\bar{\theta}_b\rangle}{|\vec{x}-\vec{x}_a||\vec{y}-\vec{x}_b|} \\ &\approx \frac{8\xi^2\pi^2}{3l^3}\int_0^{2\pi/l} dp \frac{p\sin\left(p\,|\vec{x}-\vec{y}|\right)}{|\vec{x}-\vec{y}|\left(p^2+\frac{4\pi\xi}{l^3}\right)^2},\end{aligned} \tag{3.20}$$

where we have written the result for a three dimensional model and, because we are interested in the long length scale behavior, we have approximated the Brillouin zone of the impurity lattice as a sphere of an appropriate radius.

We also numerically solved the matrix equation (3.16) without any simplifying assumptions by placing impurities at random on the nodes of a $L \times L \times L$ lattice of lattice constant ξ with randomly chosen preferred phases, and by calculating K

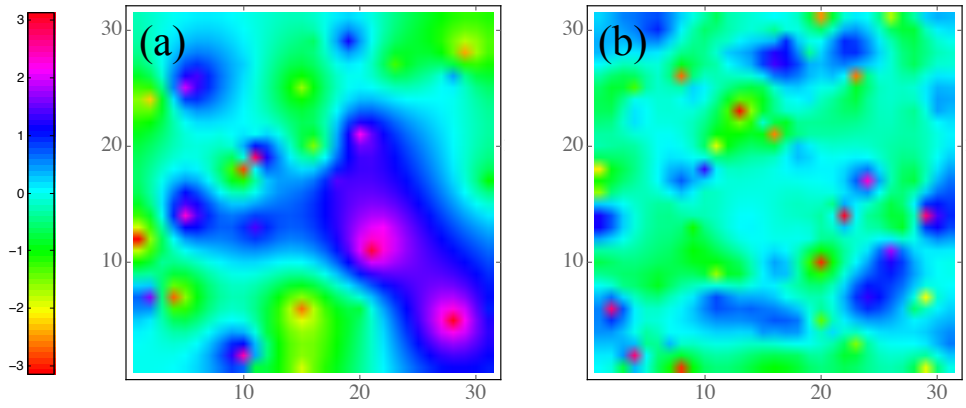

Figure 3.9: Solutions of Eq. (3.16) obtained by placing impurities randomly on sites of a cubic lattice of lattice constant ξ with phases chosen randomly in the interval $-\pi \leq \theta_a \leq \pi$. Typical phase configuration obtained for a system of linear system size $L = 31\xi$ with l chosen so the impurity density is $n_{\text{imp}} = 4\%$ in (a) two dimensions and (b) three dimensions. For the two dimensional case, we take $R = 2.5L$ in Eq. (3.21).

and J numerically. For two dimensional cases, instead of the Coulombic form of the kernel, we use a logarithmic form

$$K_{ab} = \delta_{ab} + (1 - \delta_{ab}) \log(R/|\vec{x}_a - \vec{x}_b|)/\log(R/\xi), \tag{3.21}$$

where R is an arbitrary constant. The choice of R does not affect our final result. The Fourier transform of this kernel is found to be

$$K(p) \sim 1 + \frac{2\pi}{p^2 l^2 \log(\frac{R}{\xi})}, \tag{3.22}$$

again leading to an infra-red convergent phase fluctuations; the long-range order is expected. Typical phase configurations are given in Fig. 3.9 for two and three dimensional cases. In both cases, the phase varies slowly at long length scales; the

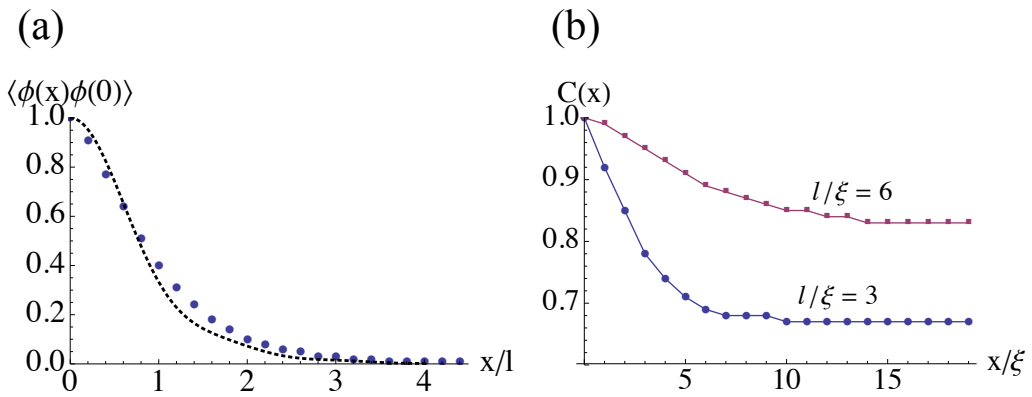

Figure 3.10: (a) Normalized phase-phase correlations obtained by averaging over 50 realizations of randomly placed impurities with $l = 5.0\xi$ and linear sample size $L = 60$. (b) Autocorrelations of the order parameter obtained for same conditions as (a).

two dimensional case, however, has more short length fluctuations (the exact amount depends on the detail of the ultra-violet cut-off). A further difference is that in two dimensions impurity-induced vortex-antivortex pairs ultimately lead to a power-law decay in the autocorrelation. We have also compared the analytical expression for the phase phase correlation [Eq. (3.20)] to the numerical result. A typical case is shown in Fig. 3.10(a) for $l = 5.0\xi$. In this case and in other cases we confirmed that the analytical expression agrees with the numerical one.

The screening form of Eq. (3.20) has an important consequence: by taking the $y \to x$ limit of Eq. (3.20) we see that the expression for the variance of the CDW phase $\langle \phi(\vec{x})^2 \rangle$ is infrared finite implying that the average of the CDW order parameter $\langle e^{i\phi} \rangle = e^{-\frac{1}{2}\langle \phi^2 \rangle}$ is non-zero, so that even in the presence of impurities the model has long ranged order. We have also confirmed this numerically; an example is shown in Fig. 3.10(b). The physics of this result is that the long-range nature of the elastic

forces means that the local constraints imposed by the pinning can be accommodated by small amplitude changes in the phase which accumulate over long distances.

We now turn to the question of local topological defects. Making a defect on one site a allows the phase to relax rapidly from the value preferred by the local impurity towards a background value determined by the other defects, decreasing the elastic free energy at the cost of driving the amplitude to zero over a correlation volume. We may estimate that the defect costs an energy $E_{\text{vortex}} \sim ft^2\xi^3/2 \sim f_0\sqrt{t}\xi_0^3/2 \sim \rho_S\xi$. The energy gain is associated with removing one defect from the elastic energy. Using the screened Coulombic form of K^{-1} and noting that the θ_a are random variables we obtain that the elastic energy gain is roughly

$$E_{\text{elastic}} \simeq 4\pi\rho_S\xi(1+\epsilon)^{-1}\theta_a^2 + \mathcal{O}(\xi/l). \tag{3.23}$$

Thus the energy cost of making a defect-antidefect pair is parametrically equal to the cost of the phase deformation and which one is preferred is determined by an intrinsic property of the CDW [namely the ratio $\kappa = 4\pi\rho_S\xi/E_{\text{vortex}}(1+\epsilon)$] and the square magnitude of the phase deviation caused by the impurity. Our finding that about 20% of impurities induce defects suggests that $\kappa \approx 0.16$, and that defects are only produced when the phase deviates by an amount near its maximal value ($\theta_a \approx \pi$); in analogy with superconductors, the system should be thought of as "type I" rather than "type II".

Lastly, before, we move on to the problem of fluctuations, we discuss the variations of n_a, which we have ignored so far. When $n_a \neq 0$ is allowed, the energy in Eq. (3.19) is generalized to

$$E = 4\pi\rho_S\xi\sum_{ab} J_{ab}(\theta_a + 2\pi n_a)(\theta_b + 2\pi n_b). \tag{3.24}$$

In order to see whether $n_a = 0$ solution is stable, we use a gradient method to search the lowest energy state in the $\{n_a\}$ space. We start from the original state with all

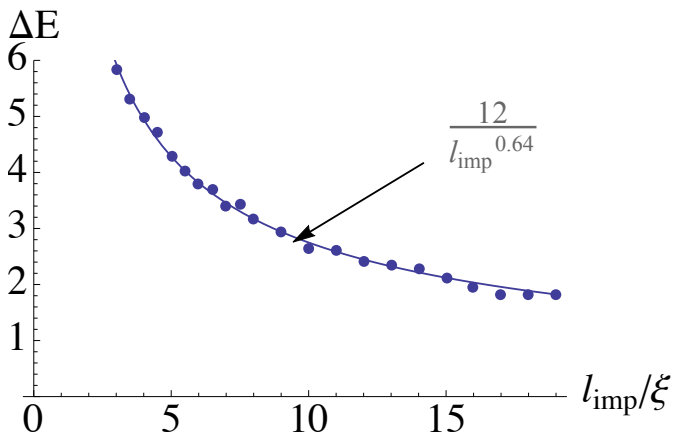

Figure 3.11: Average energy gain from n_a variation (in the unit of $4\pi\rho_S\xi$). Its dependence on the inter-impurity distance l is well fitted by $12/l^{0.64}$.

$n_a = 0$, and through all a we change $n_a \to n_a \pm 1$. If the change gives a lower energy, we accept it, and move onto the next a; otherwise, we do not update n_a. We repeat the procedures until we get a converged result. For 4% impurities with random or regular positions, about 5% to 10% of the impurities have nonzero $n_a = \pm 1$. We do not observe $|n_a|$ bigger than 1. We also tried initial states with randomly chosen $\{n_a\}$ from $\{-1, 0, 1\}$, while these do not evolve into new states. The average energy gain by a single change of n_a depends on the concentration of the impurities; it is well fitted by (Fig. 3.11)

$$\Delta E(l/\xi) \approx \frac{12.0}{(l/\xi)^{0.64}}, \tag{3.25}$$

in the unit of $4\pi\rho_S\xi$. Considering the number of $n_a \neq 0$, this is a significant change in total energy; the $n_a = 0$ solution is actually a high energy state. The change of n_a occurs mostly when θ_a is close to $\pm\pi$, while other impurities nearby prefer $\mp\pi$. As the number of impurities inside the sphere of radius r_{TF} grows as l increases, the fluctuation of local phase at the center of the sphere, which induces the change of n_a, decreases; thus, the energy gain by a single change of n_a also decreases as l becomes bigger.

Although the energy of the $n_a = 0$ solution is higher than the true ground state, the conclusion that the system is in long-range order does not change even the modification of n_a is allowed. For example, when we calculate the phase-phase correlation, now the average over the impurity phases is replaced to

$$\langle(\theta_a + 2\pi n_a)(\theta_b + 2\pi n_b)\rangle. \tag{3.26}$$

We find that autocorrelation of the n_a distribution decays almost immediately over the average inter-impurity distance l, indicating $\langle n_a n_b\rangle \propto \delta_{ab}$. Similarly the correlation between θ_a and n_a is found to be local. Thus, essentially the calculation leading to the long range order does not change.

3.4.2 Fluctuations

We now consider states that are not the ground state. These may be generated in two ways. One may consider states of the form of Eq. (3.14) but with parameters $\bar{\theta}_a$ that do not satisfy Eq. (3.16). These solutions will have very high energy, because they violate the pinning conditions. Alternatively, one may consider solutions $\phi(x)$ which correspond to elastic excitations about the ground state but with the pinning condition satisfied. To obtain such solutions we write

$$\phi(\vec{x}) = \Delta(\vec{x}) + \sum_a \frac{\bar{\theta}'_a \xi}{|\vec{x} - \vec{x}_a|}. \tag{3.27}$$

Δ does not obey the Laplace equation, because the configuration does not minimize the energy. The $\bar{\theta}'_a$ [whose dependence on $\Delta(x)$ is not explicitly notated here] are determined by minimizing the energy for fixed $\Delta(x)$, in particular insuring that the impurity pinning condition is fulfilled. Substituting Eq. (3.27) into Eq. (3.13) we

obtain

$$E[\Delta(x)] \simeq \rho_S \int d^3x \, (\nabla\Delta)^2 + \frac{V}{2}\sum_a (\Theta_a - \sum_b K_{ab}\bar{\theta}'_b)^2 + 4\pi\rho_S\xi\left[\sum_{ab} K_{ab}\bar{\theta}'_a\bar{\theta}'_b + 2\sum_a(\Delta_a - \Delta_0)\bar{\theta}'_a\right], \quad (3.28)$$

where $\Delta_a = \Delta(x = x_a)$ and Θ_a is the sawtooth function of $(\theta_a - \Delta_a)$ introduced to recover the periodicity 2π, and taken to be in $[-\pi, \pi]$. Δ_0 is the value of Δ at infinity. Minimizing Eq. (3.28) with respect to the $\bar{\theta}'_a$ gives,

$$\bar{\theta}'_a = \sum_b J_{ab}\Theta_b, \quad (3.29)$$

and substituting this into Eq. (3.28) leads to (noting that terms of order ϵ and the multi branch structure of the sawtooth function are not important here)

$$E[\Delta(x)] = \rho_S\left[\int d^3x \, (\nabla\Delta)^2 - 4\pi\xi\sum_{ab} J_{ab}\Delta_a\Delta_b\right] + \text{const.} \quad (3.30)$$

To analyze Eq. (3.30), we again consider the model in which the impurities are on a regular lattice of lattice constant l and use Eq. (3.18) for the Fourier transform of J_{ab}, obtaining finally

$$E = \rho_S \int \frac{d^3p}{(2\pi)^3}\frac{r_{\rm TF}^2 p^4}{r_{\rm TF}^2 p^2 + 1}|\Delta(p)|^2. \quad (3.31)$$

Since this is a positive definite, the ground state must have $\Delta(p \neq 0) = 0$; long-range order is preserved. The thermal fluctuation is

$$\delta\phi \equiv \phi - \sum_a \frac{\bar{\theta}_a\xi}{|\vec{x} - \vec{x}_a|}, \quad (3.32)$$

where the second part is the ground state configuration with $\bar{\theta}_a$ given by Eq. (3.16). The phase-phase correlation of the fluctuating part $\delta\phi$ is found to be

$$\langle \delta\phi(\vec{x})\delta\phi(0)\rangle \sim \frac{T}{\rho_S}\int \frac{d\vec{p}}{(2\pi)^3} e^{i\vec{p}\cdot\vec{x}} \frac{r_{\rm TF}^2}{p^2 r_{\rm TF}^2 + 1}. \tag{3.33}$$

This function decays exponentially in terms of $\vec{x}$, and, thus, the long-range order still survives. This means that the fluctuation is massive, and that the static conductivity is vanishing at $T = 0$ if we ignore the quantum fluctuations. The finite energy to excite the fluctuation originates from the fact that impurities fix the fluctuations at impurity sites to zero, $\delta\phi(x_a) = 0$.

There is also a possibility of phase slips where n_a varies. Since there is an infinitely large energy barrier between different n_a's, this could happen only as a soliton type transition. In the Monte Carlo simulation below, we do not necessarily change the phase adiabatically (especially for the overrelaxation steps), thus the transition may happen in principle, although the probability would be very small.

3.5 Monte Carlo simulation of the phase model

In this section, we use a Monte Carlo simulation to simulate the phase only model of Eq. (3.13) to verify the previous analysis. Once discretized, the phase only model is formally equivalent to the XY model with random magnetic fields:

$$E = -\sum_{\langle i,j\rangle} \vec{s}_i \cdot \vec{s}_j - \sum_{i\in\{a\}} \vec{h}_i \cdot \vec{s}_i, \tag{3.34}$$

with adjacent sites $\langle i, j\rangle$, random impurity sites $\{a\}$, and unit vectors $\vec{s}_i$. We measure the energy by the ferromagnetic coupling J between neighboring spins. The phase of the CDW maps to the angle of planer spin, and the potential term maps to the

linear coupling of the spin and a local magnetic field. Now θ_a is the angle which the magnetic field prefers at a site a. Thus, we consider the XY model with random fields in the following. First, we briefly explain the methodology of Monte Carlo simulations, and then show our results. We find that a system size dependence of the autocorrelation follows a power-law behavior, whose exponent is different from the one of the previously studied Bragg glass phase.

There are several relevant Monte Carlo simulations for the three dimensional XY model with random magnetic fields. Gingras and Huse (1996) studied a XY model with random magnetic fields applying on all sites. Their findings suggest vanishing of vortices at weak magnetic fields at low temperatures. Fisch considered $q = 6$ and 12 Potts models with dilute, but infinitely strong magnetic fields, and found long-range order at low temperatures and quasi-long-range order at intermediate temperatures for $n_{\rm imp} = 6.25\%$ [Fisch (1997)].

3.5.1 Method

The basic spirit of Monte Carlo simulation is to calculate an integral by sampling. In condensed matter physics, what we want to know are observables averaged over many thermal configurations:

$$\langle \mathcal{O}[\phi] \rangle = \frac{\int \mathcal{D}\phi e^{-\beta E[\phi]} \mathcal{O}[\phi]}{\mathcal{Z}}, \tag{3.35}$$

where ϕ represents the degrees of freedom in the system, and $\beta = 1/T$ is the inverse temperature. The most naive way of evaluating this integral is to randomly pick up N points in the phase space corresponding to various configuration of the field ϕ, and

then to take the ensemble average of the integrand,

$$\langle \mathcal{O}[\phi] \rangle \simeq \frac{1}{N} \sum_{i=1}^{N} e^{-\beta E_i} \mathcal{O}[\phi_i], \tag{3.36}$$

where ϕ_i is the field configuration of the ith sample, and E_i is the energy. However, the drawback of this method is that we sample many points that do not contribute to the integral much; many configurations are exponentially small due to the exponential factor. Thus, the evaluation of the integral takes much longer time than the one that we show below, and we will not use this approach.

To make the evaluation faster, we need to sample phase space more efficiently, in a sense that we can sample more points that contribute of the order of 1. In order to achieve this goal, we use a weighted sampling instead of uniform sampling. The basic idea is to generate N sample points $\{\phi_i\}$ in the phase space, whose energy distribution follows the Boltzmann distribution approximately,

$$\frac{\text{Number of samples having } E_i}{N} \propto e^{-\beta E_i}. \tag{3.37}$$

Then, the observable quantity can be evaluated as

$$\langle \mathcal{O}[\phi] \rangle \simeq \frac{1}{N} \sum_{i=1}^{N} \mathcal{O}[\phi_i] \tag{3.38}$$

without any exponential factor. Since there are more sample points for lower energies, whose contributions are of the order of unity, this converges much faster than the uniform sampling in the previous paragraph.

Now the problem is how to generate such a sample following the Boltzmann distribution. The most common way is to use a Markov process. Now let us label the all possible configurations of the system as $\{\chi_1, \ldots, \chi_\nu\}$, where ν is the total number of configurations. In a Markov process, the next state ϕ_{i+1} is determined from the

last state ϕ_i based on a given probability matrix $P(\chi_\alpha \to \chi_\beta)$, which is a probability where we have $\phi_{i+1} = \chi_\beta$ if $\phi_i = \chi_\alpha$. Conservation of probability flow requires that this matrix should satisfy

$$\sum_{\beta=1}^{\nu} P(\chi_\alpha \to \chi_\beta) = 1. \tag{3.39}$$

Suppose that $\vec{\rho}_i$ is a vector whose ι component is the probability of having χ_ι at ith step. This is given by simply multiplying the probability matrix i times to the initial distribution,

$$\vec{\rho}_i = P^i \vec{\rho}_0. \tag{3.40}$$

Since the probability matrix is non-negative, from Perron-Frobenius theorem, the maximal eigenvalue is 1, and all the eigenvalues are positive. This means after many steps, $\vec{\rho}_i$ converges to the eigenvector with eigenvalue 1, $\vec{\omega}$:

$$\vec{\omega} = P\vec{\omega}. \tag{3.41}$$

This equation is called a detailed balance. Now, we would like to choose P such that $\vec{\omega}$ follows the Boltzmann distribution,

$$\omega_\iota \propto e^{-\beta E[\chi_\iota]}. \tag{3.42}$$

If we can make such P, we can use the Markov process to generate the desired sample after convergence.

There are many ways to choose P satisfying the detail balance. The most common one is the Metropolis-Hasting algorithm. The key steps to generate the sample is as follows:

1. Choose the initial state $\phi_0 = \chi_\alpha$ in the phase space.

2. Choose the next state χ_β as a next candidate.

3. Accept χ_β as ϕ_1 with a probability min $\left[1, \frac{\omega_\beta}{\omega_\alpha}\right]$. If not accepted, keep $\phi_1 = \chi_\alpha$.

4. Repeat process 2 and 3 to get $i \geq 1$.

In our simulation we choose a candidate such that the acceptance rate is 40% to 60%.

We also employ the overrelaxation steps to get a faster convergence. In this method, the candidate state is chosen from the state with exactly the same energy as the last state, so that the acceptance rate is always 1. In our case, each spin is coupled to six spins as

$$\vec{s}_i \cdot \sum_{j \in \mathrm{NN}} \vec{s}_j \equiv \vec{s}_i \cdot \vec{H}_i. \tag{3.43}$$

Thus as a candidate state, using $\hat{H}_i = \vec{H}_i/|\vec{H}_i|$, we consider $\vec{s'}$ such that

$$\vec{s'} = -\vec{s} + 2(\vec{s} \cdot \hat{H}_i)\hat{H}_i. \tag{3.44}$$

$\vec{s'}$ is the vector having the same angle from $\vec{H}$ as $\vec{s}$, although in the opposite side. In other words, it is a reflection of $\vec{s}$ about $\vec{H}$. In this manner, the candidate state has the same energy as the last state of the Markov process. However, if we only use this method, the energy remains the same value forever; there is no ergodicity. Thus, we combine the Metropolis-Hasting algorithm, and the overrelaxation steps, to get a faster convergence with ergodicity.

3.5.2 Results

We simulate the XY model in Eq. (3.34) on a regular periodic lattice in three dimensions. We consider the $h_i = \infty$ limit, and the orientations of $\vec{h}_i$ are randomly chosen from $[-\pi, \pi]$. During the MC steps, we do not update the spins on impurity sites. We will count eight overrelaxation steps and two Metropolis steps as one MC step [Li and Teitel (1989)]. First 2×10^3 MC steps are used for thermalization, and

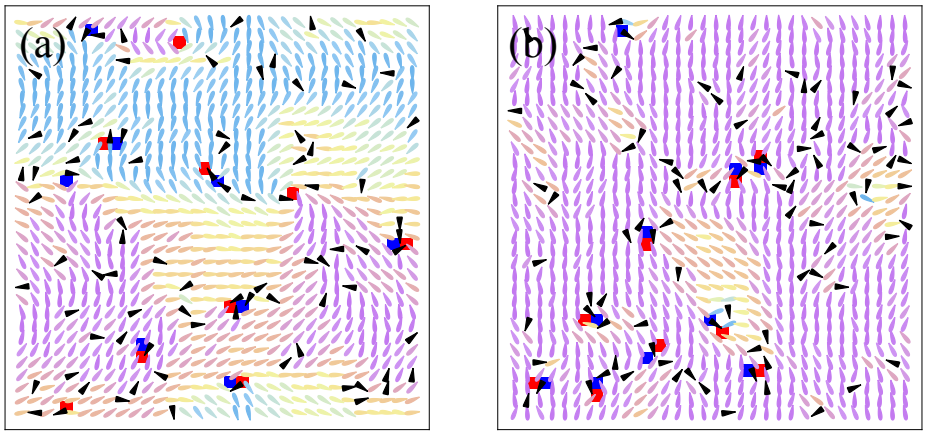

Figure 3.12: Typical phase configurations in (a) a metastable state and (b) a lowest energy state at $L = 48$, $T = 0.1$, and $n_{\text{imp}} = 8\%$.

the following 1×10^4 MC steps are used for measurements. We recorded observables every 25 MC steps. Using a cluster machine in our group with one node, it takes five to seven days to finish a calculation for $L = 128$. The autocorrelation time is at most 10 MC steps regardless of the size and temperatures; it is relatively short due to the overrelaxation steps. The range of the acceptance rate for Metropolis steps is from 40% to 60%. The physical observables are energy densities, specific heat, magnetization, magnetic susceptibility, vortex densities (the average number of vortex per plaquette), spin stiffness, and autocorrelations. In particular, the autocorrelations are defined as

$$C(\vec{x}) \equiv \langle \vec{s}(\vec{y} + \vec{x}) \cdot \vec{s}(\vec{y}) \rangle. \tag{3.45}$$

We used both "hot" (fully disordered) and "cold" (fully ordered) initial conditions. They both converge to a same statistical configurations with positive stiffness for small systems, $L = 16$. For a larger system with impurities, a cold (hot) state still converges to a state with a positive stiffness at low (high) temperatures, while it

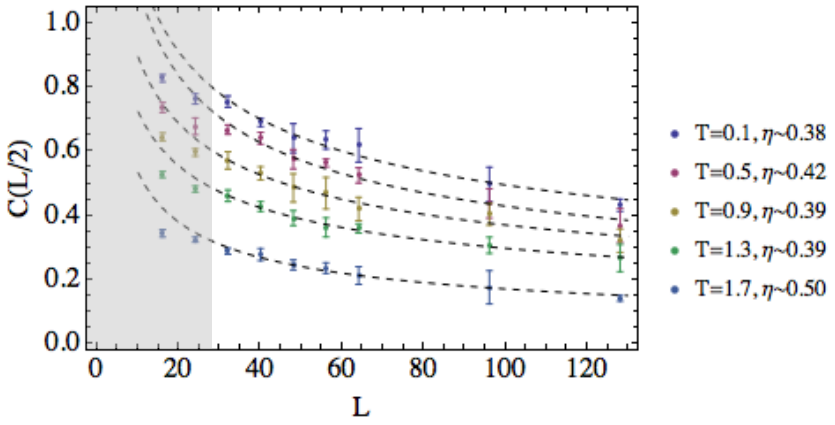

Figure 3.13: Size dependence of autocorrelations at $n_{\text{imp}} = 4\%$ at various temperatures. Only the data for $L \geq 32$ is used for fitting; the data with $L = 16$ and $L = 24$ indicated by the gray area are excluded for fitting due to their small sizes.

often goes to a metastable minimum at high (low) temperatures and remains there even after 10^4 MC steps. These metastable minima are characterized by a slightly higher energy, and a faster decay of autocorrelations by phase variations. In Fig. 3.12, we depict typical phase configurations at $n_{\text{imp}} = 8\%$ and $T = 0.1$ for a disordered metastable state and an ordered state. Vortices appear mostly near the impurity sites, and the densities of vortices are more or less the same for two cases $\sim 1.5\%$. In the ground state, except one vortex, only vortex-antivortex pairs are found, while there are more isolated vortices in the metastable state leading to the faster decay of the autocorrelation. The metastable configurations are relevant to experimental situations, which usually start from hot initial conditions.

At the transition temperature, we find peaks in the specific heat and magnetic susceptibility, while they are smeared out compared to the ones for clean samples. Above T_c, the number of topological defects increases, and at the same time, the stiffness goes to zero as expected. Due to the finite size, it is not clear whether the transition remains sharp in dirty samples.

In a Bragg glass phase, the autocorrelation decays by a power-law. In our Monte Carlo simulations, this may appear as the power-law size dependence of the autocorrelations and magnetization [Binder and Heermann (2010)],

$$C(L/2) \sim L^{-\eta}, \quad M(L) \sim L^{-\frac{\eta}{2}}. \tag{3.46}$$

If the system is in true long-range order, there is very little size dependence as far as the system size is large enough. We plotted $C(L/2)$ in Fig. 3.13 at various temperatures at $n_{\rm imp} = 4\%$. For each impurity configuration, the autoccorelations averaged over three directions are obtained, and then five different samples are used to calculate the average and the standard deviations in Fig. 3.13 [1]. To obtain η, we fit the data with $L \geq 32$ by power law function; in the log-log plot, the data at $L = 16$ and 24 deviates from the linear behavior due to their small size. We find that well below $T_c \approx 1.9$, the size dependence shows a power-law behavior with an exponent $\eta \approx 0.4$. Close to the transition, $T = 1.7$, the exponent increases to $\eta \approx 0.5$. Similar size dependence are checked on magnetization with negligible difference on the values of $\eta(T)$. Therefore, up to the size available for our simulations, the low-temperature phase is a quasi-long-range ordered phase with a low density of topological defects, i.e., a Bragg glass. The difference from the conventional Bragg glass phase with weak disorder [Giamarchi and Le Doussal (1994, 1995)] is that the exponent we find $\eta \sim 0.4$ is much smaller than the exponent $\eta_{\rm BG} \sim 1.0$ corresponding to a weakly disordered XY model. However, the exponent is almost independent of temperature as the conventional one. The apparent power-law decay in the autocorrelations is thus inconsistent with the conventional Bragg glass behavior about the exponent, and also with our previous analytical solutions giving a long-range order. Since our simulations are limited to relatively small lattice sizes, it is not certain whether the

[1] For $L = 128$ at $T = 1.7$, we have only two samples.

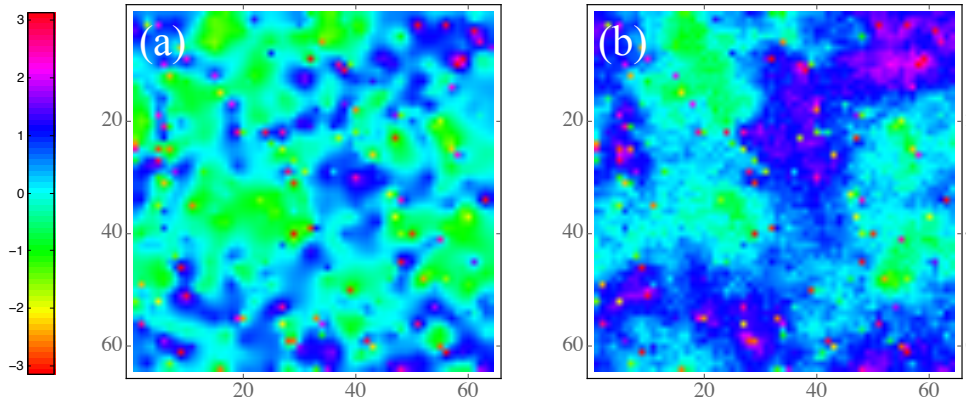

Figure 3.14: Phase profiles with the same impurity configurations given by (a) analytical expressions in Eq. (3.16), and (b) Monte Carlo simulations.

autocorrelations would saturate if the system size would be bigger. This should be checked in the future.

Lastly, we compare our analytical solution in Sec. 3.4, and our Monte Carlo simulations starting from the cold initial condition. In Fig. 3.14, we depict phase configurations obtained by these two different methods for the same impurity distribution with $L = 64$. The analytical solution has phase fluctuations at small length scales, while the Monte Carlo simulation has a larger scale phase variation. In the latter, larger amount of vortex-antivortex pairs in the vicinity of impurities are found, which seem to relax the large strain for some impurities preferring different phases from the local background phase. The different phase profiles lead to different size dependences in autocorrelations (Fig. 3.15). The autocorrelations from the analytical solutions are independent of the sizes as expected, while the ones from Monte Carlo simulations shows a power-law dependence as in Fig. 3.13.

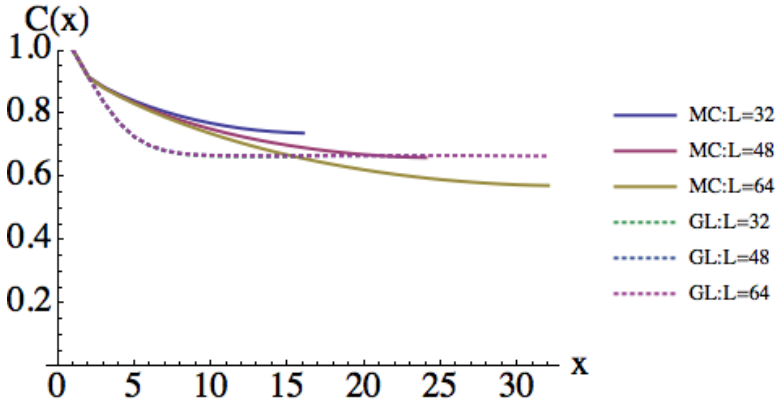

Figure 3.15: Autocorrelations given by analytical expressions in Eq. (3.16), and Monte Carlo simulations. Five samples are used for the disorder average.

3.6 Conclusions

In this chapter, we investigated the effects of impurity on the charge-density wave in $NbSe_2$. We analyzed a topographic image of the surface of the sample obtained by STM in detail, and found that the impurities on the material is dilute in a sense that the CDW periodicity is much shorter than the average inter-impurity distance, but also strongly pinning. Contrary to the conventional wisdom, predicting a proliferation of topological defects and destruction of long-range order for such a situation, the observed phase is found to be in a Bragg glass phase, where topological defects are always in dislocation-antidislocation pairs (Fig. 3.8).

In order to understand such a unconventional behavior, we studied a Ginzburg-Landau model with impurities. First, noting that a single impurity makes a Coulombic phase modulation, and assuming that the impurities are put on a periodic lattice, we solved the model analytically. We found that the ground state is in a long-range ordered state, and furthermore, the excitations that we can think of require a finite and large energy; the ground state is very stable. We also checked the solution basically does not change even we put the impurities on random positions by solving the

problem numerically (Fig. 3.9).

In order to confirm the above picture, and further study the effects of topological defects, we implemented Monte Carlo simulations of a similar model on a discrete lattice. At low temperatures, autocorrelations do not decay exponentially, but remain finite. However, they also show a power-law system size dependence, indicating that the system is in a Bragg glass phase. The power-law exponent is ~ 0.4, which is much smaller than the previously obtained value ~ 1.0, and is temperature independent. Investigating bigger systems is highly desirable to check whether the power-law decay persists or saturates.

While the two analyses both show unexpectedly (quasi-) long-range order, their size dependences of autocorrelations do not agree with each other. Correspondingly, the phase profiles calculated with the same impurity configurations, but by the two different methods differ qualitatively; in particular there are more vortex-antivortex pairs in the Monte Carlo simulations. Clarifying how such a difference in the phase configurations leads to the difference in the autocorrelations is an important future problem.

Bibliography

Abe, S., Impurity-Induced Pinning, Damping and Metastability of Interchain-Coupled Charge Density Waves, J. Phys. Soc. Japan **54**, 3494 (1985).

Abe, S., Numerical Experiments on Glassy Charge Density waves, J. Phys. Soc. Japan **55**, 1987 (1986).

Affleck, I., Kennedy, T., Lieb, E. and Tasaki, H., Rigorous Results on Valence-Bond ground states in antiferromagnets, Phys. Rev. Lett. **59**, 799 (1987).

Ahn, J. R. and Yeom, H. W., Metal-Insulator Transition in Au Atomic Chains on Si with Two Proximal Bands, Phys. Rev. Lett. **91**, 196403 (2003).

Allender, D., Bray, J. and Bardeen, J., Theory of fluctuation superconductivity from electron-phonon interactions in pseudo-one-dimensional systems, Phys. Rev. B **9**, 119 (1974).

Arguello, C. J., Chockalingam, S. P., Rosenthal, E. P., Zhao, L., Gutiérrez, C., Kang, J. H., Chung, W. C., Fernandes, R. M., Jia, S., Millis, A. J., Cava, R. J. and Pasupathy, A. N., Visualizing the charge density wave transition in 2H-$NbSe_2$ in real space, Phys. Rev. B **89**, 235115 (2014).

Aryasetiawan, F., Karlsson, K., Jepsen, O. and Schönberger, U., Calculations of Hubbard U from first-principles, Phys. Rev. B **74**, 125106 (2006).

Assaraf, R., Azaria, P., Boulat, E., Caffarel, M. and Lecheminant, P., Dynamical Symmetry Enlargement versus Spin-Charge Decoupling in the One-Dimensional SU(4) Hubbard Model, Phys. Rev. Lett. **93**, 16407 (2004).

Assaraf, R., Azaria, P., Caffarel, M. and Lecheminant, P., Metal-insulator transition in the one-dimensional SU(N) Hubbard model, Phys. Rev. B **60**, 2299 (1999).

Auerbach, A., *Interacting Electrons and Quantum Magnetism*, Graduate Texts in Contemporary Physics, Springer New York (1994).

Azaria, P., Gogolin, A., Lecheminant, P. and Nersesyan, A., One-Dimensional SU(4) Spin-Orbital Model: A Low-Energy Effective Theory, Phys. Rev. Lett. **83**, 624 (1999).

Bak, P. and Brazovsky, S., Theory of quasi-one-dimensional conductors: Interaction between chains and impurity effects, Phys. Rev. B **17**, 3154 (1978).

Balents, L., Bouchaud, J. and Mézard, M., The Large Scale Energy Landscape of Randomly Pinned Objects, J. Phys. I **6**, 1007 (1996).

Balents, L. and Fisher, D. S., Large-N expansion of $(4-\epsilon)$-dimensional oriented manifolds in random media, Phys. Rev. B **48**, 5949 (1993).

Balents, L. and Fisher, M., Weak-coupling phase diagram of the two-chain Hubbard model., Phys. Rev. B **53**, 12133 (1996).

Bardeen, J., Cooper, L. and Schrieffer, J., MIcroscopic Theory of Superconductivity, Phys. Rev. **108**, 1175 (1957).

Barth, J. V., Costantini, G. and Kern, K., Engineering atomic and molecular nanostructures at surfaces., Nature **437**, 671 (2005).

Binder, K. and Heermann, D., *Monte Carlo Simulation in Statistical Physics: An Introduction*, Graduate Texts in Physics, Springer Berlin Heidelberg (2010).

Binnig, G., Rohrer, H., Gerber, C. and Weibel, E., Surface Studies by Scanning Tunneling Microscopy, Phys. Rev. Lett. **49**, 57 (1982).

Bouchaud, J., Mézard, M. and Yedidia, J., Variational Theory for Disordered Vortex Lattices, Phys. Rev. Lett. **67**, 3840 (1991).

Bouchaud, J., Mézard, M. and Yedidia, J., Variational theory for the pinning of vortex lattices by impurities, Phys. Rev. B **46**, 14686 (1992).

Boulat, E., Azaria, P. and Lecheminant, P., Duality approach to one-dimensional degenerate electronic systems, Nucl. Phys. B **822**, 367 (2009).

Bunder, J. and Lin, H.-H., Dynamical symmetry enlargement in metallic zigzag carbon nanotubes, Phys. Rev. B **75**, 075418 (2007).

Calandra, M., Mazin, I. I. and Mauri, F., Effect of dimensionality on the charge-density wave in few-layer 2H-$NbSe_2$, Phys. Rev. B **80**, 241108 (2009).

Cardy, J., *Scaling and Renormalization in Statistical Physics*, Cambridge Lecture Notes in Physics, Cambridge University Press (1996).

Carpentier, D. and Orignac, E., Superconducting instability in three-band metallic nanotubes, Phys. Rev. B **74**, 085409 (2006).

Chaikin, P. M. and Lubensky, T. C., *Principles of Condensed Matter Physics*, Cambridge University Press (2000).

Chan, S. K. and Heine, V., Spin density wave and soft phonon mode from nesting Fermi surfaces, J. Phys. F: Met. Phys. **3**, 795 (1973).

Chen, C. J., *Introduction to scanning tunneling microscopy*, Monographs on the physics and chemistry of materials, Oxford University Press (2008).

Chen, W., Chang, M.-S., Lin, H.-H., Chang, D. and Mou, C.-Y., Potential flow of renormalization group in quasi-one-dimensional systems, Phys. Rev. B **70**, 205413 (2004).

Chudzinski, P., Gabay, M. and Giamarchi, T., Orbital current patterns in doped two-leg Cu-O Hubbard ladders, Phys. Rev. B **78**, 075124 (2008).

Coleman, S., There are no Goldstone bosons in two dimensions, Commun. Math. Phys. **264**, 259 (1973).

Controzzi, D. and Tsvelik, A., Excitation spectrum of doped two-leg ladders: A field theory analysis, Phys. Rev. B **72**, 035110 (2005).

Cyrot, M. and Lyon-Caen, C., Orbital superlattice in the degenerate Hubbard model, J. Phys. **36**, 253 (1975).

Dagotto, E., Hotta, T. and Moreo, A., Colossal Magnetoresistant Materials: The Key Role of Phase Separation, Phys. Rep. **344**, 1 (2001).

Dai, H. and Lieber, C., Solid-Hexatic-Liquid Phases in Two-Dimensional Charge-Density Waves, Phys. Rev. Lett. **69**, 1576 (1992).

Dai, H. and Lieber, C., Charge Density Dave Pinning and Disorder in Two Dimensions, J. Phys. Chem. **97**, 2362 (1993).

Delft, J. V. and Schoeller, H., Bosonization for Beginners - Refermionization for Experts, Ann. Phys. **7**, 225 (1998).

Dordevic, S., Basov, D., Dynes, R. and Bucher, E., Anisotropic electrodynamics of layered metal 2H-$NbSe_2$, Phys. Rev. B **64**, 161103 (2001).

Dove, M. T., *Introduction to Lattice Dynamics*, Cambridge Topics in Mineral Physics and Chemistry, Cambridge University Press (1993).

Efetov, K. and Larkin, A., Charge-density wave in a random potential, Sov. Phys. JETP **45**, 1236 (1977).

Fabrizio, M., Parola, A. and Tosatti, E., Strong-coupling phases of two Hubbard chains with interchain hopping, Phys. Rev. B **46**, 3159 (1992).

Feigel'man, M., Geshkenbein, V., Larkin, A. and Vinokur, V., Theory of Collective Flux Creep, Phys. Rev. Lett. **63**, 2303 (1989).

Finkel'stein, A. and Larkin, A., Two coupled chains with Tomonaga-Luttinger interactions, Phys. Rev. B **47**, 10461 (1993).

Fisch, R., Power-law correlated phase in random-field XY models and randomly pinned charge-density waves, Phys. Rev. B **55**, 8211 (1997).

Fröhlich, H., Electrons in Lattice Fields, Adv. Phys. **3**, 325 (1954).

Fujimoto, S. and Kawakami, N., Bosonization Approach to the One-Dimensional Kondo Lattice Model, J. Phys. Soc. Japan **63**, 4322 (1994).

Fukuyama, H. and Lee, P., Dynamics of the charge-density wave. I. Impurity pinning in a single chain, Phys. Rev. B **17**, 535 (1978).

Giamarchi, T., *Quantum Physics in One Dimension*, International Series of Monographs on Physics, Clarendon Press (2003).

Giamarchi, T., Disordered elastic media, in Encyclopedia of Complexity and Systems Science, pp. 2019–2038 (2009).

Giamarchi, T. and Le Doussal, P., Elastic Theory of Pinned Flux Lattices, Phys. Rev. Lett. **72**, 1530 (1994).

Giamarchi, T. and Le Doussal, P., Elastic theory of flux lattices in the presence of weak disorder, Phys. Rev. B **52**, 1242 (1995).

Giamarchi, T. and Le Doussal, P., Phase diagrams of flux lattices with disorder, Phys. Rev. B **55**, 6577 (1997).

Gill, W. and Scalapino, D., Monte Carlo study of a one-dimensional degenerate Hubbard model, Phys. Rev. B **35**, 215 (1987).

Gingras, M. and Huse, D., Topological defects in the random-field XY model and the pinned vortex lattice to vortex glass transition in type-II superconductors., Phys. Rev. B **53**, 15193 (1996).

Gogolin, A. O., Nersesyan, A. A. and Tsvelik, A. M., *Bosonization and Strongly Correlated Systems*, Cambridge University Press (2004).

Grier, D., Murray, C. and Bolle, C., Translational and Bond-Orientational Order in the Vortex Lattice of the High-T_c Superconductor $Bi_{2.1}Sr_{1.9}Ca_{0.9}Cu_2O_{8+\delta}$, Phys. Rev. Lett. **66**, 2270 (1991).

Gross, D. and Neveu, A., Dynamical symmetry breaking in asymptotically free field theories, Phys. Rev. D **10**, 3235 (1974).

Grüner, G., The dynamics of charge-density waves, Rev. Mod. Phys. **60**, 1129 (1988).

Grüner, G., *Density Waves In Solids*, Frontiers in Physics Series, Westview Press (2009).

Halperin, B. and Rice, T., Possible Anomalies at a Semimetal-Semiconductor Transition, Rev. Mod. Phys. **40**, 755 (1968).

Halperin, B. and Rice, T., The Excitonic State at the Semiconductor- Semimetal Transition, Solid State Phys. **21**, 115 (1968).

Hamers, R., Atomic-resolution surface spectroscopy with teh scanning tunneling microscope, Annu. Rev. Phys. Chem. **40**, 531 (1989).

Harper, J. and Geballe, T., Heat capacity of 2H-$NbSe_2$ at the charge density wave transition, Phys. Lett. A **54**, 27 (1975).

Himpsel, F., Altmann, K., Bennewitz, R., Crain, J., Kirakosian, A., Lin, J.-L. and McChesney, J., One-dimensional electronic states at surfaces, J. Phys. Condens. Matter **13**, 11097 (2001).

Hohenberg, P., Existence of Long-Range Order in One and Two Dimensions, Phys. Rev. **158**, 383 (1967).

Imry, Y. and Ma, S., Random-Field Instability of the Ordered State of Continuous Symmetry, Phys. Rev. Lett. **35**, 1399 (1975).

Jérome, D. and Schulz, H., Organic conductors and superconductors, Adv. Phys. **31**, 293 (1982).

Johannes, M. and Mazin, I., Fermi surface nesting and the origin of charge density waves in metals, Phys. Rev. B **77**, 165135 (2008).

Khveshchenko, D. and Rice, T., Spin-gap fixed points in the double-chain problem, Phys. Rev. B **50**, 252 (1994).

Kim, E., Fáth, G., Sólyom, J. and Scalapino, D., Phase transitions between topologically distinct gapped phases in isotropic spin ladders, Phys. Rev. B **62**, 14965 (2000).

Konik, R., Saleur, H. and Ludwig, A., Interplay of the scaling limit and the renormalization group:âĂĆâĂĆImplications for symmetry restoration, Phys. Rev. B **66**, 075105 (2002).

Korshunov, S., Replica symmetry breaking in vortex glasses, Phys. Rev. B **48**, 3969 (1993).

Kosterlitz, J. M. and Thouless, D. J., Ordering, metastability and phase transitions in two-dimensional systems, J. Phys. C Solid State Phys. **6**, 1181 (1973).

Kramers, H. and Wannier, G., Statistics of the Two-Dimensional ferromagnet. Part I, Phys. Rev. **60**, 252 (1941).

Kugel, K. I. and Khomskii, D. I., Superexchange Ordering of Degenerate Drbitals and Magnetic Structure of Dielectrics with Jahn-Teller Ions, JETP Lett. **15**, 446 (1972).

Larkin, A., Effect of Inhomogeneities on the Structure of the Mixed State of Superconductors, Sov. Phys. JETP **31**, 784 (1970).

Lee, H., Azaria, P. and Boulat, E., Effect of Hund coupling in the one-dimensional SU(4) Hubbard model, Phys. Rev. B **69**, 155109 (2004).

Lee, P. and Rice, T., Electric field depinning of charge density waves, Phys. Rev. B **19**, 3970 (1979).

Lee, P., Rice, T. and Anderson, P., Conductivity from charge or spin density waves, Solid State Commun. **14**, 703 (1974).

Lee, S., Marston, J. and Fjærestad, J., Phase diagram of the three-band half-filled Cu-O two-leg ladder, Phys. Rev. B **72**, 075126 (2005).

Li, Y. and Teitel, S., Finite-size scaling study of the three-dimensional classical XY model, Phys. Rev. B **40**, 9122 (1989).

Lin, H., Balents, L. and Fisher, M., Exact SO(8) symmetry in the weakly-interacting two-leg ladder, Phys. Rev. B **58**, 1794 (1998).

Luttinger, J., An Exactly Soluble Model of a Many-Fermion System, J. Math. Phys. **4**, 1154 (1963).

McMillan, W., Landau theory of charge-density waves in transition-metal dichalcogenides, Phys. Rev. B **12**, 1187 (1975).

McMillan, W., Microscopic model of charge-desity waves 2H-$TaSe_2$, Phys. Rev. B **16**, 643 (1977).

Mermin, N. and Wagner, H., Absence of Ferromagnetism or Antiferromagnetism in One- or Two-Dimensional Isotropic Heisenberg Models, Phys. Rev. Lett. **17**, 1133 (1966).

Momoi, T. and Hikihara, T., Exact Duality Relations in Correlated Electron Systems, Phys. Rev. Lett. **91**, 256405 (2003).

Moncton, D., Axe, J. and DiSalvo, F., Neutron scattering study of the charge-density wave transitions in 2H-$TaSe_2$ and 2H-$NbSe_2$, Phys. Rev. B **16**, 801 (1977).

Murray, C. A., Gammel, P. L., Bishop, D. J., Mitzi, D. and Kapitulnik, A., Observation of a Hexatic Vortex Glass in Flux Lattices of High-T_c Superconductor $Bi_{2.1}Sr_{1.9}Ca_{0.9}Cu_2O_{8+\delta}$, Phys. Rev. Lett. **64**, 2312 (1990).

Nakamura, M., Tricritical behavior in the extended Hubbard chains, Phys. Rev. B **61**, 16377 (2000).

Nakamura, M., Identification of topologically different valence bond states in spin ladders, Phys. B: Condens. Matter **329-333**, 1000 (2003).

Nakanishi, K. and Shiba, H., Theory of Three-Dimensional Orderings of Charge-Density Waves in 1T-TaX_2 (X: S, Se), J. Phys. Soc. Japan **53**, 1103 (1984).

Nattermann, T., Scaling Approach to Pinning: Charge-Density Waves and Giant Flux Creep in Superconductors, Phys. Rev. Lett. **64**, 2454 (1990).

Nishiyama, Y., Hatano, N. and Suzuki, M., Phase Transition and Hidden Orders of the Heisenberg Ladder Model in the Ground State, J. Phys. Soc. Japan **64**, 1967 (1995).

Nonne, H., Boulat, E., Capponi, S. and Lecheminant, P., Competing orders in the generalized Hund chain model at half filling, Phys. Rev. B **82**, 155134 (2010).

Ogata, M. and Shiba, H., Bethe-ansatz wave function, momentum distribution, and spin correlation in the one-dimensional strongly correlated Hubbard model, Phys. Rev. B **41**, 2326 (1990).

Okamoto, J., Arguello, C., Rosental, E., Pasupathy, A. N. and Millis, A. J., Experimental evidence for a Bragg glass density wave phase in a transition-metal dichalcogenide, arXiv:1405.5561 (2014).

Okamoto, J. and Millis, A., One-dimensional physics in transition metal nanowires: Phases and elementary excitations, Phys. Rev. B **84**, 205433 (2011).

Okamoto, J. and Millis, A., One-dimensional physics in transition-metal nanowires: Renormalization group and bosonization analysis, Phys. Rev. B **85**, 115406 (2012).

Overhauser, A., Giant Spin Density Waves, Phys. Rev. Lett. **4**, 462 (1960).

Peierls, R., Zur Theorie der elektrischen und thermischen leitfahigkeit von metallen, Ann. Phys. **4**, 129 (1930).

Peierls, R. E., *Quantum Theory of Solids*, International Series of Monographs on Physics, Clarendon Press (1996).

Penn, D., Stability Theory of the Magnetic Phases for a Simple Model of the Transition Metals, Phys. Rev. **142**, 350 (1966).

Peskin, M. E. and Schroeder, D. V., *An Introduction to Quantum Field Theory*, Advanced book classics, Addison-Wesley Publishing Company (1995).

Rosso, A. and Giamarchi, T., X-ray spectrum of a pinned charge density wave, Phys. Rev. B **70**, 224204 (2004).

Roth, L., Simple Narrow-Band Model of Ferromagnetism Due to Intra-Atomic Exchange, Phys. Rev. **149**, 306 (1966).

Rouxel, J. and Schlenker, C., Structural, Electronic Properties and Design of Quasi-One-Dimensional Inorganic Conductors, in Charge Density Waves Solids, edited by Gor'kov, L. P. and Grüner, G., vol. 25 of *Modern Problems in Condensed Matter Sciences*, pp. 15–83, Elsevier (1989).

Sakamoto, H., Momoi, T. and Kubo, K., Ferromagnetism in the one-dimensional Hubbard model with orbital degeneracy: From low to high electron density, Phys. Rev. B **65**, 224403 (2002).

Schlenker, C., Peierls Transition in the Quasi-One Dimensional Blue Bronzes $K_{0.30}MoO_3$ and $RbO_{0.30}MoO_3$, J. Phys. Colloq. **44**, 1757 (1983).

Schulz, H., Phases of two coupled Luttinger liquids, Phys. Rev. B **53**, 2959 (1996).

Schulz, H., Cuniberti, G. and Pieri, P., Fermi liquids and Luttinger liquids, in Field Theories for Low-Dimensional Condensed Matter Systems, edited by Morandi, G., Sodano, P., Tagliacozzo, A., and Tognetti, V., vol. 131 of *Springer Series in Solid-State Sciences*, pp. 9–81, Springer Berlin Heidelberg (2000).

Sham, L. and Patton, B., Effect of impurity on a Peierls transition, Phys. Rev. B **13**, 3151 (1976).

Shankar, R., Ashkin-Teller and Gross-Neveu Models: New Relations and Reuslts, Phys. Rev. Lett. **55**, 453 (1985).

Shankar, R., Renormalization-group approach to interacting fermions, Rev. Mod. Phys. **66**, 129 (1994).

Shelton, D., Nersesyan, A. and Tsvelik, A., Antiferromagnetic spin ladders: Crossover between spin S=1/2 and S=1 chains., Phys. Rev. B **53**, 8521 (1996).

Shelton, D. and Tsvelik, A., Superconductivity in a spin liquid: A one-dimensional example, Phys. Rev. B **53**, 14036 (1996).

Shirakawa, T., Nishimoto, S. and Ohta, Y., Superconductivity in a model of two Hubbard chains coupled with ferromagnetic exchange interaction, Phys. Rev. B **77**, 224510 (2008).

Snijders, P. C. and Weitering, H. H., Colloquium: Electronic instabilities in self-assembled atom wires, Rev. Mod. Phys. **82**, 307 (2010).

Stoner, E., Collective Electron Ferromagnetism, Proc. R. Soc. London. Ser. A, **165**, 372 (1938).

Strong, S. and Millis, A., Competition between singlet formation and magnetic ordering in one-dimensional spin systems, Phys. Rev. B **50**, 9911 (1994).

Tomonaga, S., Remarks on Bloch's Method of Sound Waves applied to Many-Fermion Problems, Prog. Theor. Phys. **5**, 544 (1950).

Tosatti, E., Displacive Reconstruction Phase Transitions of Clean Transition Metal and Semiconductor Surfaces, in Modern Trends in the Theory of Condensed Matter, edited by Pękalski, A., and Przystawa, J., vol. 115 of *Lecture Notes in Physics*, pp. 501–530, Springer Berlin Heidelberg (1980).

Tsuchiizu, M. and Furusaki, A., Generalized two-leg Hubbard ladder at half filling: Phase diagram and quantum criticalities, Phys. Rev. B **66**, 245106 (2002).

Tsuchiizu, M. and Furusaki, A., Phase Diagram of the One-Dimensional Extended Hubbard Model at Half Filling, Phys. Rev. Lett. **88**, 056402 (2002).

Tsvelik, A. M., Field theory for a fermionic ladder with generic intrachain interactions, Phys. Rev. B **83**, 104405 (2011).

Varma, C. and Simons, A., Strong-Coupling Theory of Charge-Density-Wave Transitions, Phys. Rev. Lett. **51**, 138 (1983).

Varma, C. and Zawadowski, A., Scaling in an interacting two-component (valence-fluctuation) electron gas, Phys. Rev. B **32**, 7399 (1985).

Voit, J., One-dimensional Fermi liquids, Reports Prog. Phys. **58**, 977 (1995).

Walker, M. and Jacobs, A., Effects of interlayer interactions on charge-density waves in the 2H-$TaSe_2$ structure, Phys. Rev. B **25**, 4856 (1982).

Wang, H., Lee, J., Dreyer, M. and Barker, B. I., A scanning tunneling microscopy study of a new superstructure around defects created by tip-sample interaction on 2H- $NbSe_2$., J. Phys. Condens. Matter **21**, 265005 (2009).

Wang, S.-C., Yilmaz, M., Knox, K., Zaki, N., Dadap, J., Valla, T., Johnson, P. and Osgood, R., Electronic structure of a Co-decorated vicinal Cu(775) surface: High-resolution photoemission spectroscopy, Phys. Rev. B **77**, 115448 (2008).

Weber, F., Rosenkranz, S., Castellan, J.-P., Osborn, R., Hott, R., Heid, R., Bohnen, K.-P., Egami, T., Said, A. and Reznik, D., Extended Phonon Collapse and the Origin of the Charge-Density Wave in 2H-$NbSe_2$, Phys. Rev. Lett. **107**, 107403 (2011).

Wiesendanger, R., *Scanning Probe Microscopy and Spectroscopy: Methods and Applications*, Cambridge University Press (1994).

Wilson, J., DiSalvo, F. and Mahajan, S., Charge-density waves and superlattices in the metallic layered transition metal dichalcogenides, Adv. Phys. **24**, 1171 (1975).

Wilson, K., The renormalization group: Critical phenomena and the Kondo problem, Rev. Mod. Phys. **47**, 773 (1975).

Wu, C., Liu, W. and Fradkin, E., Competing orders in coupled Luttinger liquids, Phys. Rev. B **68**, 115104 (2003).

Yeom, H. W., Ahn, J. R., Yoon, H., Lyo, I., Jeong, H. and Jeong, S., Real-space investigation of the metal-insulator transition of Si(557)-Au, Phys. Rev. B **72**, 035323 (2005).

Zaki, N., Marianetti, C., Acharya, D., Zahl, P., Sutter, P., Okamoto, J., Johnson, P., Millis, A. and Osgood, R., Experimental observation of spin-exchange-induced dimerization of an atomic one-dimensional system, Phys. Rev. B **87**, 161406 (2013).

Zaki, N., Potapenko, D., Johnson, P. and Osgood, R., Atom-wide Co wires on Cu(775) at room temperature, Phys. Rev. B **80**, 155419 (2009).

Appendix A

Fermionic renormalization group

When two Fermi velocities are different, it is more convenient to use current operators than using refermionization. We follow the notation of Balents and Fisher (1996) with slight modification:

$$J_{mr} = \sum_{ss'} \psi^\dagger_{msr}\psi_{ms'r}, \quad \boldsymbol{J}_{mr} = \sum_{ss'} \psi^\dagger_{msr}\boldsymbol{\sigma}_{ss'}\psi_{ms'r} \tag{A.1}$$

$$L_r = \sum_{ss'} \psi^\dagger_{Asr}\psi_{Bs'r}, \quad \boldsymbol{L}_r = \sum_{ss'} \psi^\dagger_{Asr}\boldsymbol{\sigma}_{ss'}\psi_{Bs'r} \tag{A.2}$$

$$M_{mr} = -i\psi_{m\uparrow r}\psi_{m\downarrow r}, \quad N_{rss'} = \psi_{rAs}\psi_{rBs'}. \tag{A.3}$$

When $k_A \neq k_B$, the interactions terms are given by,

$$\begin{aligned} -\mathcal{H}_{\text{int}} = {} & \widetilde{g}_{1\rho} J_{AR}J_{AL} + \widetilde{g}_{1\sigma}\boldsymbol{J}_{AR}\cdot\boldsymbol{J}_{AL} \\ & + \widetilde{g}_{2\rho} J_{BR}J_{BL} + \widetilde{g}_{2\sigma}\boldsymbol{J}_{BR}\cdot\boldsymbol{J}_{BL} \\ & + \widetilde{g}_{x\rho}\left(J_{AR}J_{BL} + J_{BR}J_{AL}\right) \\ & + \widetilde{g}_{x\sigma}\left(\boldsymbol{J}_{AR}\cdot\boldsymbol{J}_{BL} + \boldsymbol{J}_{BR}\cdot\boldsymbol{J}_{AL}\right) \\ & + \widetilde{g}_{t\rho}(L_RL_L + \text{h.c.}) + \widetilde{g}_{t\sigma}(\boldsymbol{L}_R\cdot\boldsymbol{L}_L + \text{h.c.}). \end{aligned} \tag{A.4}$$

This expression is formally the same as the one given in Balents and Fisher (1996). When $k_A = k_B$, we have additional processes,

$$-\mathcal{H}'_{\rm int} = \widetilde{g}_{a\rho}\left(L_R L_L^\dagger + \text{h.c.}\right) + \widetilde{g}_{a\sigma}\left(\boldsymbol{L}_R \cdot \boldsymbol{L}_L^\dagger + \text{h.c.}\right). \tag{A.5}$$

Umklapp processes are allowed when the filling is commensurate ($n = 2$):

$$\begin{aligned}
-\mathcal{H}''_{\rm int} = {} & \widetilde{g}_{1u}\left(M_{AR}M_{AL}^\dagger + \text{h.c.}\right) \\
& + \widetilde{g}_{2u}\left(M_{BR}M_{BL}^\dagger + \text{h.c.}\right) \\
& + \widetilde{g}_{xu}\left(M_{AR}M_{BL}^\dagger + M_{BR}M_{AL}^\dagger + \text{h.c.}\right) \\
& + \widetilde{g}_{tu\rho}\left(N_{R\alpha\beta}^\dagger N_{L\alpha\beta} - N_{R\alpha\beta}^\dagger N_{L\beta\alpha} + \text{h.c.}\right) \\
& + \widetilde{g}_{tu\sigma}\left(N_{R\alpha\beta}^\dagger N_{L\alpha\beta} + N_{R\alpha\beta}^\dagger N_{L\beta\alpha} + \text{h.c.}\right).
\end{aligned} \tag{A.6}$$

The $\widetilde{g}_{1u}$ and $\widetilde{g}_{2u}$ processes are allowed only when each band has commensurate filling, i.e., $k_m = \pi/2$. We ignore all the chiral scattering processes, since they only renormalize the velocities. The initial values of coupling constants are: $\widetilde{g}_{1\rho} = \widetilde{g}_{2\rho} = -\widetilde{g}_{1\sigma} = -\widetilde{g}_{2\sigma} = \widetilde{g}_{1u} = \widetilde{g}_{2u} = -U/2$, $\widetilde{g}_{x\sigma} = -\widetilde{g}_{t\rho} = \widetilde{g}_{t\sigma} = -\widetilde{g}_{xu} = J/2$, $\widetilde{g}_{x\rho} = (-2U + 5J)/2$, $\widetilde{g}_{a\rho} = (U - 4J)/2$, $\widetilde{g}_{a\sigma} = (U - 2J)/2$, $\widetilde{g}_{tu\rho} = (-U + J)/2$, and $\widetilde{g}_{tu\sigma} = (-U + 3J)/2$.

In the following, we use the renormalized coupling constants, $y_i = \widetilde{g}_i \pi^{-1}(v_A + v_B)^{-1}$. The RG equations for the $k_A = k_B = \pi/2$ case are

$$\begin{aligned}
\dot{y}_{1\rho} &= -\beta\left(y_{a\rho}^2 + 3y_{a\sigma}^2 + 3y_{tu\sigma}^2 + y_{tu\rho}^2 - y_{t\rho}^2 - 3y_{t\sigma}^2\right) - \alpha y_{1u}^2 \\
\dot{y}_{2\rho} &= -\alpha\left(y_{a\rho}^2 + 3y_{a\sigma}^2 + 3y_{tu\sigma}^2 + y_{tu\rho}^2 - y_{t\rho}^2 - 3y_{t\sigma}^2\right) - \beta y_{2u}^2 \\
\dot{y}_{x\rho} &= y_{a\rho}^2 + 3y_{a\sigma}^2 - 3y_{tu\sigma}^2 - y_{tu\rho}^2 - y_{t\rho}^2 - 3y_{t\sigma}^2 - y_{xu}^2
\end{aligned} \tag{A.7}$$

$$\begin{aligned}
\dot{y}_{1\sigma} &= -2\beta\left(y_{a\sigma}\left(y_{a\sigma}+y_{a\rho}\right)+y_{tu\sigma}\left(y_{tu\sigma}+y_{tu\rho}\right)+y_{t\sigma}\left(y_{t\sigma}-y_{t\rho}\right)\right)-4\alpha y_{1\sigma}^{2}\\
\dot{y}_{2\sigma} &= -2\alpha\left(y_{a\sigma}\left(y_{a\sigma}+y_{a\rho}\right)+y_{tu\sigma}\left(y_{tu\sigma}+y_{tu\rho}\right)+y_{t\sigma}\left(y_{t\sigma}-y_{t\rho}\right)\right)-4\beta y_{2\sigma}^{2}\\
\dot{y}_{x\sigma} &= -2\left(y_{a\sigma}\left(y_{a\sigma}-y_{a\rho}\right)+y_{tu\sigma}\left(y_{tu\sigma}-y_{tu\rho}\right)+y_{t\sigma}\left(y_{t\sigma}+y_{t\rho}\right)\right)-4y_{x\sigma}^{2}
\end{aligned} \tag{A.8}$$

$$\begin{aligned}
\dot{y}_{t\rho} &= -2y_{tu\rho}y_{xu}+y_{t\rho}y_{c-}+3y_{t\sigma}y_{s-}\\
\dot{y}_{t\sigma} &= 2y_{tu\sigma}y_{xu}+y_{t\rho}y_{s-}+y_{t\sigma}\left(y_{c-}-2y_{s+}\right)
\end{aligned} \tag{A.9}$$

$$\begin{aligned}
\dot{y}_{a\rho} &= -y_{tu\rho}\left(\alpha y_{1u}+\beta y_{2u}\right)-y_{a\rho}y_{c-}-3y_{a\sigma}y_{s-}\\
\dot{y}_{a\sigma} &= -y_{tu\sigma}\left(\alpha y_{1u}+\beta y_{2u}\right)-y_{a\rho}y_{s-}-y_{a\sigma}\left(y_{c-}+2y_{s+}\right)
\end{aligned} \tag{A.10}$$

$$\begin{aligned}
\dot{y}_{1u} &= -4\left(3\beta y_{a\sigma}y_{tu\sigma}+\beta y_{a\rho}y_{tu\rho}+\alpha y_{1u}y_{1\rho}\right)\\
\dot{y}_{2u} &= -4\left(3\alpha y_{a\sigma}y_{tu\sigma}+\alpha y_{a\rho}y_{tu\rho}+\beta y_{2u}y_{2\rho}\right)\\
\dot{y}_{xu} &= 4\left(3y_{t\sigma}y_{tu\sigma}-y_{t\rho}y_{tu\rho}-y_{xu}y_{x\rho}\right)
\end{aligned} \tag{A.11}$$

$$\begin{aligned}
\dot{y}_{tu\rho} &= -y_{a\rho}\left(\alpha y_{1u}+\beta y_{2u}\right)-2y_{t\rho}y_{xu}-y_{tu\rho}y_{c+}-3y_{tu\sigma}y_{s-}\\
\dot{y}_{tu\sigma} &= -y_{a\sigma}\left(\alpha y_{1u}+\beta y_{2u}\right)+2y_{t\sigma}y_{xu}-y_{tu\rho}y_{s-}-y_{tu\sigma}\left(y_{c+}+2y_{s+}\right),
\end{aligned} \tag{A.12}$$

where we defined $y_{c(s)\pm}=\alpha y_{1\rho(\sigma)}+\beta y_{2\rho(\sigma)}\pm 2y_{x\rho(\sigma)}$ with $\alpha=(v_A+v_B)/(2v_A)$, and $\beta=(v_A+v_B)/(2v_B)$. For doped cases, and $k_A\neq k_B$ cases, the coupling constants which are not allowed by momentum conservation should be removed.

As we mentioned, the asymptotic behavior of a RG flow is captured by the ansatz (2.55), and now the ratios of coupling constants at fixed points depend on velocity differences. However, we can easily distinguish phases with different fixed point structure by looking at the signs of relevant couplings, and irrelevant couplings. In that sense, we identify phases as the same ones when the relevant couplings and the signs are the same. When the relevant couplings are different, or the signs of renormalized couplings are different, we regard them as different phases.

Appendix B

Data analysis of the STM image

In this appendix, we explain the detail procedures to analyze the STM image of $NbSe_2$. First, the procedures to extract order parameters from the topographic data are as follows. The first step is a Fourier transformation of the data (an image of 1024×1024 pixels) assuming that the field of view is periodically repeated in the x and y directions. The Fourier transformed image has a central peak, atomic Bragg peaks at reciprocal lattice vectors $\vec{G}_i$, and 6 relatively sharp peaks originating from the CDW correlations located approximately on the vertices of a hexagon, $\vec{Q}_{i=1...6}$ [Fig. B.1(a)]. We define the mean distance of the CDW peaks from the origin to be $Q \approx |\vec{G}|/3$. We then filter the data by retaining only the region in an annulus of inner radius $Q/2$ and outer radius $3Q/2$ [Fig. B.1(b)]. Next, we performed an affine transformation

$$\vec{x}' = A\vec{x} + \vec{b} \tag{B.1}$$

to remove the shear distortion, which we believe arises from the drift of the scanning tunneling microprobe. To define the affine transformation we partition the annulus into six segments, with each boundary between segments passing through a middle point of neighboring CDW peaks and through the origin. In Fig. B.1(b), X's are the middle points, and dashed lines are the boundaries of a segment. For each segment, we define an affine transformation which maps each middle point position to a vertex

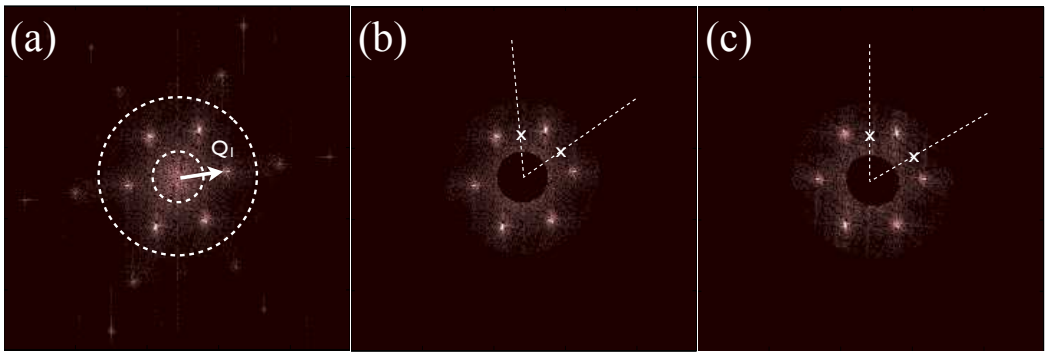

Figure B.1: (a) The absolute values of Fourier components $\delta\rho(\vec{k})$. The Fourier components outside the annulus given by the dashed lines are removed. (b) Fourier components after removing atomic peaks and $\vec{k} = 0$ components. X's are the middle points of neighboring CDW peaks. (c) The Fourier components after affine transformations.

of a regular hexagon. The positions of two middle points and the origin of the picture uniquely defines the parameters, A and $\vec{b}$, in Eq. (B.1) for each segment. After the affine transformations, the Fourier components will look like Fig. B.1(c). Finally, we need to perform the inverse Fourier transform of the filtered, affine-transformed data to obtain a position dependent amplitude which we identify with the CDW component $\delta\rho(\vec{x})$ in the real space. $\delta\rho(\vec{x})$ is related to the order parameters, $\psi_i(\vec{x}) = \eta_i(\vec{x})e^{i\phi_i(\vec{x})}$ by

$$\delta\rho(\vec{x}) = \sum_{i=1}^{3} \Re\psi_i(\vec{x})e^{i\vec{Q}_i\cdot\vec{x}}. \tag{B.2}$$

To obtain the η_i and ϕ_i, we shift each CDW peak in a circle of radius $Q/2$ to the origin of the Fourier space, and Fourier transform it to the real space.

The construction of the Delaunay diagram is as follows. First, we remove the central peaks of the Fourier image as Fig. B.1, and then transform it back to the

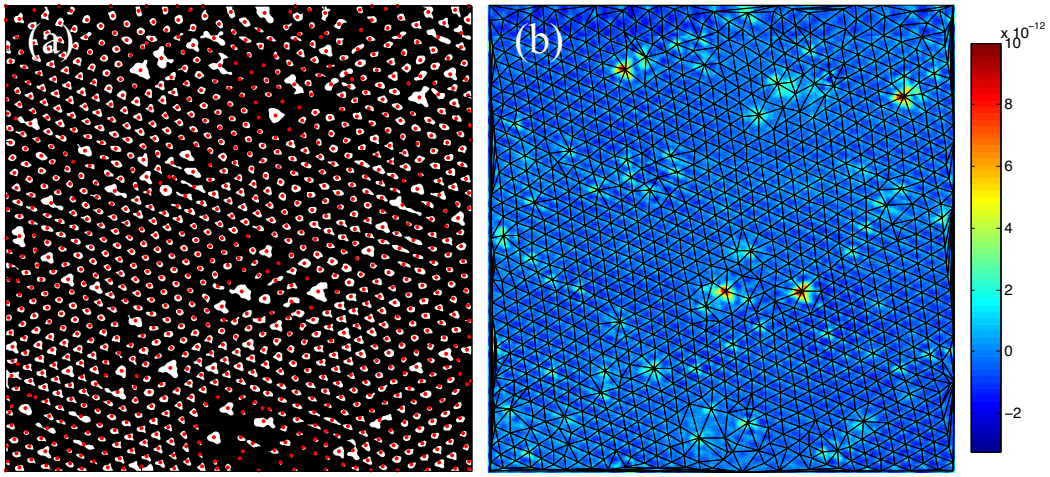

Figure B.2: (a) The binary image after filtering the topographic image by a threshold value. (b) The obtained Delaunay image overlaid on the topographic image.

real space. Then, we create a binary image by distinguishing each data points by a threshold value; in Fig. B.2, the white parts are above the value, and the black parts are below. The threshold value is chosen such that we obtain a maximal number of distinct points. If the value is too low neighboring maximal islands are connected, while if the value is too large, we miss some of the CDW maxima. The locations of maxima are identified by red points in Fig. B.2. The Delaunay diagram is then constructed based on these points.